UNIVERSITY OF SOUTHAMPTON

Signal Processing of Electrocardiogram for Arrhythmia Prediction and Classification

by

Hanjie Chen

A thesis submitted for the
degree of Doctor of Philosophy

in the

Faculty of Engineering and Physical Science
School of Electronics and Computer Science

February 2022

University of Southampton

Abstract

Faculty of Engineering and Physical Science
School of Electronics and Computer Science

Doctor of Philosophy

by Hanjie Chen

The prevalence of Cardiovascular Diseases (CVD) currently poses a significant global burden to the healthcare systems. Arrhythmia is a condition associated with CVD that can lead to death in chronic CVD patients or even to an apparent healthy person. Electrocardiogram (ECG) is the first-point diagnosis tool of arrhythmia. Currently, Implantable Cardioverter Defibrillator (ICD) and its subcutaneous version (S-ICD) are used for treating fatal arrhythmias. However, these devices can only detect arrhythmia once it started and therefore in the case of fatal arrhythmias such as Ventricular Fibrillation they are not very effective in saving lives. Recently, ECG has been applied to predict impending arrhythmias. However, their prediction and classification performance need to be improved to become acceptable in day-to-day clinical use. Also, such predictive methods need to be incorporated within the framework of ICD itself. This dissertation addresses this issue and provide a solution by improving the predictive capability of ECG and then integrating it with S-ICD.

We first proposed two automated algorithms for precise delineation of ECG fiducial points based on the time- domain Hierarchical clustering and the time-frequency-domain Discrete Wavelet Transform (DWT). Then we developed a new algorithm based on the Phase Space Reconstruction (PSR) to overcome the T-wave over-sensing problem that typically plagues efficacy of ICDs, more specifically the S- ICD system. After that, we reported a risk index based on PSR and fuzzy c-means clustering to predict an impending fatal Ventricular Arrhythmias (VA) and its classifications (four different types of VA). The main feature of the proposed method is that for the first time it has been shown that it is not only possible to predict an impending arrhythmia sufficiently before its actual occurrence in time but also is possible to classify the type of arrhythmia before it actually occurs (1 min after the prediction time point).

We further extended these methods for classifying other types of non-fatal arrhythmias such as, Atrial Fibrillation (AF) which are indicative to the risk of stroke in a patient suffering from chronic CVD condition. The methods proposed here could be used in day-to-day clinical practice after rigorous clinical trial to advance technologies such as ICD and S-ICD that can help to pre-empt the occurrence of fatal ventricular arrhythmia - a main cause of Sudden Cardiac Death (SCD).

Contents

List of Figures

List of Tables

Nomenclature

ACC	Accuracy
AF	Atrial Fibrillation
AFL	Atrial Flutter
ANN	Artificial Neural Network
AV	Atrioventricular
BII	Second Degree Block
CVD	Cardiovascular Disease
CWT	Continuous Wavelet Transform
DCT	Discrete Cosine Transform
DWT	Discrete Wavelet Transform
ECG	Electrocardiogram
ELM	Extreme Learning Machine
EMG	Electromyography
FDA	United States Food and Drug Administration
FIR	Finite Impulse Response
FN	False Negative
FP	False Positive
FT	Fourier Transform
ICA	Independent Component Analysis
ICD	Implantable Cardioverter Defibrillator
IQR	Interquartile Range
KNN	K-Nearest Neighbor
$LBBB$	Left Bundle Branch Block
LMS	Least Mean Square
LVQ	Learning Vector Quantization
MSE	Mean Square Error
PAC	Premature Atrial Contractions
PSR	Phase Space Reconstruction
$PSVT$	Paroxysmal Supraventricular Tachycardia
PVC	Premature Ventricular Contractions
QoL	Quality of Life
$RBBB$	Right Bundle Branch Block

$RBFN$	Radial Basis Function Neural Network
SA	Sinoatrial
SE	Sensitivity
$SICD$	Subcutaneous Implantable Cardioverter Defibrillator
SND	Sinus Node Dysfunction
SWT	Stationary Wavelet Transform
SCD	Sudden Cardiac Death
$STFT$	Short Time Fourier Transform
SVM	Support Vector Machine
$TDMG$	Time Domain Morphology and Gradient
TN	True Negative
TP	True Positive
$TVICD$	Transvenous ICD
VA	Ventricular Arrhythmia
VF	Ventricular Fibrillation
VPB	Ventricular Premature Beat
VT	Ventricular Tachycardia
WT	Wavelet Transform
$+P$	Positive Predictivity

Declaration of Authorship

I declare that this thesis and the work presented in it is my own and has been generated by me as the result of my own original research.

I confirm that:

This work was done wholly or mainly while in candidature for a research degree at this University;

Where any part of this thesis has previously been submitted for a degree or any other qualification at this University or any other institution, this has been clearly stated;

Where I have consulted the published work of others, this is always clearly attributed;

Where I have quoted from the work of others, the source is always given. With the exception of such quotations,

I have acknowledged all main sources of help;

Where the thesis is based on work done by myself jointly with others, I have made clear exactly what was done by others and what I have contributed myself;

Parts of this work have been published as:

Chapter 3: Wiles et al. (2018); Chen and Maharatna (2019); Chen and Maharatna (2020); Wiles et al. (2022);

Chapter 4: Chen et al. (2021c);

Chapter 5: Chen et al. (2021b);

Chapter 6: Chen et al. (2021a);

Signed:..... Date:.....

Acknowledgements

First and foremost, I am extremely grateful to my supervisor Professor Koushik Maharatna for his inspiration and guidance, but also for giving me the autonomy and freedom I needed to develop this project in my own way. He is my supervisor but also like an elder to support me for my research and life

Also, I would like to thank Doctor Benedict M. Wiles and Professor John M. Morgan for providing ECG database from University Hospital Southampton to me. It is also my pleasure to acknowledge Dr Saptarshi Das and my research group.

Finally, I would like to express my whole-hearted thanks to my parents, Mr. Zhiming Chen and Mrs. Yuanqi Zhang. Thank you for their support mo matter how hard the challenge is. I dedicate this work to them and Rong Ma.

Chapter 1

Introduction

Over the past decades, many intelligent and advanced signal processing algorithms have been developed in the fields of bio-medical technologies such as, automated diagnosis, surgical robot and mobile health monitoring. An important area of is automated early diagnosis of an acute event in Cardiovascular Diseases (CVD) since such an event either leads to disability or death or at a minimum, hospitalisation. It requires a possible prediction and classification of different types of CVD. Arrhythmia as one of the most common condition in chronic CVD patients Rabe et al. (2018), is paid much attention, especially the Ventricular Arrhythmias (VA) - which may lead to the Sudden Cardiac Death (SCD). ECG plays an important role in the assessment of different types of arrhythmia in the established clinical practice. Recent advances in wearable ECG technology coupled with improved diagnostic algorithms have been applied to protect patients from arrhythmia under the framework of mobile healthcare making it possible to offer treatment anytime anywhere Abubakar et al. (2018).

On the other hand, in patients with previous acute CVD episodes, arrhythmia management is done using pacemaker and Implantable Cardioverter Defibrillator (ICD). The former is used to prevent patient's heart from beating too slowly and ICD is applied to detect and stop fatal arrhythmia by applying an electrical shock. However, such advanced technology can detect VA and stop it only after it occurs. If a predictive algorithm could be incorporated in them, they may pre-empt its occurrences and thereby improving the patient's Quality of Life (QoL). Besides, accuracy of performance is another major concern in ICD applications. For example, in S-ICD, a patient can receive inappropriate shock when the device wrongly identifies an R or T-wave even when there is no VA – known as T-wave over sensing problem (TWOS). It has been reported that up to 8% of patients receive this inappropriate shock per year Boersma et al. (2017). Therefore, reduction of TWOS is a prime concern for S-ICD performance.

The rest of the chapter is organised as follows. Section 1.1 shows the motivation of our work, followed by Section 1.2 briefly introducing the main aim of our entire research

work. Section 1.3 highlights the contributions and the list of publications generated from our research. Finally, Section 1.4 presents the outline of the thesis.

1.1 Motivation

According to a report from the World Health Organization (WHO), 31% of all global deaths are due to the CVDs W.H.O. (2019). In general, CVDs are conditions affecting the functions of heart and blood vessels, which can be broadly divided into the following categories of diseases: cardiac, cerebrovascular and peripheral artery. An arrhythmia is an irregular heartbeat, also can be defined as an abnormal heart rhythm that occurs in the patients with CVDs which can lead to acute conditions resulting in fatal consequence. Also, a certain type of arrhythmia can be precursors of acute cerebrovascular episodes such as, stroke. A report from the National Health Service (NHS) shows that more than 2 million people in the UK experience arrhythmias every year NHS (2018) and incurs huge costs due to hospitalisation. Giedrimiene and King (2017) reported that prescriptions and operations costs of CVD in UK is around £6.8 billion. Besides, CVD cost the US economy $320 billion every year. By 2030, this cost is predicted to rise to $818 billion in the US.

Normally, arrhythmia can be divided into two different types based on its origin. The first type of arrhythmia is defined as supraventricular arrhythmia because the origin is the upper chamber of heart, i.e. Atria. Another type of arrhythmia originates from the lower chamber of heart, i.e. Ventricle, and is called VA. For most people, arrhythmias do not influence their normal life if they can be properly diagnosed. However, VAs could be life-threatening and can cause collapse or SCD Harris and Lysitsas (2015). Also, the frequency of Atrial Fibrillation (AF) has been evidently associated with acute cerebrovascular events Doshi et al. (2021). Therefore, if such arrhythmic episodes could be *predicted* and *classified*, then one can pre-empt the impending acute events and the associated hospitalisation thereby saving lives and reducing healthcare cost – hospitalisation alone accounts for approximately 60% of the CVD expenditure in the UK Luengo-Fernandez et al. (2006).

Currently, there is no available algorithm that can simultaneously predict and classify arrhythmias although several algorithms have been proposed for predicting or classifying arrhythmias. An important requirement for an arrhythmia prediction algorithm is that it needs real-time monitoring of patients – and hence, should be applicable in mobile environment – so that in case of an impending fatal event the appropriate clinical service can be provided at the point-of-need. This fact motivated us to undertake this research.

.

1.2 Aim and Objective

The main aim of this thesis is to develop an algorithm for predicting impending arrhythmia and classifying their type in order to provide clinical services at the point-of-need. Given that the populations affected by chronic CVD might or might not have ICD, the algorithm should be amenable for both populations. However, ECG is the fundamental process for detecting arrhythmia in both populations – be it externally worn or embedded within an ICD. Therefore, we aim to develop our algorithm based on ECG signal. This aim will be achieved through the following objectives.

- Development of automated algorithms for precise identification of ECG fiducial points: The first important thing in classifying the normal and abnormal heartbeats is calculating the R-R interval in an ECG waveform. Therefore, it is necessary to design an algorithm to detect R-waves or QRS-complexes. In addition, given their diagnostic importance, the precise occurrences of T- and P-waves need to be identified in terms of their temporal position.
- Reduction of T-wave over-sensing (TWOS): As the TWOS is the major cause of inappropriate shocks in ICD system, an algorithm needs to be developed that can reduce the TWOS.
- Development of an algorithm to predict VA: This objective targets at developing an algorithm for not only prediction of VA but also to classify its type so that appropriate clinical actions could be taken.
- Development of an algorithm for classifying other types of arrhythmia: Under this objective, we develop a generic arrhythmia classifier given the importance of even the non-fatal arrhythmias as the precursor of other types of CVD complicacies.

1.3 Contribution

Following the objectives described in the foregoing section, here we summarise the list of our contribution:

- We developed an automated ECG delineation algorithm with high precision. This new algorithm combines hierarchical clustering and wavelet transform to detect QRS complexes and T waves in ECG. The experimental results in terms of positive detection (+P) and sensitivity (SE) that tested on MIT-BIH database and QT database is used to evaluate the proposed algorithm. The results also compared with other formally published methods and show a high performance for ECG

feature extraction. Our algorithm achieved 99.89% of Se and 99.94% of $+P$, 100% of Se and 99.83% of $+P$ for R peak detection in MIT-BIH and QT database respectively. It also shows 99.91% of Se and 99.38% of $+P$ for T peak detection in QT database.

- We have developed a PSR-based algorithm to reduce TWOS in S-ICD system. The algorithm has been evaluated against 34 records from University Hospital Southampton (UHS) and all records from the MIT-BIH arrhythmia database. In the UHS analysis we demonstrate a sensitivity of 99.88% and a positive predictive value of 99.99% with reductions in TWOS episodes (from 166 to 0). Whilst in the MIT-BIH analysis we demonstrate a sensitivity of 99.87% and a positive predictive value of 99.99%, with effective reduction in the number of false positives in R wave detection. The average processing time for 1 min ECG signals from all records is 2.9 s.

- We propose a novel algorithm based on the combination of PSR and Fuzzy C-means (FCM) clustering technique of the ECG for prediction and classification of VA. 32 healthy subjects and 32 arrhythmic subjects from PTBDB and CUDB respectively were used to evaluate our proposed technique. The proposed system showed 298.3 seconds of an average prediction time for impending ventricular arrhythmia based on 32 VA subjects. Also, our system can classify four types of VA (VA without VPBs, VF, VT, and VT followed by VF) with an average 238.3 seconds before the VA onset. It achieved an average accuracy of 98.4%, a sensitivity of 97.5% and s specificity of 99.1%, which was comparable and better then the previous work. This study has demonstrated that this algorithm can be used to predict and classify the impending VA.

- Finally, a simple PSR-based arrhythmia classifier has been developed to classify normal ECG, atrial fibrillation (AF), VT, VF and VT followed by VF. This process was verified with 122 records with more than 5500 windows of ECG signals. The results show an average sensitivity of 98.73%, specificity of 99.71% and accuracy of 99.56%. Keeping in mind its possible implementation in a mobile environment, which is resource-constrained in terms of processing and battery power, we also explored the computational complexity of this algorithm. The average computational time it takes for processing of one 5 s 1.9 s and therefore satisfying the real-time constraint for arrhythmia classification.

The contributions of the research work throughout the thesis have been published as the following list:

Journal:

Chen, H, Maharatna, K, "An Automatic R and T peak Detection Method Based on the Combination of Hierarchical Clustering and Discrete Wavelet Transform" IEEE Journal of Biomedical and Health Informatics (*doi* : 10.1109/*JBHI*.2020.2973982).

Chen, H, Das, S, Morgan, J.M, Maharatna, K, "An effective PSR-based arrhythmia classifier using self-similarity analysis" Biomedical Signal Processing and Control (*doi* : 10.1016/*j.bspc*.2021.102851).

Chen, H, Wiles, B.M, Roberts, P.R, Morgan, J.M, Maharatna, K, "A New Algorithm to Reduce T-wave Over-sensing based on Phase Space Reconstruction in S-ICD system" Computers in Biology and Medicine (*doi* : 10.1016/*j.compbiomed*.2021.104804).

Chen, H, Das, S, Morgan, J.M, Maharatna, K, "Prediction and Classification of ventricular arrhythmia based on phase-space reconstruction and fuzzy c-means clustering" Computers in Biology and Medicine (*doi.org*/10.1016/*j.compbiomed*.2021.105180).

Wiles, B.M, Roberts, P.R, Allavatam, V, Acharyya, A, Vemishetty, N, EIRefai, M, Wilson, D.G, Maharatna, K, **Chen, H**, Morgan, J.M, "Personalised S-ICD sensing vectors generated by mathematical rotation increase S-ICD eligibility whilst preserving device performance" Europace (*doi.org*/10.1093/*europace*/*euab*310).

Conference:

Chen, H, Maharatna, K, "An automatic R-peak Detection Method Based on Hierarchical Clustering" IEEE Biomedical Circuits and Systems Conference (BioCAS), IEEE. 4 pp.(*doi* : 10.1109/*BIOCAS*.2019.8919208).

Wiles, B.M, Roberts, P.R, Allavatam, V, Maharatna, K, Acharyya, A, **Chen, H**, Vemishetty, N, Wilson, D.G and Morgan, J.M, 2018. The future of S-ICD sensing: improve significantly increases R: T ratio and generates universal device eligibility without impairing vf detection. EUROPACE-LONDON-, 20(4), pp.iv1(*doi* : 10.1093/*europace*/*euy*200).

Dataset:

(2020) ECG R and T-peak detection. Code Ocean (*doi* : 10.24433/*co*.5608972.*v*1) [Dataset]

1.4 Thesis Outlines

The rest of the thesis is structured as follows, which is shown in Fig.1.1. In Chapter 2, we discussed the background and literature review of the heart and ECG, arrhythmia and signal processing of ECG. Firstly, the structure and basic operations of the heart and the heart activities with the corresponding ECG waves are presented. Secondly, the introduction of several types of arrhythmias are reviewed. Finally discussions of ECG

pre-processing, ECG feature extraction and the methods for arrhythmia detection and prediction are described.

Chapter 3 presents in detail the automated ECG feature extraction method. We first give a introduction of wavelet transform and preliminaries of the discrete wavelet transform. Then we present the basic introduction of clustering algorithms and a detailed description of hierarchical clustering. Next, The hierarchical clustering is used to detect R-peak, and then identify the QRS boundary based on the mean square error. Finally we applied discrete wavelet transform with modulus-maxima analysis method to determine T-peak. The MIT-BIH and QT databases with 15 one-minute records from University Hospital Southampton were used to validate our method. We also compared our algorithm with the algorithm mentioned in the literature. Our method represented a comparable and higher performance for ECG feature extraction.

In Chapter 4, we describe the S-ICD system and phase-space reconstruction with box-counting techniques. Then, it gives a detailed discussion on development of phase-space reconstruction and box-counting techniques to reduce T-wave over-sensing after using hierarchical clustering Chen and Maharatna (2020). We tested our algorithm for 34 records from UHS and all records from the MIT-BIH arrhythmia database. The results showed it has the potential to reduce inappropriate shock therapies in S-ICD recipients.

In Chapter 5, first the phase-space reconstruction, box-counting techniques and Fuzzy c-means clustering are reviewed. Then, it gives a detailed discussion on development of phase-space reconstruction and box-counting techniques to extract ECG features, which were used to formulate a risk index to predict an impending ventricular arrhythmia. It also showed a novel method based on Fuzzy c-means clustering to classify the impending ventricular arrhythmias. We tested our algorithm for both healthy subjects in PTBDB and arrhythmic subjects in CUDB.

In Chapter 6, first the PSR diagrams of different ECG signals with different time delay are reviewed. Then, it gives a detailed discussion on extraction of PSR area features, which are used to classify arrhythmias. 4 different databases were used for validation of our proposed method. It also contains the computational complexity analysis of our proposed method.

Chapter 7 summarises the findings and contributions discussed in this thesis. Future work is also outlined finally.

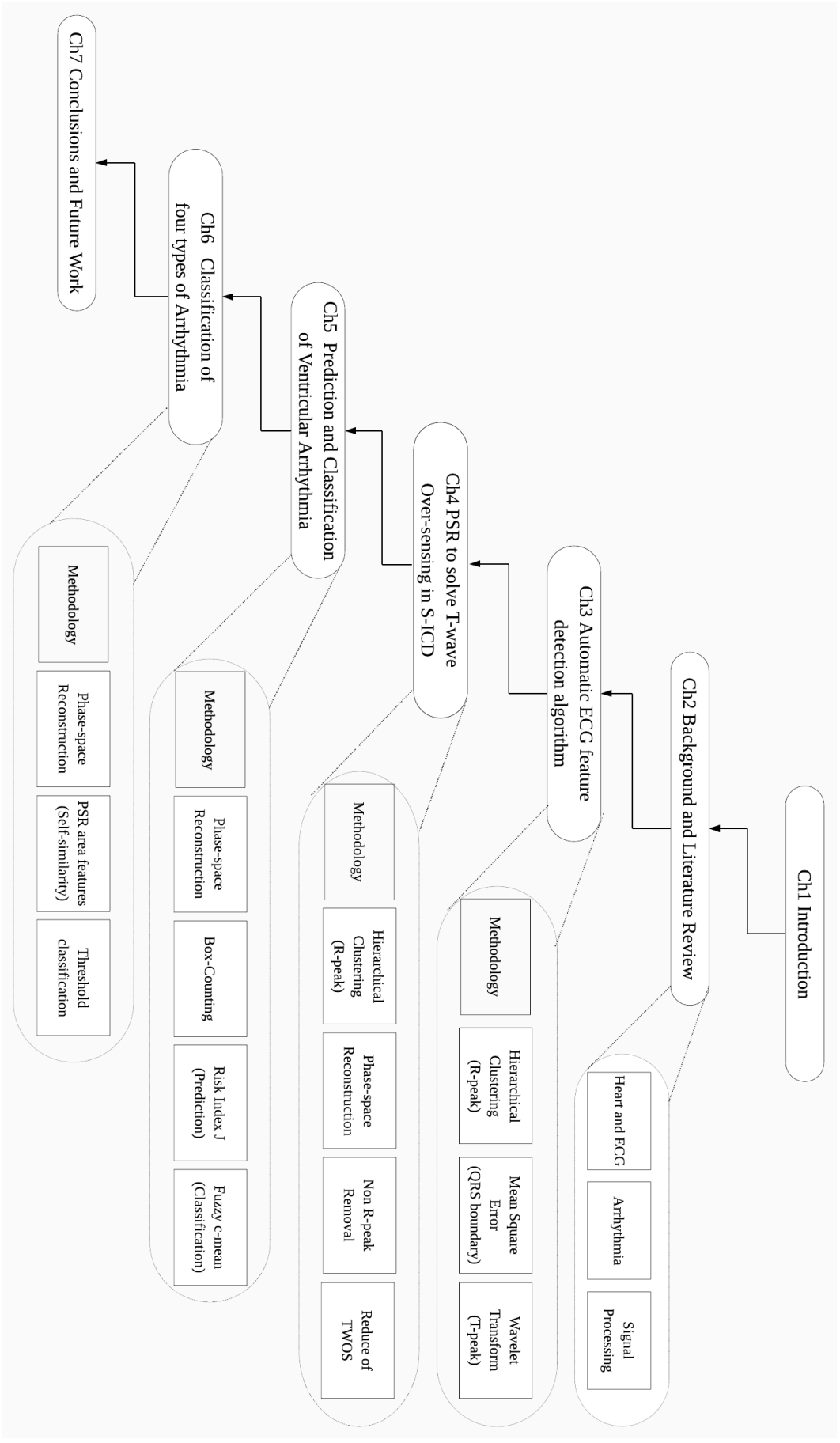

FIGURE 1.1: The structure of the Thesis

Chapter 2

Background and Literature Review

2.1 The Heart

2.1.1 The Heart Structure

A human heart is a muscular organ that pumps blood to the body. It is comprised of four chambers: the right and left atria, and the right and left ventricles - Figure 2.1 shows an anterior view of the heart. The main function of the heart is to circulate the blood, acting as a synchronized reciprocating double-pump NIH (2015b). In every heartbeat, blood is squeezed into the arteries from the heart and then returns back to the heart in a one-way circuit through the veins. First the left atrium receives oxygenated blood from the lung via the pulmonary veins, and empties into the left ventricle through mitral valves. From there, the left ventricle injects the blood into the whole body via the aorta. The peripheral circulation system consumes the oxygen and nutrition, and then returns the blood with carbon dioxide as well as waste back to the right atrium via the superior/inferior vena cava. The right atrium then pulls the deoxygenated blood into the right ventricle through the tricuspid valve. After that, the right ventricle forces the blood through the semilunar valve and pulmonary arteries into the lung, where oxygen diffuses into the blood and is exchanged for carbon dioxide. The delivery of the oxygen and nutrients takes place in the connection between arteries and veins, known as the capillary network, which consisted of micro vessels Mohammadi and Fradet (2017).

[1] Figure is extracted from: https://commons.wikimedia.org/wiki/File:Heart_diagram-de.svg under license CC BY-SA-3.0

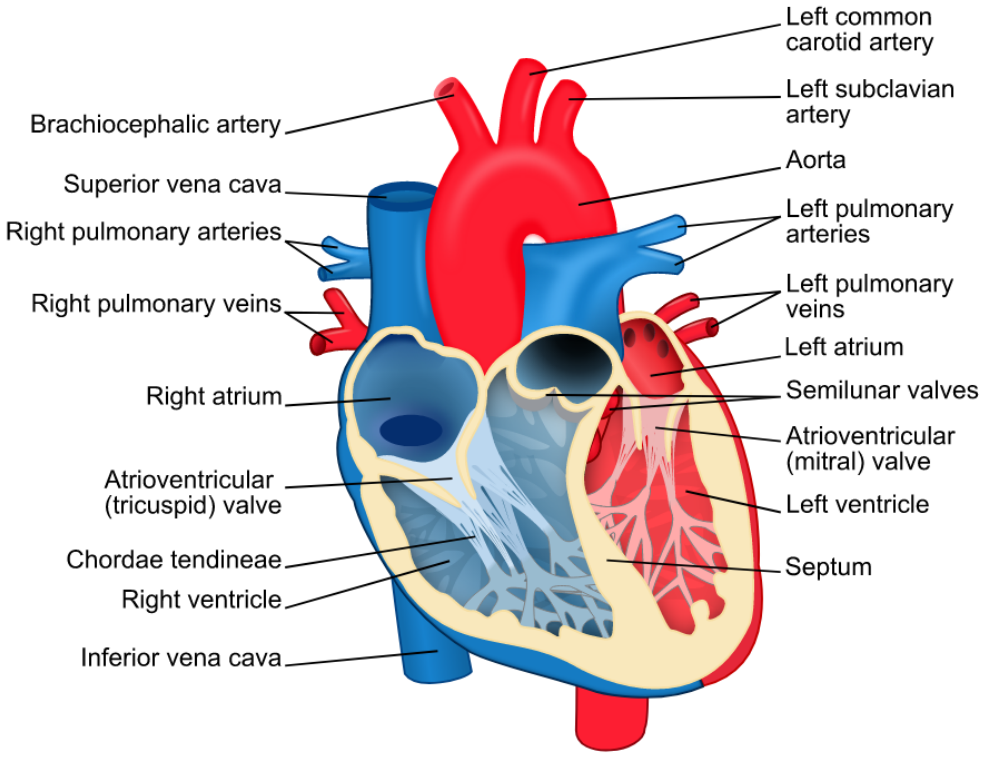

FIGURE 2.1: Structure of the heart[1]

2.1.2 Electrical Conduction System

The rhythmic contraction of the heart occurs due to the forces by electrical impulses known as action potentials. In general, electrical signal propagation through heart follows a specific path which is referred to as the electrical conduction system (see Figure 2.2). It consists of specialized heart muscle cells. These specialized cells have two main functions, some cells is used to pacemaking, and function of the other cells is to propagate the electrical current through them.

As shown in Figure 2.2, everything starts with an electrical impulse generated at the sinoatrial (SA) node. The SA node is a specialized muscle cell that located at the right upper chamber and generates the electrical impulse regularly at a rate of 60 to 100 per minute. Then the electrical signal propagates throughout the atria and reaches the atrioventricular (AV) node. The AV node is located in the wall of the right atrium and composed of highly specialized conducting tissues. Its function is to slow down the conduction from the atria to the ventricles. This allows sufficient time to complete atrial depolarization and contraction before the depolarization and contraction of ventricles. Next, the impulse enters the base of the ventricle at the Bundle of His from where it follows the Left and Right bundle branches along the interventricular septum. At the

[2]Figure is extracted from: https://commons.wikimedia.org/wiki/File:Conductionsystemoftheheart.png under license CC BY-3.0

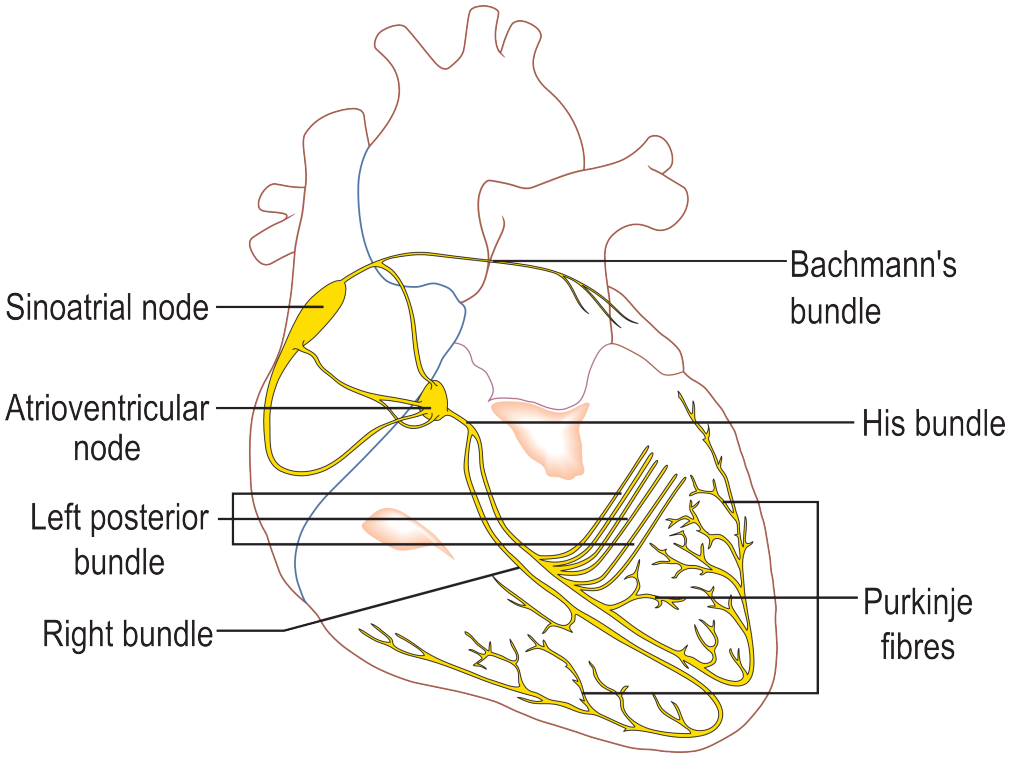

FIGURE 2.2: The electrical conduction system of the heart[2]

end, the bundle branches divide into Purkinje fibers which is the extensive system of fibers directly innervating the myocardial cells.

2.2 Electrocardiogram(ECG)

2.2.1 Components of the ECG

the heart activity can be considered as propagation of electrical impulses and therefore, any abnormality in heart function is reflected in this electrical impulse propagation characteristics. This could be measured by attaching electrodes to the surface of the body skin and recording the electrical activity by a device. Such recording is generally referred as Electrocardiogram (ECG) and it plays a significant role in day-to-day clinical practice for detecting arrhythmias since the Cardiologists can obtain critical signs of malfunction of heart from ECG signal. In general, as shown in Figure 2.3, one normal ECG beat consists of the P-QRS-T and U waves and the relevant ECG features, such as PR interval, QT interval, QRS complex as well as ST segment and PR segment.

In the following, a separate description of each of the components will be given to summarize their characteristics and the corresponding cardiac events.

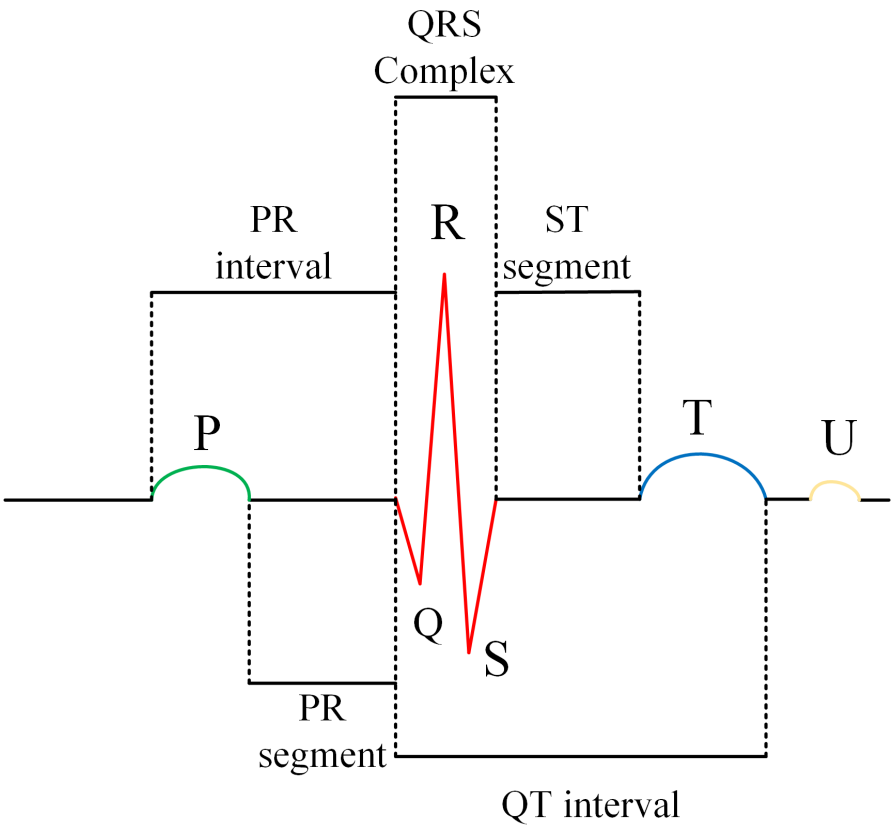

FIGURE 2.3: A normal ECG period

- P wave:The first wave in an ECG is called P wave which is generated due to electrical activity through the Atria. The normal duration of the P wave is shorter than 80 milliseconds (ms).
- PR interval:It is identified as the time for electrical impulse to travel from SA to AV node. The normal duration can vary between 120 and 200 ms.
- PR segment: It essentially represents the spread of depolarization through the AV node, the bundle of His, and bundle branches and normally is displayed as a flat line.
- QRS complex: This represents the activity of the ventricles and seen as three closely related waves on the ECG (Q, R and S wave). Normally, the duration which is measured from the beginning of the QRS complex to its end is 0.08 to 0.10 seconds.
- ST segment:It starts at the end of the S wave and finishes at the start of the T wave. It is an isoelectric line that represents the time between depolarization and repolarization of the ventricles.

- T wave: It is seen as a small wave after the QRS complex that represents ventricular repolarization. Normal duration of the T wave can vary close to the 160 ms.
- QT interval: It starts at the beginning of the QRS complex and finishes at the end of the T wave. It represents the time taken for the ventricles to depolarize and then repolarize.
- U wave: Normally hypothesized to be caused by repolarization of interventricular septum.

The following section is to explain how the ECG is constructed. In above section, eight different temporal states are shown. Each of them corresponds to the sequential status of the heart during a heart cycle. Figure 2.4 shows the shape of electrical signal within heart. It is evident that different parts of the conduction system give rise to varied action potentials at different times and different locations. The relationship between these action potentials is clearly shown as an ECG in color.

All the above-mentioned features could be used for diagnosing atypical heart functions in clinical practice. In addition, a specturm analysis of normal electrocardiograms is performed to analyse the normal PQRST complex and its individual components. The highest amplitude of normal P and T waves occurred at 5Hz, the power spectrum of an individual QRS complex can be found in the 0 to 20Hz frequencies and the maximum amplitude normally occurred at 15Hz Lin (2008).

2.2.2 The Lead System

As mentioned earlier, the ECG is recorded by a device with electrodes attaching to the body skin. The whole set-up is generally called the lead system. The first 'standard' ECG consisted of only the three limb leads is introduced by Einthoven in 1931 Papouchado et al. (1987). Around 3 years later, Wilson and Goldberger developed the ECG lead system. The standard 12-lead combined the lead systems from Einthoven, Wilson and Goldberger. Finally it evolved in mid-1940s Papouchado et al. (1987).

Figure 2.5 and Figure 2.6 illustrate the standard 12-lead system on a human body. Commonly, 10 electrodes attached to the body are used to form 12 ECG leads, with each lead measuring a specific electrical potential difference. Each lead refers to an imaginary line between two different ECG electrodes. All leads can be divided into three main types which are limb leads, augmented limb leads and precordial leads.

Leads I, II and III are called the limb leads. The top three of Figure 2.5 illustrates these limb leads on a human body. The electrodes that form these signals are located on the

[3]Figure is extracted from: https://commons.wikimedia.org/wiki/File:Limb_leads_of_EKG.png under license CC SA-BY-4.0

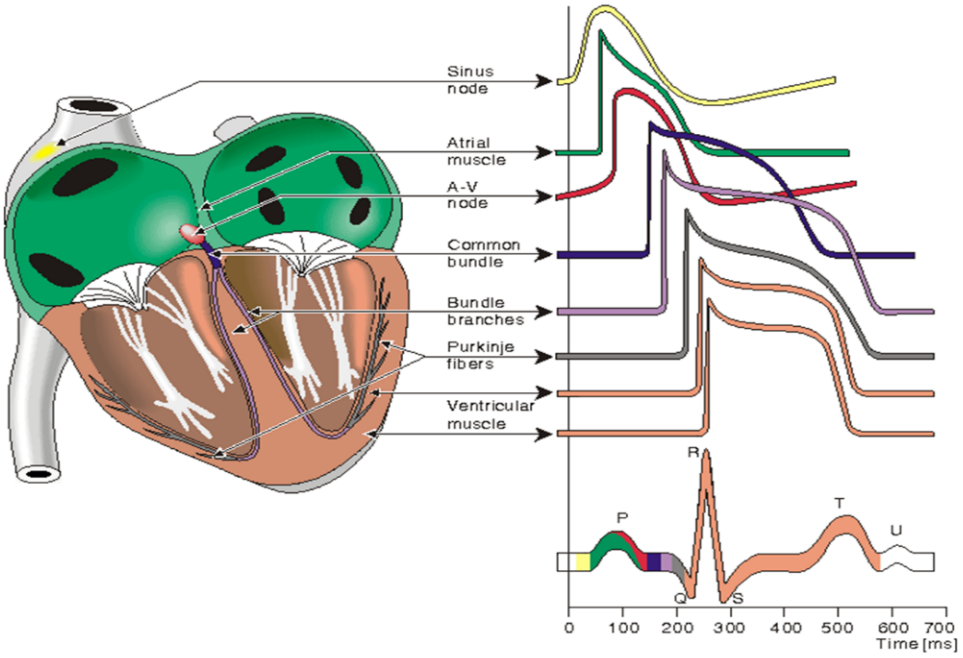

FIGURE 2.4: The electrical conduction system of the heart, with detailed morphology and timing of ECG signal from different parts of the heart and ultimately leading to the form of an ECG heartbeat Belyakin and SS (2019)

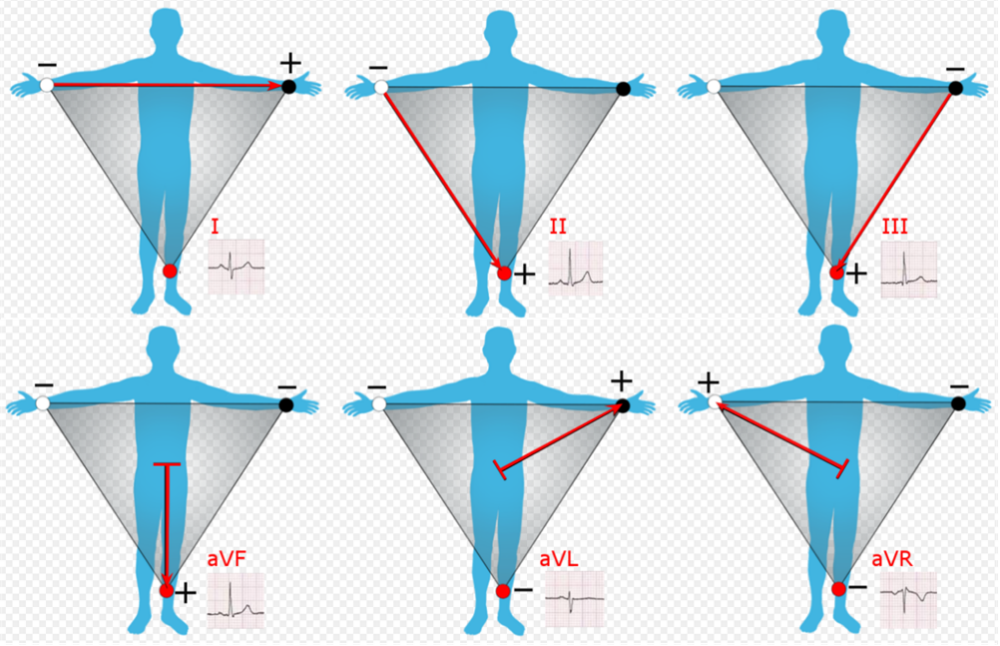

FIGURE 2.5: The limb lead diagram(Top) and the augmented lead diagram(Bottom)[3]

limbs – one on each arm and one on the left leg. Lead I is the voltage between the (positive) left arm (LA) electrode and right arm (RA) electrode. Lead II is calculated as the voltage between left leg (LL) electrode and right arm (RA) electrode and lead III represents the voltage from left leg (LL) electrode to left arm (LA) electrode. The mathematical equations of the voltage recorded for three limb leads are shown in (2.1), (2.2) and (2.3) respectively.

$$I = LA - RA \tag{2.1}$$

$$II = LL - RA \tag{2.2}$$

$$III = LL - LA \tag{2.3}$$

On the other hand, augmented limb leads are divided into augmented vector right (aVR), augmented vector left (aVL) and augmented vector foot (aVF). The augmented limb lead diagram is shown on the bottom of the Figure 2.5. They are derived from the same three electrodes as leads I, II, and III. In terms of the aVR, it has the positive electrode on the right arm, the negative pole is a combination of the left arm and left leg electrodes. Lead aVL has the positive electrode on the left arm with the combined negative pole of right arm electrode and left leg. Finally, Lead aVF has the positive electrode on the left leg and the negative electrode is the combination of right and left arm electrodes. Following gives the mathematical equations of the voltage recorded for three limb leads, namely aVR, aVL and aVF in (2.4), (2.5) and (2.6) respectively. .

$$LeadaVR = RA - \frac{1}{2}(LA + LL) \tag{2.4}$$

$$LeadaVL = LA - \frac{1}{2}(RA + LL) \tag{2.5}$$

$$LeadaVF = LL - \frac{1}{2}(RA + LA) \tag{2.6}$$

A more insightful view of the standard 12-lead system is shown in Figure 2.7. From there the spatial relationship between each participating lead is mapped and linked with respect to the origin. The cardiac vector generated in three-dimensional space is projected onto those leads. At each instant of time, each lead reveals the projected magnitude of the vector. It is possible to see because the directions of the cardiac vectors are different, the ECG records of all leads are different as shown on the right panel of Figure 2.7.

[4]Figure is extracted from: https://commons.wikimedia.org/wiki/File:Precordial_Leads.svg

[5]Figure is extracted from: https://commons.wikimedia.org/wiki/File:EKG_leads.png under license CC BY-SA-4.0

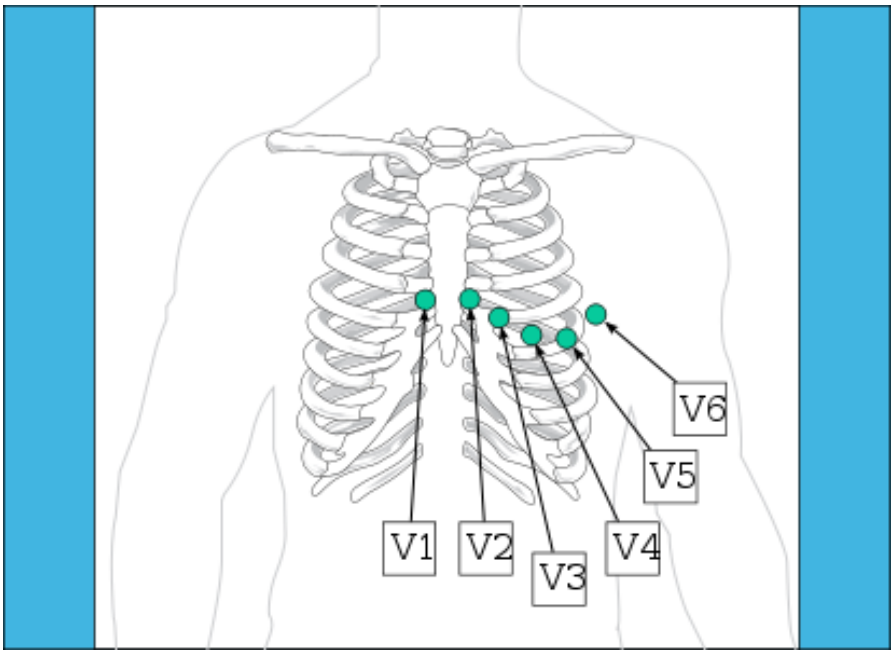

FIGURE 2.6: The precordial leads position on the torso[4]

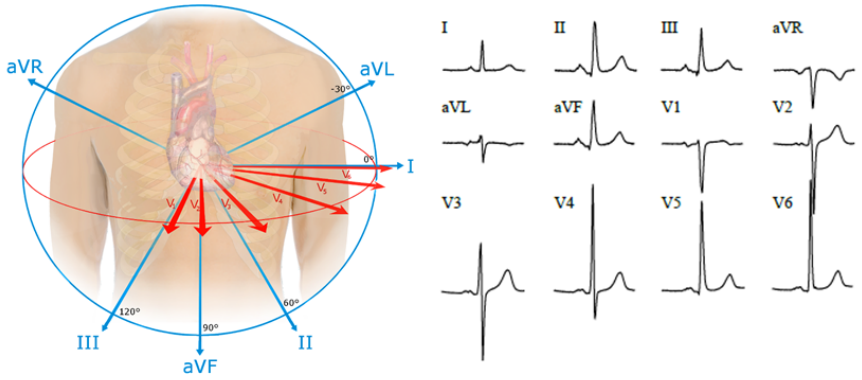

FIGURE 2.7: Spatial orientation of 12 leads, with a panel of time sequences on the right showing one heart beat simultaneously recorded by different leads for a typical normal patient[5]

2.3 Arrhythmia

As mentioned earlier, a healthy heart supplies the human body with the right amount of blood at the rate needed to work normal. In general, a heartbeat should be 60 to 100 times per minute NIH (2015a). However, if disease or injury weakens the human heart, the rhythm of heart will be abnormal, which is known as arrhythmia. There are two major categories of arrhythmia based on the heart rate. Tachycardia is one broad category of arrhythmia that is a heart rate that exceeds the normal resting rate. On the other hand, arrhythmia which leads to the slow heart rate is defined as bradycardia Alliance (2019). In the following subsection, we present discussion about different types of arrhythmias.

2.3.1 Premature (Extra) Beats

Premature Beats consist of Premature (Extra) Atrial Contractions (PACs) and Premature Ventricular Contractions (PVCs) also called Ventricular Premature beats(VPBs). PACs are extra beats that occur in the atria. In most cases, they are harmless without any symptoms. Therefore normally they do not require treatment NIH (2015a). On the other hand, premature beats that originate in the lower chambers (ventricles) are defined as PVCs. An ECG example of PVCs is shown in Figure 2.8. The main characteristic of PVCs is the compensatory pause following the contraction. The extra action potential causes the SA node to become refractory to generating its next scheduled beat, and thus it must "skip a beat" and will resume exactly two P-P intervals after the last normal sinus beat. For some people, PVCs can happen because of too much exercise and they are also relative with stress and too much caffeine or nicotine. Sometimes, heart disease or electrolyte imbalance can also lead to PVCs. However, in most people, the hazard of PVCs can be negligible NIH (2015a).

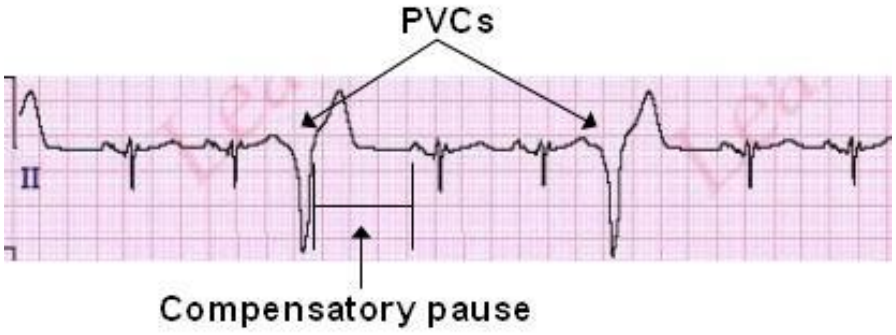

FIGURE 2.8: The ECG record of PVCs from Lead II CARDIOLOGYreview (2021b)

2.3.2 Supraventricular Arrhythmias

Another category of arrhythmias called Supraventricular Arrhythmias can be divided into Atrial Fibrillation (AF), Atrial Flutter (AFL) and Paroxysmal Supraventricular Tachycardia (PSVT). AF is a common type of arrhythmias that involves a fast and irregular heart rhythm and can cause the abnormal contraction of atria. An example of ECG records of Atrial Fibrillation and Atrial Flutter is given in Figure 2.9.

2.3.2.1 Atrial Fibrillation (AF)

In AF, the heart's electrical impulses originate in another position of the atria instead of the sinoatrial (SA) node. Moreover, the heart's electrical impulses travel through the whole atria rapidly rather than a normal way, which may cause the atrial wall beats very fast. In result, the atria are not capable of pumping blood into the ventricle in a

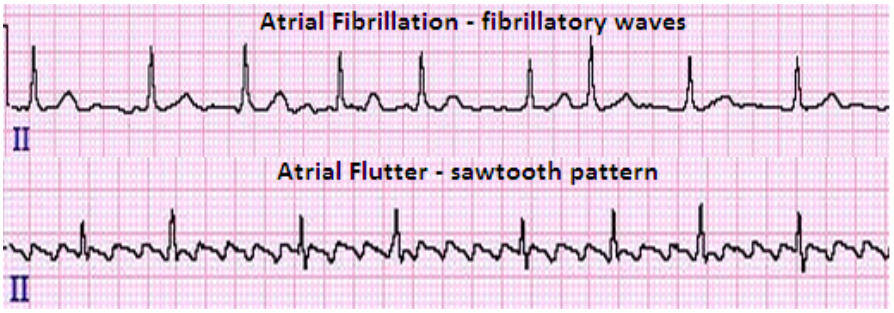

FIGURE 2.9: The ECG records of Atrial Fibrillation and Atrial Flutter from Lead II CARDIOLOGYreview (2021a)

right way NIH (2015a). The major causes of AF are high blood pressure, inflammation and coronary heart disease. In addition, an early research Krahn et al. (1995) proposed that the risk of AF is strongly associated with age. The advancing age can lead to the higher incidence of AF.

2.3.2.2 Atrial Flutter (AFL)

AFL is an arrhythmia that is like the AF. AF usually involves a rapid and irregular heart rhythm, however, in AFL, the electrical impulses travel throughout the atria with fast and regular heart rhythm. It occurs due to one or more rapid circuits in the atrium and usually can be found in people with heart disease or after cardiac surgery MedicineNet (2018).

2.3.2.3 Paroxysmal Supraventricular Tachycardia (PSVT)

It is a rapid heart rate that occurs in a part of heart above the ventricles. PSVT begins and ends during a short time and normally with a regular rhythm. The cause is the abnormal electrical connection between the atria and the ventricle. Accessory pathway tachycardia as a special type of PSVT, usually happens because of an extra pathway between the atria and ventricle. The electrical impulses can go through the normal route and the extra pathway simultaneously. Therefore, the electrical impulses can quickly travel through the whole heart and turn out the rapid heart rates. Another type of PSVT is AV nodal reentrant tachycardia, it occurs when a reentrant circuit is present within the AV node itself. In this situation, there are two separate conduction pathways within the AV node instead of just one MedicineNet (2018).

2.3.3 Ventricular Arrhythmias

Ventricular Arrhythmias are the most dangerous category of arrhythmias and normally composed of Ventricular Tachycardia (VT) and Ventricular Fibrillation (VF). VT can

occur with many variations of the QRS morphology, depending on where the arrhythmia originates, which sometimes makes diagnosis on ECG challenging. Figure 2.10 shows two examples of VT with different QRS morphologies — one with a right bundle branch block morphology and one with a left bundle branch block morphology. And an example of VF is shown in Figure 2.11.

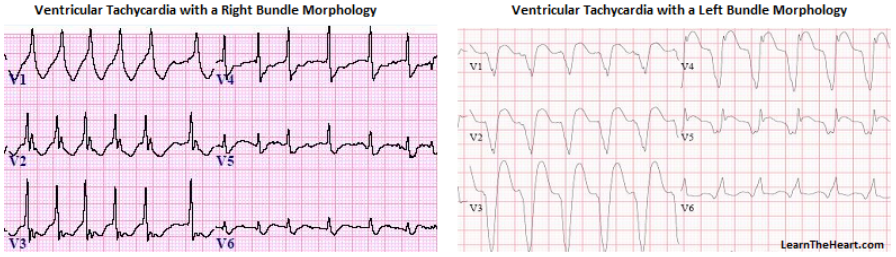

FIGURE 2.10: The ECG records of ventricular tachycardia with right and left bundle branch block from Lead V1 to V6 CARDIOLOGYreview (2021d)

FIGURE 2.11: The ECG records of ventricular fibrillation from Lead V1, II and V6 CARDIOLOGYreview (2021c)

2.3.3.1 Ventricular Tachycardia (VT)

It is defined as a rapid and regular heart rhythm originating from the ventricle that usually lasts for a few seconds. A short time VT normally cannot cause any heart problem. However, VT can change into some serious arrhythmias, for example ventricular fibrillation when VT episodes for more than a few seconds MedicineNet (2018). In addition, Harris and Lysitsas (2015) proposes another definition of VT. In Harris and Lysitsas (2015) , VT is represented when three or more consecutive heart beats occur in the ventricle with cycle length larger than 100 beats every minute. Also, it suggests that VT should be independent with conduction of atria and AV node. There are several causes can lead to VT. For example, the problem in the transition zone from the heart to pulmonary arteries can cause right ventricular outflow tract tachycardia (RVOT) and some genetic defects in heart's cells may lead to VT Healthcentral (2005). According to an early research Dungan et al. (1981), VT also can happen because of the arrhythmogenic right ventricular dysplasia (ARVD).

2.3.3.2 Ventricular Fibrillation (VF)

It is defined as a chaotic and rapid heart rate with variable speed up to 300 beats per minute Harris and Lysitsas (2015). In MedicineNet (2018) , VF can also be considered as a disorganized electrical signal originating from the ventricle. It causes the ventricle quiver and hence the ventricle cannot pump blood to the body. This situation turns out sudden cardiac arrest or death within a few minutes NIH (2015a). However, the cause of VF is still poorly understood. There are two common causes, first is a scar of the heart's muscle tissue, which might have resulted from a previous heart attack. Another cause is the abnormal electrical heart impulses spread throughout the heart after the first heart attack MayoClinic (2018). In some cases, VF begins as a ventricular tachycardia (VT). A research Harris and Lysitsas (2015) also mentioned the prolonged VT can be considered as a risk factor. In addition, the iatrogenic pacing of the myocardium can also lead to VF, which is represented by the increasing amplitude of the T wave in ECG.

2.3.4 Bradyarrhythmia

The last type of arrhythmias is Bradyarrhythmia. For adults, bradyarrhythmia is defined as a heart rate slower than the normal situation (60 beats every minute). Normal, bradyarrhythmias can be caused by heart attacks. In some cases, bradyarrhythmias happen due to the imbalance of chemical substances in the blood NIH (2015a). Moreover, Epstein et al. (2008) proposed bradyarrhythmias are associated with sinus node dysfunction (SND) and the incidence of bradyarrhythmias is high after cardiac transplantation. An early report Grinstead et al. (1991) showed that some of the significant bradyarrhythmias may cause sudden death. The Figure 2.12 shows the difference of ECGs between normal rhythm, bradycardia and tachycardia. On the contrary, tachycardia is a condition when the heart rate is faster than the normal situation.

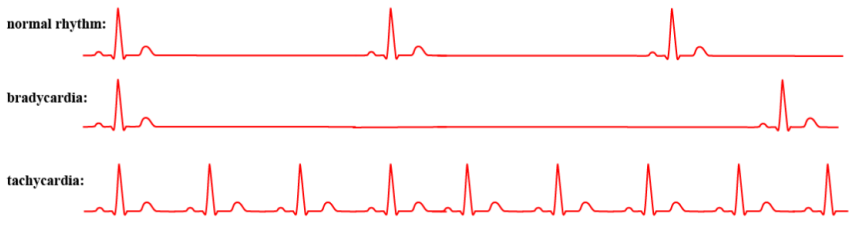

FIGURE 2.12: The difference of ECGs between normal rhythm, bradycardia and tachycardia

2.4 Signal Processing

2.4.1 ECG Pre-processing

Pre-processing is clearly required in ECG applications since ECG is affected by various kind of noises. Normally, these noises can be divided into four main types which are power line interference, Electromyography (EMG) artefact, electrode contact noise and baseline wandering. The following sections will give introduction of these noises and the corresponding removal methods.

2.4.1.1 Power Line Interference

Electromagnetic field from nearby machinery is one of the common causes of power line interference in the ECG. This normally consist of 50/60 Hz sinusoidal interference. Such noise can corrupt the ECG recordings and make a difficulty for analysis of ECG features with high-frequency. Therefore, it is extremely important to remove power line interference. Several techniques are commonly used to handle it, for example adaptive filter. A detailed example of adaptive filter based on least mean squares (LMS) algorithm can be found in Thalkar and Upasani (2013). The advantages of adaptive filter are fast filtering response and small residual errors, however this method requires reference signal which may cause poor efficiency of the filtering processing. Another novel robust nonlinear aggregation operator was introduced in Leski (2021). The advantages of this method includes higher efficiency of power-line interference suppression, lower sensitivity of filter parameters and the suppression of disturbances from variable amplitude.

2.4.1.2 Motion/EMG Noise

This noise occurs due to muscle activity during an ECG recording especially in a stress test. This artifact consist of maximum frequency of 10 KHz. This type of noise contains frequency contents that spread through the ECG frequency spectrum, making it extremely difficult to handle. A wavelet threshold method was first reported in Donoho (1995) to reduce the noise effect. Tayel et al. (2018) developed a new multi-stage kernel filtering based approach to effectively the EMG artifact. This method combined KernelRecursive Least Squares Tracker (KRLST) and Kernel Recursive Least Squares with Approximate Linear Dependency (ALDKRLS) algorithms to not only adequately attenuate the EMG noise but also preserve the tiny features of the originally ECG signal.

2.4.1.3 Electrode Contact Noise

It is the movement of the electrode away from the contact area on the skin that leads to variations in the impedance between the electrode and skin causing potential variations in the ECG. Some methods have been developed to tackle this problem, such as weighted adaptive noise canceling and recursive Hampel filter Ghaleb et al. (2018), novel skin-stretch estimation approach Kalra and Lowe (2020) and stationary wavelet transform (SWT) Nagai et al. (2017).

2.4.1.4 Baseline Wandering

A baseline wandering is very low but unwanted frequency contents in ECG signal recordings caused by respiration, body movements and skin-electrode impedance Chatterjee et al. (2020). It is usually lying close to 0.5 Hz. It can affect the analysis of low-frequency components in ECG, such as ST segments Malhotra and Chintanpalli (2020). Therefore, it is necessary to remove baseline wandering before ECG signal processing. A conventional method based on FIR digital filter is proposed in Dai and Lian (2009). And Raj et al. (2021) introduced a high-speed IIR filter to remove baseline wandering. In addition to these traditional filtering methods, the other novel algorithms from Rahman et al. (2017) and Eisner et al. (2019) are based on one of the following techniques: path finding algorithm and phase space mapping.

2.4.2 ECG Feature Extraction

The most useful information in the ECG is normally derived from the amplitudes and intervals that are defined by the fiducial points of ECG wave (e.g. onset, offset, peak). In general, these features are used to classify the normal and abnormal heartbeats (Arrhythmias) and accordingly produce an alarm. Therefore, it is necessary to find some methods to extract such ECG features. Recently, Many research papers have presented various methods to achieve feature extraction of ECG. In general, there are two main groups of ECG feature extraction algorithms, which are QRS detection algorithms and other wave delineation algorithms Martínez et al. (2004).

2.4.2.1 QRS detection algorithm

The QRS detection is the primary task of the ECG feature extraction because it is the most characteristic waveform of the ECG signal. The properties of the QRS complex, which are high amplitude and specific morphology, makes QRS detection easier than the other waves. Thus, it is usually used as a reference in the ECG signal. Pan and Tompkins first introduced a conventional method named pan-tompkins algorithm based

on the digital band-pass filter to detect QRS complex Pan and Tompkins (1985). An extensive review of the QRS detection algorithms was reported in Martis et al. (2014). There are other attempts for QRS detection based on time domain morphology and gradient method Mazomenos et al. (2012), shannon energy envelope (SEE) Manikandan and Soman (2012). In addition, the wavelet transform is widely used to detect the QRS complex. The study in Martínez et al. (2004) suggested using the discrete wavelet transform to identify the QRS complex. Recently, many research presented QRS detection algorithms with lower computation burden. A QRS detection method with low- complexity in individual ECG beat named hybrid feature extraction algorithm that based on the discrete wavelet transform was introduced in Mazomenos et al. (2013). Other WT-based algorithms are shown in Merah et al. (2015) Thiamchoo and Phukpattaranont (2016) Thungtong (2017) and Smaoui et al. (2017). Hou et al. (2018) defined a real-time QRS detection method based on phase portraits and box-scoring calculation. Optimized adaptive thresholding Saadi et al. (2015), iterative state machines Zalabarria et al. (2020), and moving-average filters Elgendi (2013) are also presented to detect QRS complex.

2.4.2.2 Wave delineation algorithm

The main objective of these algorithms is to determine the peaks and boundaries of the individual QRS complexes, P and T waves. In general, these algorithms estimate the location of the QRS complex initially and then define the time windows before and after the QRS fiducial point (onset and offset) to detect the P and T waves. The locations of P and T waves onsets, peaks and offsets are difficult to determine because the amplitudes of the noises can be higher than the P and T waves. In this situation, it is necessary to apply some techniques to enhance the characteristic features of the P and T waves. The existing literature on ECG wave delineation algorithms is extensive and focuses particularly on frequency aspect. Some methods are used to extract ECG wave features in the frequency band, such as discrete wavelet transform (DWT) (e.g. Martínez et al. (2004),Mazomenos et al. (2013),Cesari et al. (2017) and Ghaffari et al. (2009)). Another study in de Lannoy et al. (2009) combined wavelet transform and hybrid hidden Markov models to identify the ECG waveforms. Using these approaches based on the wavelet transform, researchers have been able to extract morphological information of the ECG waves in both frequency and time domains. A study in Martínez et al. (2010) suggested a new ECG delineator based on the phasor transform. In recent years, there has been an increasing amount of literature on ECG wave delineation based on machine learning algorithms. As noted by a study in Saini et al. (2013), the K nearest neighbour (KNN) algorithm is efficient to locate the ECG waveform boundaries because the KNN algorithm is simple to apply and can be realized easily. The study in Hajimolahoseini et al. (2018) pointed out that ECG wave delineation can be achieved by using an unsupervised learning algorithm based on expectation maximization. In

addition to the above methods, moving-average filtersElgendi et al. (2015) Elgendi et al. (2016), morphological mathmatical filtering with Elgendi's algorithm Friganovic et al. (2018) and the correlation analysis-based method Homaeinezhad et al. (2014) have also been proposed to detect ECG fiducial points.

2.4.3 Analysis of Arrhythmia using ECG

2.4.3.1 Detection or Classification of Arrhythmia

Recently, many researchers tried to use ECG features to detect or classify arrhythmia in order to improve patient's life quality. Pathoumvanh et al. (2014) and Übeyli (2009) are similar, they both considered the power spectrum as a feature from different ECG to detect arrhythmia. Pathoumvanh et al. (2014) suggested that discrete cosine transform (DCT) was applied to determine the power spectrum in the frequency domain. The energy compaction property of DCT allowed the ECG features representation in only low frequency components of DCT coefficients, which can be used to detect arrhythmia. Übeyli (2009) used Eigenvector methods to identify the relationship between power spectral density and frequency to detect arrhythmia. Recently, an ECG-based independent component analysis (ICA) method is proposed by Behar et al. (2019) to detect fetal cardiac arrhythmia.

Other researchers focused on finding a better classification algorithms, for example machine learning algorithms based on Artificial Neural Network (ANN) Gothwal et al. (2011), Support Vector Machine (SVM) Moavenian and Khorrami (2010); Li et al. (2013); Alonso-Atienza et al. (2013). Acharya et al. (2018) also suggested to use convolution neural network (CNN) to classify atrial fibrillation, atrial flutter and ventricular fibrillation. In addition to these machine learning based algorithm, there are other arrhythmia classification algorithms (based on the reviews from Roopaei et al. (2010); Balasundaram et al. (2013); Melin et al. (2014); Tripathy et al. (2016) and Amrani et al. (2018) based on one of the following techniques: thresholding method, binary classifier, Learning Vector Quantization (LVQ), random forest classifier and multi-canonical correlation analysis (MCCA). Mohanty et al. (2018) also developed a novel C4.5 classifier to detect and classify ventricular arrhythmia.

Besides, with the release of the public Physionet 2020/2021 ECG datasets Goldberger et al. (2000), many ECG classification algorithms has been proposed in Physionet computing in cardiology challenge 2021. For example EfficientNet-B3 based deep learning model Suh et al. (2021), Convolution-Free waveform transform Natarajan et al. (2021), ResNet deep neural network architecture Nejedly et al. (2021); Magni et al. (2021); Jing et al. (2021). These novel algorithms showed a better performance than CNNs for ECG classification.

2.4.3.2 Prediction of Arrhythmia

The occurrence of SCD leads to a massive death across the world. The detection or classification of fatal arrhythmia may not provide sufficient time for the doctor to stop SCD that is caused by VA. Therefore, the early prediction of VA becomes a vital task to prevent people from SCD in modern medicine. However, the common pattern of the impending VA is still an unconquered task. Many published papers proposed some techniques to try to find the common pattern for impending arrhythmia. For example Artificial Neural Network (ANN) Adams and Choi (2012) and Phase-space reconstruction (PSR) Cappiello et al. (2014). Besides, empirical mode decomposition (EMD) Riasi and Mohebbi (2015), radial basis function neural network (RBFNN) Kelwade and Salankar (2016) and naive Bayes classifier Bayasi et al. (2015) have also been successfully applied for arrhythmia prediction. However, all reports do not show the prediction time before arrhythmia onset. Hence, they can be only considered as a possible early detection rather than the actual prediction of the impending arrhythmia. Moreover, the prediction of arrhythmia can only achieve for the limited types of arrhythmia, some types of arrhythmia especially VA, are still difficult to early detection or prediction.

2.5 Concluding Remarks

In this chapter, the basic anatomy of the heart, its electrical condition system, as well as ECG and lead system have been introduced. Signal processing methods for ECG preprocessing and feature extraction have also been described. We have broadly reviewed a range of arrhythmia detection, classification and predication algorithms pertinent to the thesis and highlighted their shortcomings. In the next chapter, we will discuss the fundamental and important steps for automated ECG analysis and ECG feature extraction and consequently will describe a novel algorithm for the automated delineation of ECG fiducial points.

Chapter 3

Automatic Feature Extraction of ECG R and T-peaks

3.1 Introduction

The analysis of the ECG is widely applied in the diagnosis of heart disorders such as atrial fibrillationLin et al. (2010). The most useful information in the ECG is normally derived from the amplitudes and intervals of these dividual waves that are defined by the fiducial points (e.g. onset, offset, peak). In general, these features are used to classify the normal and abnormal heartbeats in this process of diagnosis of the specific heart disease, e.g. congestive heart failure (CHF) Yu and Lee (2012) and cardiac arrhythmia Yıldırım et al. (2018). Therefore, it is necessary to extract various features of ECG in order to diagnose the heart diseases. Among the ECG wave, the QRS complex is relatively easy to identify because of its specific morphology and high amplitude. However, the T wave delineation is a more challenging task, due to its low amplitude and possibly irregular morphology. In addition, noises such as baseline wandering and power line interference are main factors that can result in faulty T wave delineation.

Over the decade, a number of automated algorithm have been developed for ECG delineation, which has been introduced in Section 2.4.2. All these mentioned algorithms can be used to identify the ECG fiducial points. However, the major concern associated with these algorithms is their detection accuracy more importantly low positive predictivity ($+P$) caused by the large number of false-positives (FPs) of R-peak detection. In addition, current methods can be error-prone, especially cannot achieve satisfactory performance for T wave detection due to the variable morphology of the T wave Yochum et al. (2016). This is particularly important in Implantable Cardioverter Defibrillator (ICD) device where depending upon the detected R-R interval and a patient's heart is given high-voltage electrical shock if necessary. In this context, even more severe

problem is T-wave oversensing phenomenon, where T-peak is misidentified as an R-peak resulting to a wrong R-R interval calculation. This causes a delivery of an electrical shock even though the patient's heart rhythm is normal. Inspired by this fact, a novel automated ECG feature extraction algorithm based on the hierarchical clustering and discrete wavelet transform, which is specifically designed to detect R-peak and T-peak is proposed in this paper. The hierarchical clustering method is used to identify the R-peaks. Then, the T-wave boundaries are determined using the ECG template. Finally, the discrete wavelet transform is applied to obtain the DWT coefficients of the T waves, and the modulus-maxima analysis (MMA) method is employed to detect the T-peaks. The flow chart of our proposed algorithm is shown in Fig.3.1

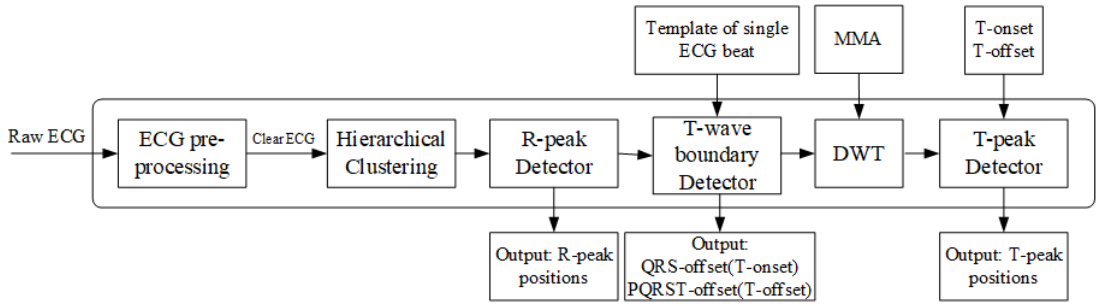

FIGURE 3.1: The system overview of the proposed algorithm

The rest of this chapter is organized as follows: in *Section* 3.2, we introduce the hierarchical clustering and DWT. After that, in *Section* 3.3 we discuss our proposed algorithm for ECG R-peak and T-peak detection. The performance of our proposed algorithm for R and T-peak detection based on three different databases are shown in *Section* 3.4. Finally, the conclusion are drawn in *Section* 3.5

3.2 Theoretical Background

3.2.1 Wavelet Transform

3.2.1.1 Introduction

In the early stages of signal processing, the Fourier Transform (FT) was first mentioned in 1807 Narasimhan (1999) and commonly used in order to analyse the signal in the frequency domain. However, FT cannot show any information in the time domain when a particular frequency occurs (non-stationary signal). To overcome this problem, researchers started to modify FT to work in a short time window for non-stationary signals and then the Short Time Fourier Transform (STFT) was discovered in 1946 by Gabor (1946). It is a Fourier-related transform which segments the original signal into several short intervals with the same length and then applies FT separately on each

of them. The length of each time window is small enough to satisfy valid stationarity. However, it exits resolution problem, which is to obtain the time information in non-stationary signal at the expense of frequency resolution. Since during analysis, the width of window in STFT is fixed leading to the unchanged time and frequency resolutions during the signal analysis. This makes it very difficult to observe in the time-frequency domain, particularly when low and high frequency components both exist within the same segment.

In this case, wavelet transform (WT) seems to be a solution that allows us to analyse the signal in different scale Chun-Lin (2010). A wavelet is a wave-like oscillation with an amplitude that begins at zero, increases or decreases, and then returns to zero one or more times. In formal terms, it is a wavelet series representation of a square-integrable function with respect to either a complete, orthonormal set of basis functions. Mathematically, WT is a convolution of the wavelet function with the signal. There are two ways to manipulate wavelet function during the convolution, which are time location shift, stretch or squeeze. In WT, the transform coefficients is direct proportion to the correlation between the wavelet function and the signal for a specific window, which means a better match can lead to a higher transform coefficient. On the other side, a poor match of the wavelet function to the shape of the original signal results in lower transform coefficients.

The wavelet transform can be divided into Continuous Wavelet Transform (CWT) and Discrete Wavelet Transform (DWT), which are manipulated in continuous and discrete steps respectively. In general, the representation of CWT can be shown in (3.1). Where a is scaling factor and b represents time shift factor, $\varphi^*(t)$ is the mother wavelet and it must satisfy an admissibility criterion (loosely speaking, a kind of half-differentiability) in order to get a stably invertible transform. Finally, the $X_{a,b}$ is the outcome of the signal $x(t)$. There leads to an important idea named scale. The concept of scale can be understood by considering a window of different sizes of scale, if a window is stretched to a larger window, the features could be found in this window are grosser, hence the higher scale leads to a larger window with a lower frequency, or vice versa. In addition, as mentioned before, wavelet function can be done by time shift, stretch or squeeze. Here from the (3.1), it is known that time shift factor b is relative with time shift and the change of scaling factor a can be considered as the stretch or squeeze. Along with the increase of scaling factor a, wavelets are stretched and then the lower frequency will be analysed, the reduction if a leads to the squeezed wavelets with higher frequency.

$$X_{a,b} = \frac{1}{\sqrt{a}} \int_{-\infty}^{\infty} x(t)\varphi^*(\frac{(t-b)}{a})dt \tag{3.1}$$

It can be seen that WT analyses the signal at different frequencies with different resolutions, this renders WT to preserve both time and frequency informations that resolved

unequally of resolution problem in contrast to STFT. The comparison of resolution between STFT and WT is given in Figure 3.2. It can be demonstrated that STFT has a fixed resolution. This allows to lend STFT sufficiently to one side of resolution, however, it will lose another side of resolution at its expense. It is also observed that the resolution of WT is different for different frequencies. Here the width of the window box relates to how the signal is represented. A wide box represents good frequency resolution with poor time resolution. On the other side, a narrower box gives bad frequency resolution and good time resolution. From the right of Figure 3.2, the window box with long width exists in large scale (low frequency) and the narrow box is in small scale (high frequency), which means WT represents bad frequency resolution and good time resolution at high frequencies, and shows the good frequency resolution and poor time resolution at low frequencies. This help us to analysis such non-stationary signal effectively, especially in cases when low frequency signals exist in a long time window whiles high frequency components exist for short durations. Biomedical signals like the ECG are extremely fitted in the field of WT application.

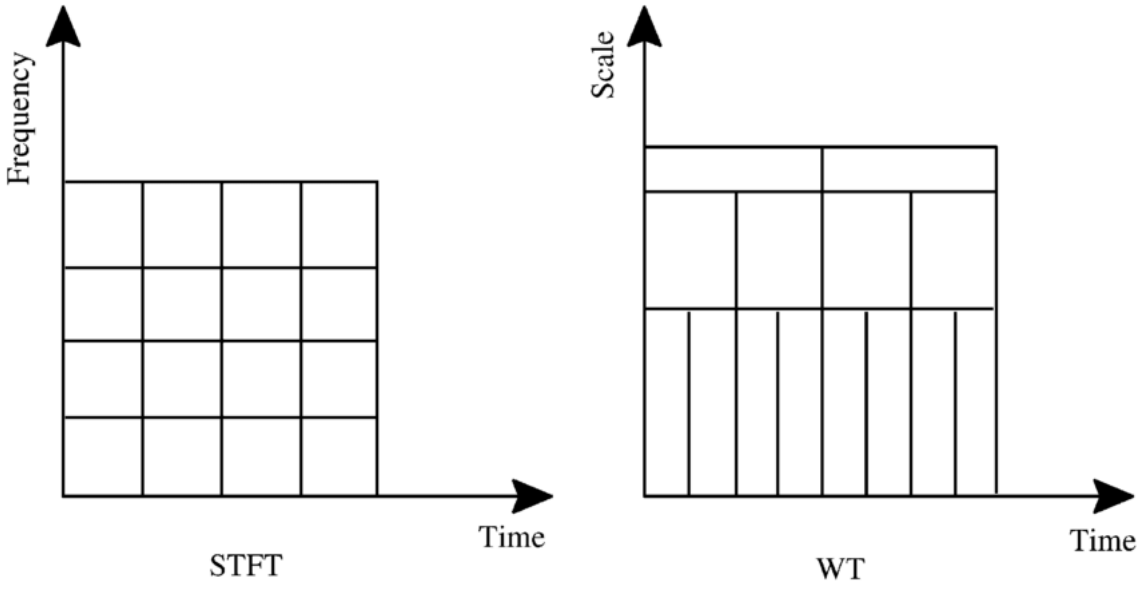

FIGURE 3.2: Comparison of resolution between STFT and WT

During this decade, many research papers have applied wavelet transform to process and analyse ECG signals. In Maheshwari et al. (2013), wavelet transform is used to remove the baseline wandering, artefact and noise of ECG signals. In addition, a low-complexity feature extraction algorithm proposed in Mazomenos et al. (2013) has been implemented to detect features in ECG. Although wavelet transform is a useful tool to analysis ECG signal in both frequency and time domain. It still has the limitation of the banlance between frequency and time resolutions. Recently, some researches proposed some algorithms to solve this problem. For example, Mazomenos et al. (2013) proposed a novel algorithm based on wavelet transform. Moreover, time-domain morphology analysis is implemented to solve the limitation of resolution in the frequency domain. In

this project, we used discrete wavelet transform (DWT) to remove noise and combined with maximum module analysis (MMA) to detect the T-peaks of ECG.

3.2.1.2 Discrete Wavelet Transform

A discrete wavelet transform (DWT) is any wavelet transform for which the wavelets are discretely sampled. As with other wavelet transforms, a key advantage it has over Fourier transforms is temporal resolution: it captures both frequency and time information. Moreover, it can reduce the computational cost due to the discrete set of the mother wavelet. For the DWT, one needs at least the condition that the wavelet series is a representation of the identity in the space $L^(2)(\mathrm{R})$. As mentioned in the above section, the DWT decomposition is implemented as high and low pass filters, which can obtain the detail (D_x) and approximation (A_x) coefficients in the 2^x scale. The level 3 DWT decomposition is shown in Figure 3.3. The low pass filter removes all the frequency components of the above half of the maximum frequency of the input signal, on the other hand, the high pass removes the components below half the maximum frequency. However, since half of the frequencies of the input signal have been removed, half the samples can be discarded according to the Nyquist's rule. Down sampling is performed after filtering in order to remove half of the samples. The output of low pass filter will be considered as the input for next level processing. The process is repeated until the desired level of decomposition of the signal is reached. The frequency resolution increases in higher resolution scales, thus low frequency components are more easily detectable in high resolution scales. On the contrary, high frequency components are expected to be more distinguishable in the lower resolution scales.

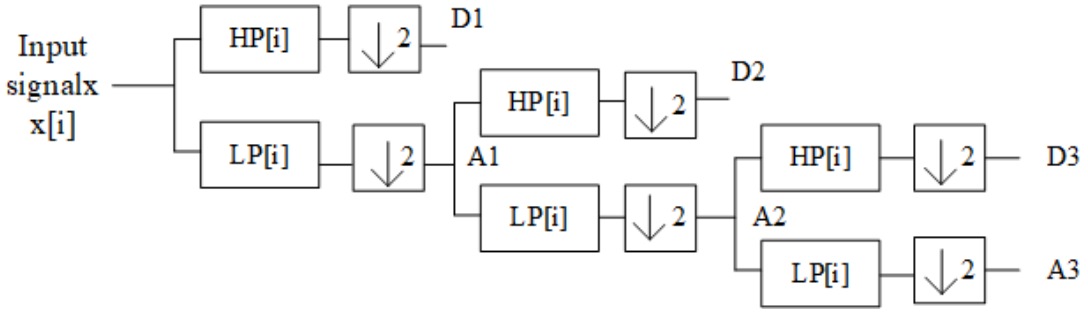

FIGURE 3.3: A level 3 DWT decomposition

From there we can see LP and HP stand for low-pass and high pass filters respectively. At each decomposition level n, detail DWT coefficient D_n and approximation coefficient A_n are produced after filtering and down sampling, which can be given in (3.2).

$$
\begin{aligned}
D_n[i] &= \sum_{k=-\infty}^{\infty} D_{n-1}[i] \cdot HP[2i-k] \\
A_n[i] &= \sum_{k=-\infty}^{\infty} A_{n-1}[i] \cdot LP[2i-k]
\end{aligned}
\tag{3.2}
$$

As mentioned above, frequency in each scale can be divided into two bands with the same bandwidth by using high pass filter and low pass filter. The frequency resolution increases in higher resolution scales Mazomenos et al. (2013), thus low frequency components in ECG, such as P and T waves are more easily detectable in higher resolution scales. In this work, the detail coefficients (D4) in 2^4 scale and (D5) in 2^5 scale are used to detect T wave. Here, the choosing of resolution scale depends on the sampling frequency of the ECG signal. With the increasing sampling frequency of ECG signal, the resolution scale also need to be increased. Once wavelet coefficients are computed, modulus-maxima analysis (MMA) will be applied in order to detect the peaks of T wave. According to the 2^4 and 2^5 resolution scale detailed coefficients in T wave boundaries, the positive values with following negative values of coefficients represents that T peak is the minimum (convex) point in original ECG data, whereas the T peak is the maximum (concave) point if the coefficients are first negative and then become positive.

3.2.2 Clustering Algorithm

3.2.2.1 Introduction

Cluster analysis or clustering is the task of grouping a set of objects in such a way that objects in the same group are more similar to each other than to those in other groups. Recently, many papers have published machine learning algorithm based on clustering to detect arrhythmias. For example Haldar et al. (2017) proposed a machine learning algorithm based on FuzzyC-Means clustering to classify arrhythmias. In cluster analysis, data is partitioned into groups based on some measures of similarity or shared characteristic. Clusters are formed so that objects in the same cluster are very similar and objects in different clusters are very distinct. In machine learning, clustering algorithms can fall into two broad groups. First type is hard clustering, where each data point belongs to only one cluster. Another called soft clustering, where each data point can belong to more than one cluster. In the following section, we represent the brief introduction of two common hard clustering algorithms and one soft clustering algorithm.

- K-Means: As one of most common clustering algorithm, K-Means algorithm partitions data into K number of mutually exclusive clusters. How well a point fits into a cluster is determined by the distance from that point to the cluster's center.

Normally, K-Means algorithm is applied when the number of clusters is known. In addition, It is wildly used for fast clustering of large data sets.

- Hierarchical clustering: It produces nested sets of clusters by analyzing similarities between pairs of points and grouping objects into a binary hierarchical tree. If we do not yet know how the data might be grouped, hierarchical clustering will be the best choice to look for possible structures in the data.
- FuzzyC-Means: It is the most common soft clustering algorithm, as a partition-based clustering where data points may belong to more than one cluster. In general, FuzzyC-Means is used for pattern recognition when the number of clusters is known.

3.2.2.2 Hierarchical Clustering

Hierarchical clustering is a common machine learning algorithm that seeks to determine the hierarchy of all clusters by analyzing similarity or dissimilarity between pairs of points. During recently 15 years, many researchers applied hierarchical clustering method to their projects. For example, Bandyopadhyay and Coyle (2003) proposed an energy efficient hierarchical clustering algorithm to determine the characteristics of the environment. Another research Heard et al. (2006) represented using Bayesian hierarchical clustering to report a statistical analysis of gene expression. Normally, the process of hierarchical clustering is divided into three steps which are (1) choose the hierarchical method, (2) select a measure of similarity or dissimilarity and (3) select a clustering algorithm respectively Sarstedt et al. (2014).

Hierarchical Methods The hierarchical method can be divided into two types. The schematic diagram is shown in Fig.3.4. First is Agglomerative clustering. In this category, each object represents a single cluster at the beginning. These individual clusters will be combined based on their similarity step by step. As shown above, in this case, the two most similar clusters B and C are merged into a new cluster. Then, it will combine with another cluster to generate a new cluster and so on. On the contrary, in divisive clustering, all objects are combined into one cluster initially. Then these objects sequentially spilt up according to their dissimilarity. Moreover, hierarchical clustering does not require the known number of clusters. Therefore, we can obtain the results based on different cluster numbers.

Select a measure of similarity or dissimilarity Determine a measure of similarity and dissimilarity is a very important step because different measures may produce different results. Normally, this step is achieved by calculating the distance between pairs

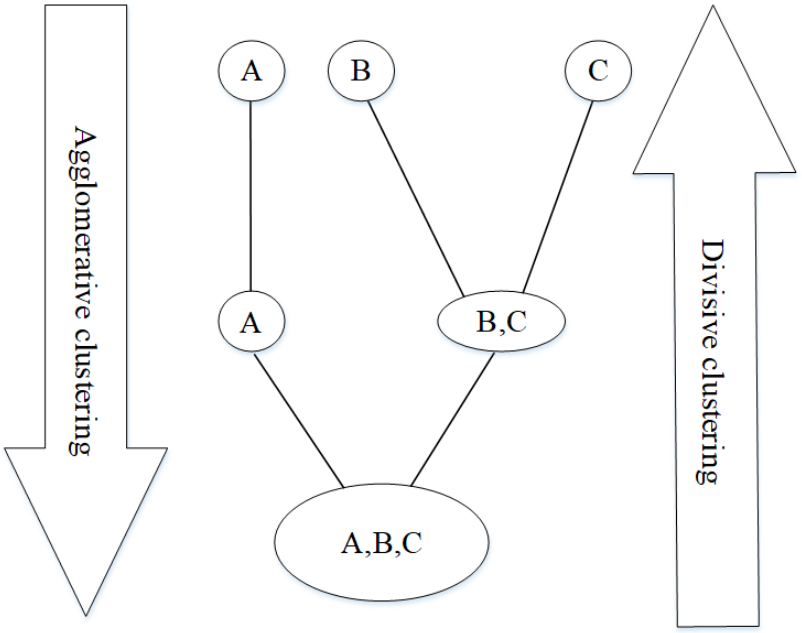

FIGURE 3.4: The flow chart of agglomerative clustering and divisive clustering

of points. There are three different measures of distance shown in Fig.3.5. Euclidean distance is considered as the direct distance between two objects. City-block distance is represented by the difference of abscissa plus difference of ordinate between two objects. Chebychev distance is defined as the maximum value between the difference of abscissa and the difference of ordinate between two objects. If we consider two objects A and B with their corresponding positions (X_a, Y_a) and (X_b, Y_b),the formulas of Euclidean distance, City-block distance and Chebychev distance measures are (3.3), (3.4) and (3.5) respectively.

$$D_{Euclidean} = \sqrt{(X_b - X_a)^2 + (Y_b - Y_a)^2} \tag{3.3}$$

$$D_{City-block} = |(X_b - X_a) + (Y_b - Y_a)| \tag{3.4}$$

$$D_{Chebychev} = max(|X_b - X_a|, |Y_b - Y_a|) \tag{3.5}$$

Select a clustering algorithm After choosing the measure of similarity or dissimilarity, the next step is to determine which clustering algorithm will be applied. Actually, there are several linkage algorithms which can be distinguished by the distance measures between two clusters. The most popular agglomerative clustering algorithms are single linkage algorithm, complete linkage algorithm and average linkage algorithm. These three agglomerative clustering procedures are shown in Fig.3.6. Single linkage and complete linkage determine the distance between two clusters based on the shortest and

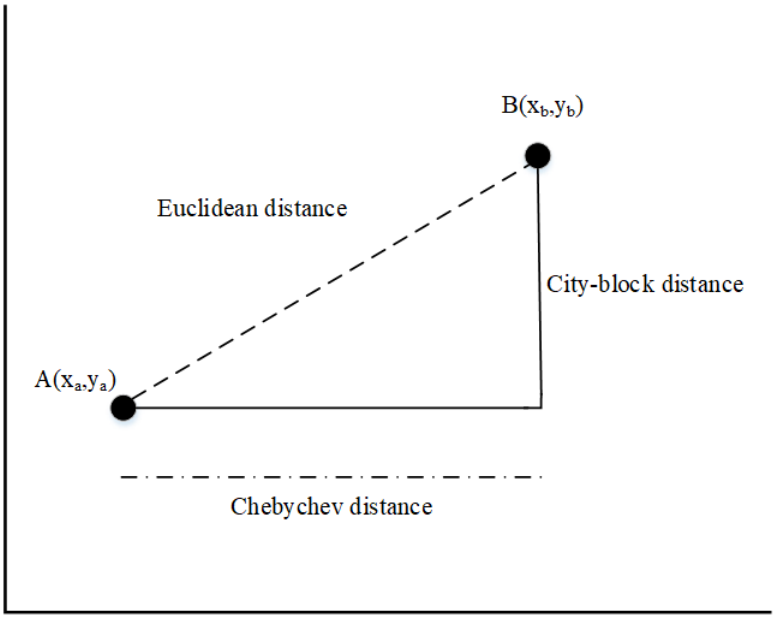

FIGURE 3.5: Three different measurements of similarity or dissimilarity

longest path between any two points in these two clusters respectively. However, because the single and complete linkage algorithms are associated with the shortest and longest distance, it may cause one cluster containing a large number of objects and some other small clusters. Average linkage algorithm is used in order to avoid this situation. Average linkage algorithm can produce clusters with similar sizes based on the average distance between all pairs of points in two clusters.

In addition, the descriptions of three linkage algorithms are shown in (3.6), (3.7) and (3.8) respectively. The cluster r and s are comprise of the previous clusters, n_r and n_s are the number of objects in cluster r and s respectively. x_{ri} and x_{sj} are the i^{th} and j^{th} object in cluster r and s respectively.

$$Linkage_{single}(r,s) = min(D(x_{ri}, x_{sj})), i \in (1, \cdots, n_r), j \in (1, \cdots, n_s) \tag{3.6}$$

$$Linkage_{complete}(r,s) = max(D(x_{ri}, x_{sj})), i \in (1, \cdots, n_r), j \in (1, \cdots, n_s) \tag{3.7}$$

$$Linkage_{average}(r,s) = \frac{1}{n_r n_s} \sum_{i=1}^{n_r} \sum_{j=1}^{n_s} D(x_{ri}, x_{sj}) \tag{3.8}$$

3.3 Methodology

The strategy of the first step is to identify the R peak positions by using clustering algorithm. If we can determine the R-wave clusters and non R-wave clusters, it is

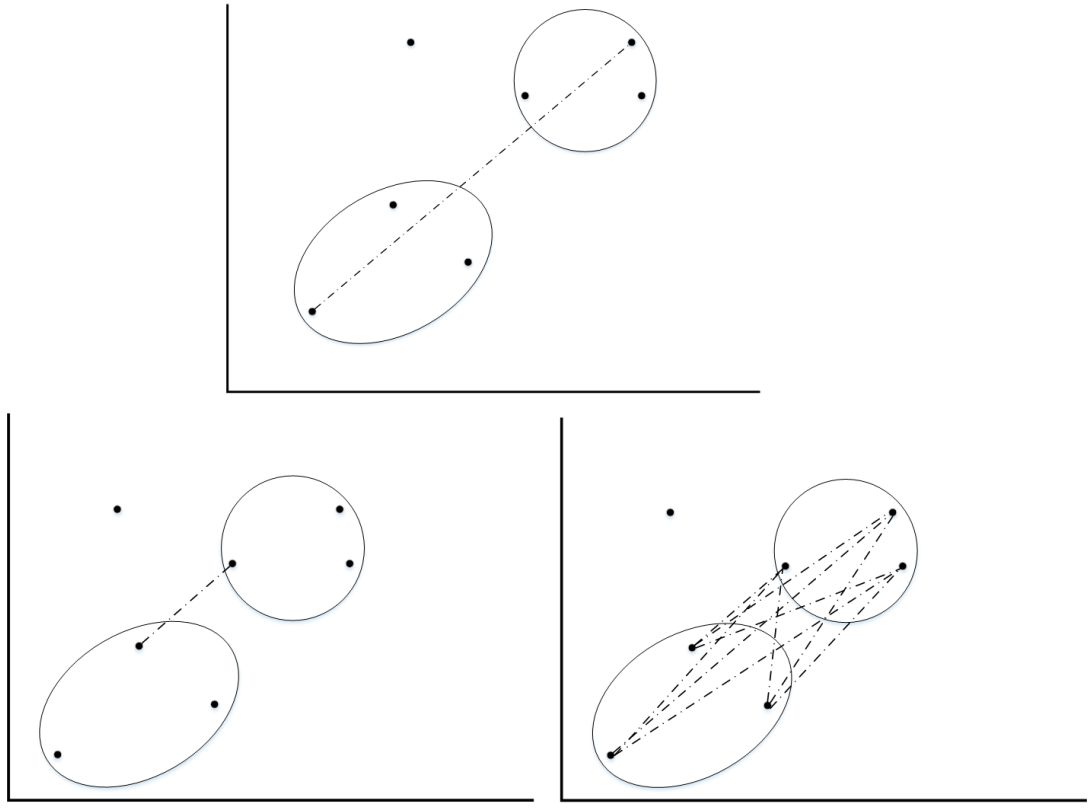

FIGURE 3.6: The agglomerative clustering algorithms based on complete linkage (top), single linkage (left bottom) and average linkage (right bottom)

possible to find the R peaks in R-wave clusters. There are many unsupervised machine learning algorithm may help us determine the R-wave clusters. Among these algorithms, most of them such as K-Means, K-Medoids and Fuzzyc-Means, can only be applied when we know the number of clusters Boutros and Okey (2005). It is difficult to know the number of R-wave clusters because different situations may lead to many different R-wave clusters. For example, wide QRS complexes, abrupt changes of R-R intervals, low-amplitude R peaks and high-amplitude T peaks et al. In this case, the advantage of hierarchical clustering is highlighted, it assumes the data are hierarchical and hence does not require the known number of clusters.

In this section, we will present the proposed method based on the combination of hierarchical clustering and discrete wavelet transform. our algorithm aims at detection of QRS complexes and T peaks from the sequence of successive ECG signals. In this work, in order to analyse at least one R-peak and at most two R-peaks each step. We set a sliding $1.2s$ time window for each step, as we experimentally found out the optimal time window for detecting the R-peaks. Our proposed technique is structured as a four-stage process. First is ECG pre-processing. Raw ECG signals were filtered using Butterworth high-pass filter and low-pass filter with the corresponding cut-off frequency of 1 Hz and 30 Hz to remove the noise and baseline wandering Amann et al. (2005). After that, the ECG signal was normalized using the (3.9) such as all the values will be in the

range [0,1]. An example can be seen in Fig.3.7. The second stage is using hierarchical clustering to determine the R clusters and non-R clusters, then, identify the R-peaks from R-clusters. The third stage pertains to the T-wave boundary detection based on the R peak and the ECG period template. The final stage is to find the T peaks by using discrete wavelet transform and modulus-maxima analysis.

$$\widetilde{E}(n) = (E(n) - E_{min}) / (E_{max} - E_{min}) \tag{3.9}$$

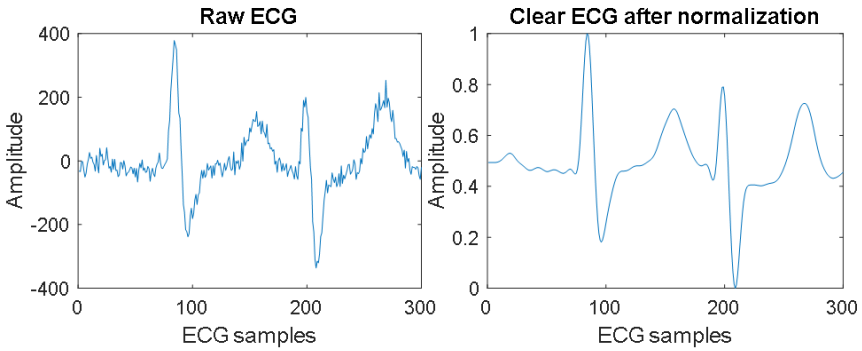

FIGURE 3.7: An example of ECG pre-processing(annotation:se1891m from QT database. The sampling frequency is $250Hz$ hence a time window has 300 ECG samples)

3.3.1 Detection of R peaks

The strategy of the proposed algorithm is to first identify the R-peak position by using hierarchical clustering. In this stage, we use agglomerative cluster method because we consider every ECG sample as an individual cluster initially and all R wave samples are merged into a cluster based on their similarity. The second step is to choose a measurement of similarity. We select Euclidean distance to measure the similarity between each ECG sample because the Euclidean distance is widely used measurement for two-dimensional data in a mathematical field. Finally, we need to select a clustering method to determine the R-wave clusters. In this case, single and complete linkage algorithms are not applicable because these two algorithms reduce the assessment of the cluster quality to a single similarity between a pair of objects. These two algorithms based on a pair of objects cannot fully reflect the distribution of objects in one cluster. Therefore, they usually produce an undesirable cluster that may include non-R samples. The average linkage algorithm can avoid this situation because it determines the clusters based on the average distance between all pairs of objects. The process of our R-peak detector can be divided into three main stages, namely cluster extraction, R-peak estimation and real R-peak identification. The block diagram of the proposed R-peak detector is drawn in Fig. 3.8.

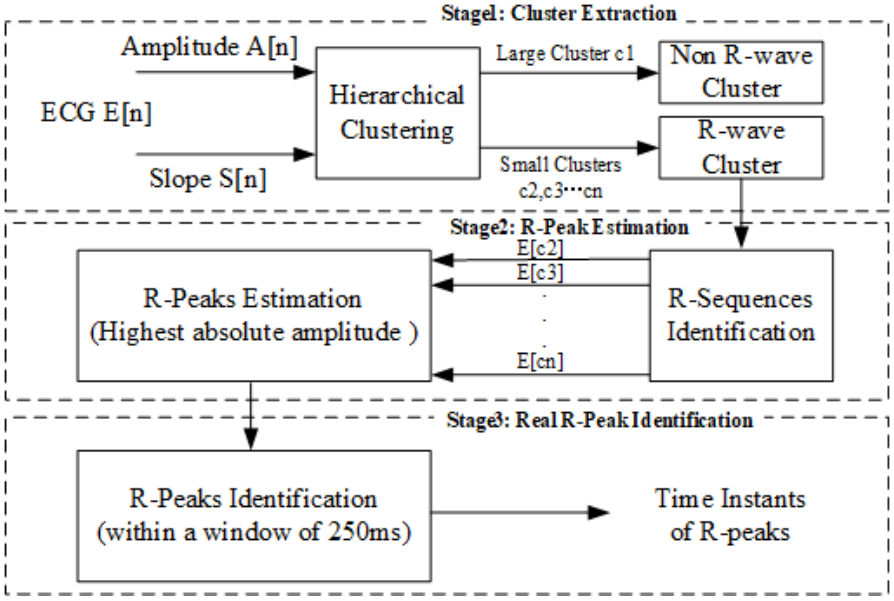

FIGURE 3.8: Flowchart of the proposed R-peak detector

First, for ECG data $E[n]$, each ECG sample $E[i]$ is considered as a individual object with its amplitude $A[i]$ and slope $S[i]$. The slope of an object is defined as the average absolute value of the amplitude difference between $E[i]$ and $E[i+1]$; and $E[i-1]$ respectively. The expression is shown in (3.10). Then, these objects are considered as the input data to a two-dimensional hierarchical clustering system. The ECG samples are displayed in a two-dimensional coordinate system, with x axis and y axis are the amplitude and slope of each ECG sample respectively as seen on the left of the Fig.3.9. Then, the hierarchical clustering system will calculate the distance between each object (ECG sample) using (3.3). Initially, two ECG samples with the shortest distance are merged into a cluster. Then the hierarchical clustering system selects two clusters with the shortest average distance of the ECG samples between them by (3.8), groups them together into a new cluster and repeats the procedure with the remaining ECG samples. Until the number of cluster become 2, one is a large cluster and another is a small cluster. The cluster with small number of object is R-cluster, since the ECG samples of R-wave is just a small part of the ECG signal. It is shown on the right of the Fig.3.9, the objects (ECG samples) with relatively larger slope and amplitude are merged into a small cluster, which can be considered as the R-cluster. Other ECG samples are non-R cluster. Here, some of the ECG samples with large amplitude are still considered as non-R cluster, that is because the slope of these objects are relatively low. This is particularly important to solve T-wave oversensing. Even the amplitude of a T-wave is higher than a R-wave, the slope of the T-wave is relatively low. Then the ECG samples of this T-wave will still be grouped into the non-R cluster.

$$S[i] = \begin{cases} |A[i+1] - A[i]| & i = 1, \\ (|A[i+1] - A[i]| + |A[i] - A[i-1]|)/2 & 1 < i < n, \\ |A[i] - A[i-1]| & i = n. \end{cases} \tag{3.10}$$

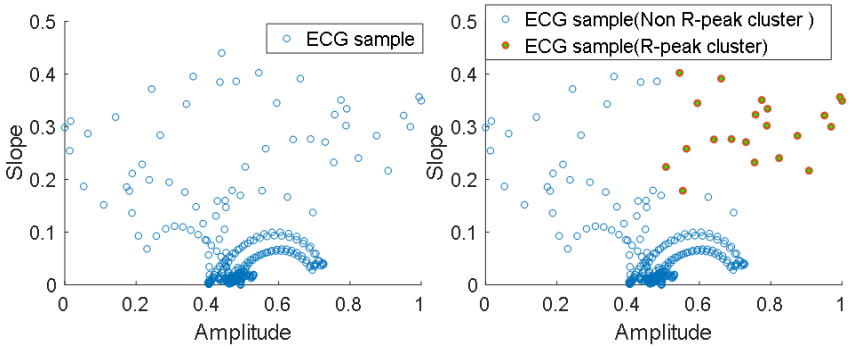

FIGURE 3.9: An example of ECG R-wave cluster extraction based on Fig.3.7

Once the R-wave clusters are determined in the last stage, the next step is to identify the R-wave ECG sample sequences from these R-wave clusters. As shown on the left of the Fig.3.10. There are two R-wave sequences (Green points) from the R-peak cluster which are identified using hierarchical clustering. Then, this step is to find the ECG sample with highest absolute value of the amplitude within each R-wave sequences and consider these ECG samples are R-peaks. The final result is shown on the right of the Fig.3.10.

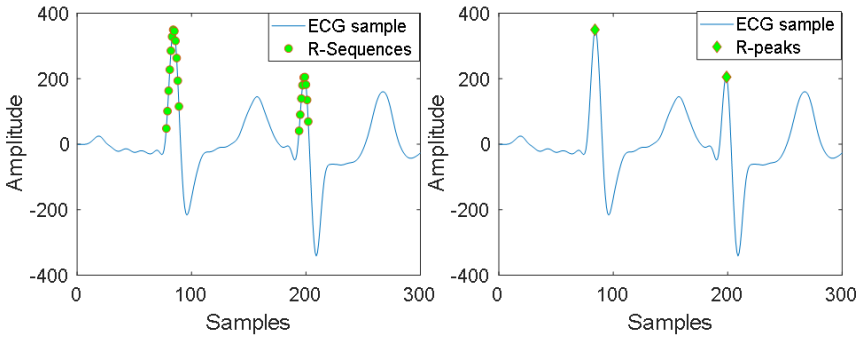

FIGURE 3.10: An example of R-peak Estimation based on Fig.3.9.

However, there is an abnormal situation that was introduced in Maheshwari et al. (2013) named RsR' pattern. There is an additional spike of QRS complexes caused by any abnormality of conduction in bundle branch block, which is referred to as R'. In addition, as we mentioned earlier, a sliding 1.2 s time window was applied for R-peak detection. In this case, if two successive windows contain half of a same ECG beat, our algorithm will detect two R-peaks that actually are in the same QRS complex. Therefore, a post-processing is needed to remove such R' peaks from RsR' pattern or a fake R-peak due to a half ECG beat in a window. We set a threshold of the shortest period between each R

peak from two successive QRS complexes, which is from 100 ms Manikandan and Soman (2012) to 250 ms Cesari et al. (2017). The experimental results showed that 100 ms window is too small if there is a RsR' pattern in a wide QRS complex and 250 ms is too large to a small QRS complex. From the results, 200 ms time window is an acceptable time window to identify the R-peaks. In this case, if two R peaks are identified in a window of 200 ms, the one with the lower amplitude is removed and another one is kept as a real R peak.

3.3.2 Determination of the T wave boundary

In this stage, we have the template of a single PQRST period with its corresponding QRS onset, offset and R-peak, which are annotated by cardiologists Goldberger et al. (2000). The template is randomly defined as one well-behaved PQRST period from the healthy part of each ECG record from MIT-BIH and QT databases. For UHS database, a template file showing one stable intrinsic rhythm created by an Electrophysiologist, who also visually identified the R and T wave components in each signal. Fig.3.11 is an example of a template with the determined QRS complex. The green diamond is marked as R-peak (t_0). Moreover, the PQRST-onset (offset) and QRS-onset (offset) are t_1 (t_2) and t_3 (t_4) respectively. In this case, [t_4,t_2] is considered as T wave boundary of the template. Then we calculated the distance between R-peak and QRS offset, PQRST offset as $t_4 - t_0$ and $t_2 - t_0$ respectively. Once we obtained the R-peak (t_R), the QRS offset(T onset) and PQRST offset (T offset) is initially estimated as $t_{Ton} = t_R + (t_4 - t_0)$ and $t_{Toff} = t_R + (t_2 - t_0)$ respectively. It can be seen in Fig.3.12, the red points are QRS offset (T onset) and yellow points are PQRST offset (T offset). The next step is to calculate the Mean Square Error (MSE) between ECG samples (E_i) in the T wave boundary of the template and ECG samples ($\tilde{E}_i$) in each estimated T wave boundary using (3.11). Where n is the number of ECG samples in T wave boundary. Finally is to move each estimated T wave boundary forward and backward for 20 samples $\tilde{E}_{i\pm20}$ and calculate the respective MSE. The final T wave boundaries are extracted based on the minimum MSE between E_i and $\tilde{E}_{i\pm20}$. It is also need to noted that our obtained T wave boundaries may not be the actual T wave boundaries, since once the width of ECG beat become abnormal, such T wave boundaries can not be identified accurately using a normal template. Therefore, the main idea of our algorithm is to determine the approximate range based on the T boundary to make sure the T-peak is in this range.

$$MSE = \frac{1}{n}\sum_{i=1}^{n}(E_i - \tilde{E}_i)^2 \tag{3.11}$$

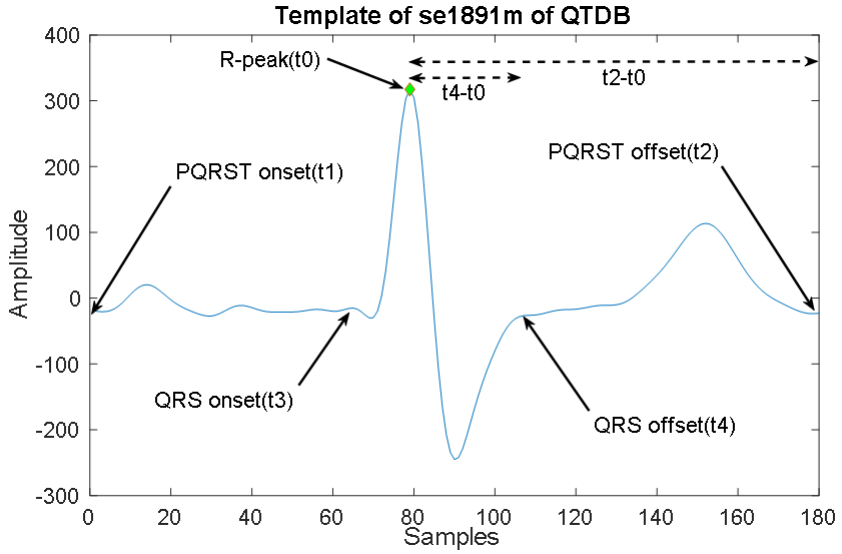

FIGURE 3.11: The template of the single PQRST period (annotation:se1891m from QT database)

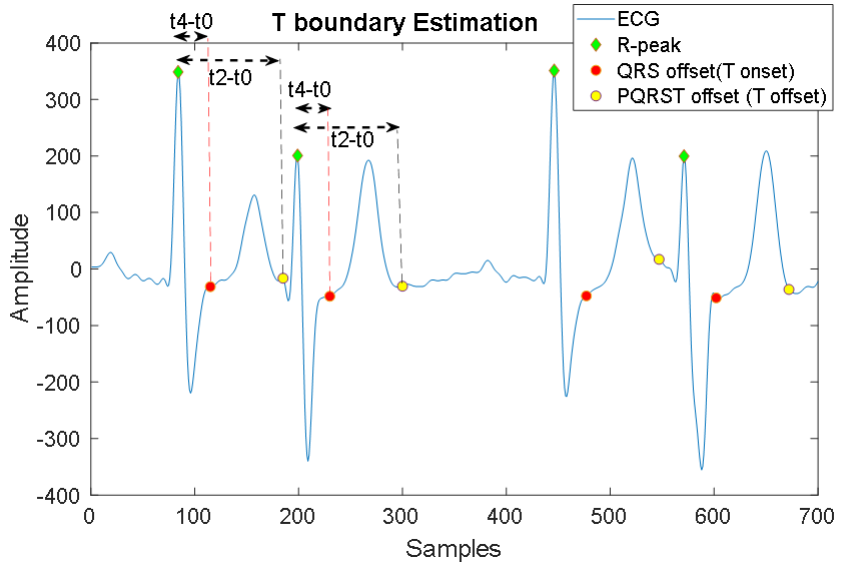

FIGURE 3.12: T wave boundary estimation using template (Fig.3.11) (annotation:se1891m from QT database)

3.3.3 Detection of T peaks

Once the approximate T wave boundaries are finalized. The discrete wavelet transform (DWT) is applied to combine with the modulus-maxima analysis (MMA) method to determine the T-peaks. We developed an algorithm that takes inspiration from the work of Martínez et al. (2004) and Mazomenos et al. (2013). Since the T waves have significant components at higher scale, it is possible to detect T-peaks at scale 2^4 or 2^5 using DWT Martínez et al. (2004). We also select 'Haar' as the wavelet function in order to reduce the computational complexity, because it is the simplest wavelet function and it is sufficient for T-peak detection Mazomenos et al. (2013). In this work, the 2^4

and 2^5 resolution scale detailed coefficients are first determined after using DWT. Once wavelet coefficients are computed, the next step is using MMA to find the positions of T peaks. Given the positive or negative deflection of the T wave, compared to the baseline, the pair of extrema that indicates the wave's temporal position can be either a wavelet coefficient with minimum value followed by a maximum wavelet coefficient, for positive deflection or the reverse for a negative deflection. Through MMA, we initially obtain the temporal position by calculating the temporal positions t_1, t_2 with the maximum or minimum values in the D4 coefficients and t_3, t_4 in the D5 coefficients as discussed in section 3.2.1.2. This deflection should correspond to the T peaks. As mentioned before, half of the samples are discarded at each level after filtering in DWT. Therefore, it is noted that the temporal resolutions on the 2^4 and 2^5 are diminished (by a factor of 16 and 32 respectively) compared to the original time scale. Thus, the T peak time point is calculated as the maximum or minimum of the data within time widows $[t_1 \times 2^4, t_2 \times 2^4]$ and $[t_3 \times 2^5, t_4 \times 2^5]$. If the deflection detected in the MMA is characterized as negative, then T wave is inverted. The final step is to compare the absolute values of T peak amplitudes, which are obtained from the last step. The one with the highest absolute value of the amplitude is kept as the T peak. A detailed example is shown in Fig.3.13. Once the T wave boundaries are determined, the DWT is applied to calculate the D4 and D5 coefficients of the T wave. From the D4 coefficients, the t_1 and t_2 are 3 and 5 respectively, the T peak time point is then calculated as the maximum value within the time window $[3 \times 2^4, 5 \times 2^4]$. In this case, the T peak time point is identified at 58. On the other side, the T peak time point based on the D5 coefficients within the time window $[2 \times 2^5, 3 \times 2^5]$ is calculated at 64. Finally, the T peak with the highest absolute value of amplitudes is kept, in this case, the real T peak is determined at 58 with amplitude 46.5 rather than another T peak with lower amplitude 38.1.

Although it is noted that the T waves have different morphology, such as peaked T waves, inverted T waves, biphasic T waves, T waves with two peaks et al.Burns (2019). The main aim of our system is to identify the T-peak with the largest absolute value of the amplitude as the real T-peaks in each window. The Fig.3.14 is the final result of our algorithm for an example record (se1891) with T wave oversensing problem from QT database. The green diamonds and the red squares are R-peaks and T-peaks respectively. The implementation of the algorithm for validation took place in MATLAB R2018a.

3.4 Results and Discussion

3.4.1 Data and Validation

The MIT-BIH, QT databases Goldberger et al. (2000) and 15 records from University Hospital Southampton (UHS) are used to validate our proposed algorithm. First we used all 48 30-minutes ECG records with 360Hz sampling frequency of MIT-BIH

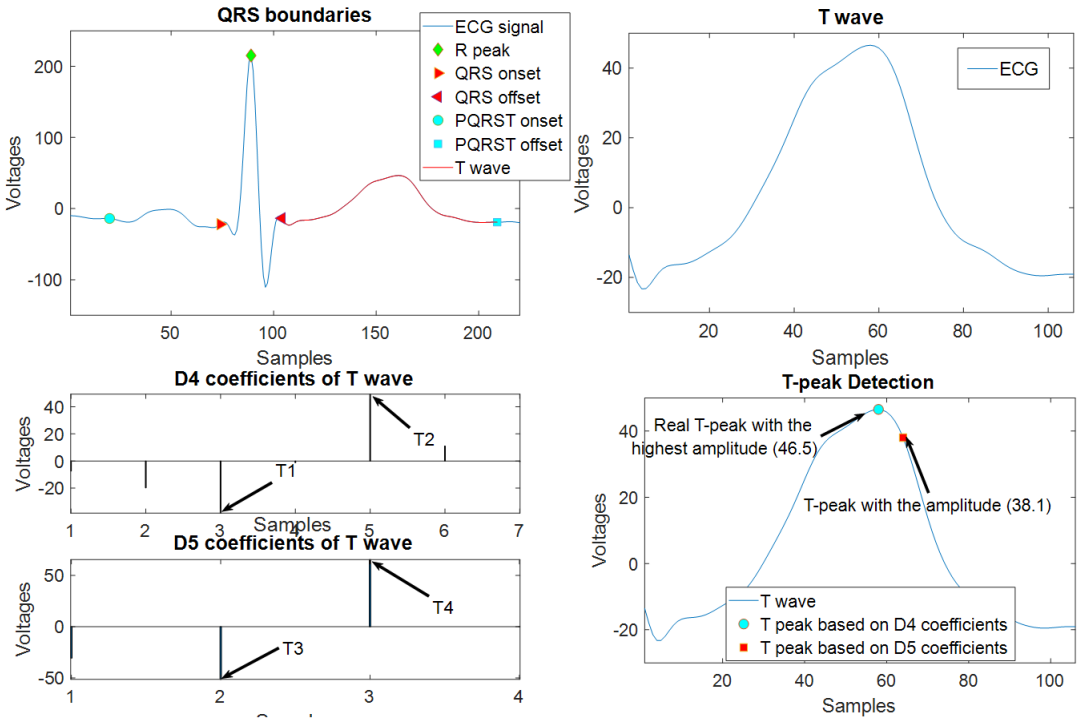

FIGURE 3.13: T peak detection based on DWT and MMA

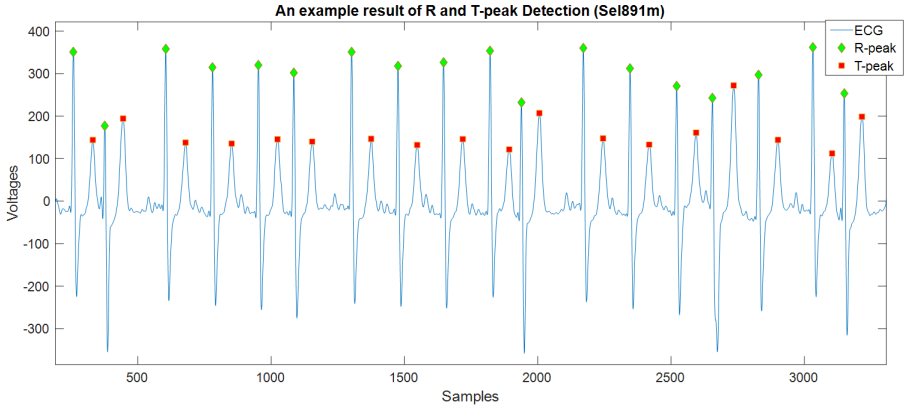

FIGURE 3.14: The result of an example with T wave oversensing for R and T peak Detection.(annotation:sel891m)

databse. In this work, we calculated sensitivity $Se = TP/(TP + FN)$, positive predictivity $+P = TP/(TP + FP)$ and Accuracy $Acc = TP/(TP + FP + FN)$ of the annotated R wave peaks, where TP is the true positives (peak is detected of the annotated peak), FN denotes the false negatives (annotated peak is not detected) and FP is the false positives (when peak is detected outside the range of the annotated peak). In this work, we calculated sensitivity Se and positive predictivity $+P$ by considering the range of 150ms ($\pm$75ms) of the annotated R-peaks in order to compare with the literature under the same condition Saadi et al. (2015)Cesari et al. (2017)Ghaffari et al. (2009)Friganovic et al. (2018). We compared the performance of our algorithm with other formally established algorithm for R-peak detection, which is shown in Table 3.1.

Moreover, Table 3.2 represents the effectiveness of our R-peak detector in terms of false positives.

For the QT database, it has 105 2-lead recordings with a sampling frequency of 250Hz. It includes different T wave morphologies, such as normal, inverted, only upwards and only downwards deflections Laguna et al. (1997). It was also manually annotated by two cardiologists with annotated R-peaks and T-peaks for 3623 beats and 3542 beats respectively in 103 records. These records have different situations that include supraventricular arrhythmias, normal sinus rhythm, ST change, long-term ECG signals and sudden death. In this work, all ECG records (more than 111200 beats) of the automatically annotated QT database is used to evaluate our algorithm. Moreover, the 103 manual annotated records of Lead I are also used since they are more salient. The results are finally compared with other methods.

We also evaluated the detection accuracy of our algorithm based on the time difference (error) between the detected peaks and the manual annotated peaks. The accuracy in terms of the average of the errors (m) and the standard deviation (s) of the errors are obtained for entire records. The results and the comparison with the literature are given in Table 3.3. Finally, we built a record-by-record classification as proposed in Martínez et al. (2004) and more recently in Cesari et al. (2017) for T peak detection. We chose the same threshold in Martínez et al. (2004) to compare with the previous works. The thresholds are measured by the 15ms for the absolute average error ($bias$) and 30.6ms for the standard deviation (s). Thus, these records are divided into four groups based on the following rule: Group I: $bias < 15ms$ and $s < 30.6ms$; Group II: $bias > 15ms$ and $s < 30.6ms$; Group III: $bias < 15ms$ and $s > 30.6ms$ and Group IV: $bias > 15ms$ and $s > 30.6ms$. The comparison results with three formally established algorithms for the T peak detection are shown in Table 3.4.

In addition, the 15 ECG records from UHS are 1 minute in duration and the sampling frequency is 1000 samples per second. We also calculated the sensitivity and positive predictivity for these 15 ECG records. And the performances for R-peak and T-peak detection based on the UHS database are shown in Table 3.5 and Table 3.6 respectively.

3.4.2 Method Evaluation

The proposed algorithm shows the high performance in the delineation of ECG R and T-peaks. Concerning the R peak detection, the Table 3.1 shows that the performance of our proposed algorithm for R-peak detection in MIT-BIH database is generally better or comparable with other formally established methods. Our method achieves 99.89% Se, 99.94% $+P$ and 99.83% Acc for R-peak detection, the performance in terms of $+P$ and

TABLE 3.1: The R-peak (QRS) detection performance comparison in the MIT-BIH Arrhythmia database.(The window used for defining a true positive is reported as w, N/R: Not Reported)

Authors	Method Used	w[ms]	TP	FP	FN	Se[%]	+P[%]	Acc[%]
This work	**Hierarchical clustering**	**150**	**109370**	**63**	**124**	**99.89**	**99.94**	**99.83**
Martínez et al. (2004)	Wavelet transform(WT)	N/R	109208	153	220	99.80	99.86	99.66
Ghaffari et al. (2009)	Discrete wavelet transform(DWT)	150	109327	129	101	99.91	99.88	99.79
Manikandan and Soman (2012)	Shannon energy envelope(SEE)	N/R	109356	140	79	99.93	99.86	99.79
Elgendi (2013)	Moving average filters	N/R	N/R	N/R	N/R	99.78	99.87	N/R
Merah et al. (2015)	Stationary wavelet transform(SWT)	100	109316	126	178	99.84	99.88	99.72
Saadi et al. (2015)	Optimized adaptive thresholding	150	N/R	N/R	N/R	99.90	99.87	N/R
Thiamchoo and Phukpattaranont (2016)	Continuous wavelet transform(CWT)	N/R	109135	356	185	99.69	99.83	99.52
Thungtong (2017)	Discrete wavelet transform(DWT)	N/R	109096	242	409	99.63	99.78	99.41
Smaoui et al. (2017)	Continuous wavelet transform(CWT)	N/R	N/R	168	756	99.37	99.83	N/R
Cesari et al. (2017)	Wavelet transform (WT)	150	109321	147	173	99.84	99.87	99.71
Friganovic et al. (2018)	Mathematical morphological filter	150	98659	268	214	99.78	99.72	99.52
Zalabarria et al. (2020)	Iterative state machines	N/R	106096	431	485	99.54	99.60	N/R

TABLE 3.2: Comparison of the numbers of false-positives (FPs) based on R-peak detection for specific records of the MIT-BIH arrythmia database, (where **N/A** is Noise and Artefact, **BD** is Baseline Drifts, **IR** is Irregular Rhythmic, **VA** is Ventricular Arrhythmias, **SCR** is sudden changes in R-peak, **HT** and **HP** are high T-peak and P-peak respectively, **PVCs** is Premature Ventricular Contractions and **sQRS** is small QRS complexes.)

No.	Characteristics	Number of false-positive (FP) detection						
		Manikandan and Soman (2012)	Merah et al. (2015)	Thiamchoo and Phukpattaranont (2016)	Thungtong (2017)	Smaoui et al. (2017)	Zalabarria et al. (2020)	This work
104	N/A	14	12	15	7	32	3	**0**
105	N/A	18	11	22	48	25	9	**0**
108	N/A, BD, HP	12	10	12	40	19	73	**5**
113	HT	3	4	8	4	0	0	**0**
116	BD, sQRS	8	7	2	26	2	1	**10**
200	N/A, VA	6	0	16	6	7	0	**0**
203	N/A, BD, IR, VA	5	10	14	53	24	24	**10**
208	BD, PVCs, sQRS	5	3	4	22	4	4	**7**
210	N/A, BD	3	3	3	16	4	1	**7**
222	BD, IR, HP	0	5	1	4	1	0	**4**
223	SCR	0	0	1	8	0	0	**0**
228	N/A, BD	7	7	19	5	19	9	**7**
232	BD	18	10	4	2	2	12	**4**
233	VA	0	0	0	13	0	0	**0**
Total		99	82	121	254	139	136	**54**

TABLE 3.3: R-peak (QRS) and T-Peak Detection Performance comparison in the QT database.(The window used for defining a true positive is reported as w, N/R: Not Reported)

	Authors	Method Used	Annotation(File Name)	w[ms]	TP	FP	FN	Se[%]	+P[%]	Acc[%]
R-peak (QRS)	**This work**	**Hierarchical clustering**	**Manual(.qlc)**	**150**	**3617**	**6**	**0**	**100**	**99.83**	**99.83**
	Martínez et al. (2010)	Phasor transform	Manual(.qlc)	N/R	N/R	N/R	N/R	99.85	N/R	N/R
	Cesari et al. (2017)	WT	Manual(.qlc)	150	N/R	N/R	N/R	100	N/R	N/R
	This work	**Hierarchical clustering**	**Automatic(.pu)**	**150**	**111153**	**47**	**91**	**99.92**	**99.96**	**99.88**
	Martínez et al. (2004)	WT	Automatic(.pu)	N/R	86824	107	68	99.92	99.88	99.80
	Ghaffari et al. (2009)	DWT	Automatic(.pu)	150	86845	79	47	99.94	99.91	99.85
	Elgendi (2013)	Moving average filters	Automatic(.pu)	N/R	110834	N/R	N/R	99.99	99.67	N/R
	Merah et al. (2015)	SWT	Automatic(.pu)	100	86837	99	55	99.94	99.89	99.82
	Thungtong (2017)	DWT	Automatic(.pu)	N/R	83092	80	206	99.75	99.90	99.66
	Friganovic et al. (2018)	Mathematical morphological filter	Automatic(.pu)	150	84849	2161	1508	98.25	97.51	95.76

	Authors	Method Used	Annotation(File Name)	w[ms]	TP	FP	FN	Se[%]	+P[%]	m±s(ms)
T-peak	**This work**	**Hierarchical clustering and DWT**	**Manual(.qlc)**	**150**	**3520**	**22**	**3**	**99.91**	**99.38**	**1.4±8.2**
	Martínez et al. (2004)	WT	Manual(.qlc)	N/R	N/R	N/R	N/R	99.77	97.79	0.2±13.9
	Ghaffari et al. (2009)	DWT	Manual(.qlc)	N/R	N/R	N/R	N/R	99.87	99.80	0.3±4.1
	Martínez et al. (2010)	Phasor transform	Manual(.qlc)	N/R	N/R	N/R	N/R	99.20	N/R	5.3±12.9
	Elgendi et al. (2015)	Moving average filters	Manual(.qlc)	60	N/R	N/R	N/R	98.90	98.77	N/R
	Cesari et al. (2017)	WT	Manual(.qlc)	150	N/R	N/R	N/R	99.50	N/R	-2.6±12.2
	Friganovic et al. (2018)	WT+templates	Manual(.qlc)	160	3115	464	427	87.94	87.03	N/R

TABLE 3.4: QT database stratification according to the T-peak detection.(N/A: Not Available)

QT database	Group I		Group II		Group III		Group IV	
Method	%	m±s[ms]	%	m±s[ms]	%	m±s[ms]	%	m±s[ms]
This work	**95**	**2.86±5.62**	**0**	**N/A**	**2**	**12.07±54.53**	**3**	**33.13±74.02**
Martínez et al. (2004)	83	3.9±7.6	5	-2.7±17	5	-0.5±37	7	-42±72
Cesari et al. (2017)	89	-5.5±7.7	2	8.7±22.5	3	-3.1±55.3	6	38.1±50.5
Vila et al. (2000)	82	4.2±8.6	8	36±15	4	9.6±38	6	32±40

TABLE 3.5: R peaks and QRS complexes detection performance results in ECG from UHS

Record	R/QRS	TP	FN	FP	SE (%)	+P (%)
No.1	90	87	2	3	96.67	97.75
No.2	61	58	0	3	95.08	100
No.3	65	65	0	0	100	100
No.4	59	59	0	0	100	100
No.5	85	84	1	1	98.82	98.82
No.6	72	72	0	0	100	100
No.7	57	57	0	0	100	100
No.8	84	84	0	0	100	100
No.9	77	77	0	0	100	100
No.10	50	50	0	0	100	100
No.11	63	63	0	0	100	100
No.12	70	70	0	0	100	100
No.13	67	67	0	0	100	100
No.14	61	61	0	0	100	100
No.15	61	61	0	0	100	100
Total	**1022**	**1015**	**3**	**7**	**99.32**	**99.71**

Acc is higher than other previously proposed works. The detailed performance of R-peak detection for each MIT-BIH record is shown in the Table 3.7. Besides, from Table 3.2, it can be seen in our work, false positives of R-peak detection can be effectively reduced and only exist in the records with baseline drifts. Furthermore, Table 3.3 shows that for R peak detection, this algorithm achieves 100% Se and 99.83% $+P$ over the manually annotated QT database. It also achieved a Se of 99.92% and a $+P$ of 99.96% over the automatically annotated QT database. Although three studies in literature Ghaffari et al. (2009), Manikandan and Soman (2012) and Saadi et al. (2015) achieved slightly higher Se for R-peak detection, the $+P$ and Acc are lower than our algorithm. Since the number of true positive of our algorithm for R-peak detection is larger than these studies. Overall, the R-peak detection performance of our algorithm is generally better or comparable with the previous work.

In terms of the T-peak detection in manually annotated QT database, our algorithm achieved a Se of 99.91% and a $+P$ of 99.38%. Although we used a 150 ms window

TABLE 3.6: T peaks detection performance results in ECG from UHS

Record	T peaks	TP	FN	FP	SE (%)	+P (%)
No.1	90	87	3	3	96.67	96.67
No.2	61	58	3	3	95.08	95.08
No.3	65	65	0	0	100	100
No.4	59	59	0	0	100	100
No.5	85	84	1	1	98.82	98.82
No.6	72	71	1	1	98.61	98.61
No.7	57	57	0	0	100	100
No.8	84	82	2	2	97.62	97.62
No.9	77	74	3	3	96.1	96.1
No.10	50	47	3	3	94	94
No.11	63	63	0	0	100	100
No.12	70	70	0	0	100	100
No.13	67	67	0	0	100	100
No.14	61	61	0	0	100	100
No.15	61	61	0	0	100	100
Total	**1022**	**1006**	**12**	**16**	**98.43**	**98.82**

to define the true positive of T-peak detection, the mean (m) and standard deviation (s) of errors are lower than most of the previous work. It is also noted that the study in literature Ghaffari et al. (2009) achieved lower mean (m) and standard deviation (s) of errors for T-peak detection. However, they did not annotate the number of the true positives and this may reflect they did not use all manual annotated QT database. Moreover, the QT database stratification based on the T peak detection is given in Table 3.4. It shows that the T peaks in the 95% of the records are able to be detected by using our method, which is higher than other referenced methods. The other 5% records in Group III and IV show the larger mean (m) and standard deviation (s) than other works. This might be the reason for causing large mean (m) and standard deviation (s) of errors over the whole QT database. A deeper analysis shows the records in these two groups are from "sudden death" patients which can be checked in Laguna et al. (1997). Our method may have problems in T peak detection for "sudden death" records because the morphology of T waves in these records may be erratic. Further study is needed to investigate in this type of condition.

For the ECG records from the UHS, the results show that the proposed algorithm can detect R peaks, the corresponding QRS complexes and T peaks successfully in normal ECG. Some R peaks and T peaks are failed detection because of the dramatic change of the ECG data. The sensitivity SE reports the percentage of R wave peaks that were correctly detected by the algorithm. The positive detection +P reports the percentage of R wave peak detection that were true R wave peaks. The algorithm achieved a sensitivity of 99.32% and a positive detection of 99.71%, which can be considered as a very nice performance for detecting R peaks and QRS complexes. The performance

of T-peak detection is slightly worse than the detection of R peaks, the sensitivity and positive detection are 98.43% and 98.82% respectively. The reason of this phenomenon might be the fickle shape of ECG in T wave boundaries. Moreover, these ECG only contain one-minute record, the results might not show the completely performance for ECG peak detection.

3.5 Concluding Remarks

In this chapter, we have proposed a new algorithm based on the hierarchical clustering and discrete wavelet transform for the automated delineation of the ECG fiducial points (R and T peaks). Our algorithm has been validated on the MIT-BIH arrhythmia database, QT database and UHS database. The results show that the performance of algorithm is generally better than other referenced algorithms. The use of hierarchical clustering allows for identifying the R clusters and determining the R peaks with high accuracy of 99.83% based on MIT-BIH database. The combination of DWT and MMA analysis detect the T peaks with high sensitivity of 99.91% based on QT database. Also our algorithm can effectively reduce the TWOS and the number of R-peak false positive detection. However, since the template of each ECG record in MIT-BIH and QT databases was randomly chosen from healthy parts, the performance of our algorithm might be changed with different templates. Therefore, the robustness of our algorithm should be further evaluated with the different healthy templates. In the next chapter, we will develop a PSR-based method and combine with the above hierarchical clustering algorithm to improve the performance for reducing TWOS in S-ICD system.

TABLE 3.7: R-peak detection results of evaluating the proposed algorithm performance on MIT-BIH arrhythmia database

MIT-BIH	TP	FP	FN	SE(%)	+P(%)	Acc(%)
100	2271	0	2	99.91	100.00	99.91
101	1864	0	1	99.95	100.00	99.95
102	2185	0	2	99.91	100.00	99.91
103	2085	0	0	100.00	100.00	100.00
104	2225	0	4	99.82	100.00	99.82
105	2570	0	2	99.92	100.00	99.92
106	2024	0	3	99.85	100.00	99.85
107	2137	0	0	100.00	100.00	100.00
108	1762	5	1	99.94	99.72	99.66
109	2529	0	3	99.88	100.00	99.88
111	2118	1	6	99.72	99.95	99.67
112	2539	0	0	100.00	100.00	100.00
113	1794	0	1	99.94	100.00	99.94
114	1877	0	2	99.89	100.00	99.89
115	1953	0	0	100.00	100.00	100.00
116	2406	10	6	99.75	99.59	99.34
117	1535	0	0	100.00	100.00	100.00
118	2277	0	1	99.96	100.00	99.96
119	1981	0	2	99.90	100.00	99.90
121	1862	0	1	99.95	100.00	99.95
122	2476	0	0	100.00	100.00	100.00
123	1518	0	0	100.00	100.00	100.00
124	1616	0	4	99.75	100.00	99.75
200	2593	0	8	99.69	100.00	99.69
201	1958	2	5	99.75	99.90	99.64
202	2129	0	7	99.67	100.00	99.67
203	2974	10	6	99.77	99.83	99.60
205	2654	3	2	99.92	99.89	99.81
207	1861	0	1	99.95	100.00	99.95
208	2954	7	1	99.97	99.76	99.73
209	3005	0	0	100.00	100.00	100.00
210	2650	7	0	100.00	99.74	99.74
212	2748	0	0	100.00	100.00	100.00
213	3249	0	2	99.94	100.00	99.94
214	2260	0	2	99.91	100.00	99.91
215	3360	0	3	99.91	100.00	99.91
217	2206	2	2	99.91	99.91	99.82
219	2151	1	3	99.86	99.95	99.81
220	2047	0	1	99.95	100.00	99.95
221	2421	0	6	99.75	100.00	99.75
222	2480	4	3	99.88	99.84	99.72
223	2599	0	6	99.77	100.00	99.77
228	2044	7	9	99.56	99.66	99.22
230	2253	0	3	99.87	100.00	99.87
231	1566	0	5	99.68	100.00	99.68
232	1780	4	0	100.00	99.78	99.78
233	3071	0	8	99.74	100.00	99.74
234	2753	0	0	100.00	100.00	100.00
Overall	109370	63	124	99.88	99.94	99.83

Chapter 4

A New Algorithm to Reduce T-wave Over-sensing based on Phase Space Reconstruction in S-ICD System

4.1 Introduction

In Western societies, 15%-20% of deaths are caused by sudden cardiac death (SCD) Haqqani et al. (2019), of which 80% are attributed to ventricular tachyarrhythmia Mehra (2007). Fortunately, in high risk individuals, the Implantable Cardioverter Defibrillator (ICD) has been shown to be highly effective in both the primary and secondary prevention of SCD. The fundamental aim of ICD therapy is to effectively terminate life-threatening rhythm disturbances by shock therapy. This can be achieved within a few seconds of arrhythmia onset and ICDs have been shown to be highly effective. The subcutaneous implantable cardioverted defibrillator (S-ICD) (Boston Scientific, MA, USA) is a relatively new defibrillator system, which has demonstrated a Ventricular Fibrillation (VF) conversion efficacy of greater than 97% in clinical trials Lambiase et al. (2014). Unfortunately, ICD recipients are also at risk of inappropriate shock therapy, where defibrillation is delivered in the absence of a life threating arrhythmia. Inappropriate shocks adversely affect quality of life and psychological health, can be responsible for the induction of ventricular arrhythmias, and are associated with increased mortality Proietti et al. (2015); Poole et al. (2008); Daubert et al. (2008); van Rees et al. (2011). A single inappropriate shock has also been shown to increase a patient's all-cause mortality Proietti et al. (2015). In S-ICD recipients inappropriate shock therapy has been reported to occur in up to 8% of patients per year, with the commonest cause being T wave over-sensing (TWOS) Lambiase et al. (2014); Burke et al. (2015); Boersma et al.

(2017); Nordkamp et al. (2015). This occurs when T waves, the surface ECG manifestation of ventricular repolarisation, are incorrectly counted as R waves, which are themselves the ECG feature denoting myocardial depolarisation. The consequence is double counting of the heart rate, which is highly significant as shock therapies are only ever considered above a programmable heart rate threshold. Over the decades, a number of automated algorithms have been developed to reduce TWOS. The first relative algorithm was introduced by Pan and Tompkins Pan and Tompkins (1985) and was based on the maximum slope of the T-wave. Other attempts at reducing TWOS have been based on frequency analysis Cao et al. (2012), morphology analysis Brisben et al. (2015) and a high-pass filter Boveda et al. (2018).

However, the major concern associated with these algorithms is their performance for reducing TWOS, in other words the detection accuracy of the real R-peaks. In this case, it is more important to reduce the number of false-positives (FPs) of R-peak detection, leading to a high positive predictivity (+P). Inspired by this fact, a novel automated TWOS rejection algorithm based on the phase space reconstruction, which is specifically designed to distinguish R and T-peak is proposed in this paper. The R-peaks are initially detected by hierarchical clustering technique Chen and Maharatna (2020), whilst the phase space features of a normal ECG template (Reference ECG) are used to identify all detected peaks and discard inappropriate detections. This technique is highly applicable to the S-ICD system, in which a recorded ECG template is already employed in tachycardia detection.

The rest of the chapter is organized as follows: in *Section* 4.2, we describe the S-ICD device and present the theoretical background of the PSR and box-counting. Then we explain our algorithm based on one example case in *Section* 4.3. we discuss our proposed algorithm for ECG R-peak and T-peak detection. The results and the discussion of the validation on our UHS database and MIT-BIH arrhythmia database are show in *Section* 4.4. Finally, the conclusion are drawn in *Section* 4.5

4.2 Theoretical Background

4.2.1 Transvenous ICD

The implantable cardioverter defibrillator (ICD) is a complex cardiac implantable electronic device, which is used to treat the VA and prevent from SCD. Normally, an ICD can diagnose and treat life-threatening VA by providing potentially lifesaving therapy within a few seconds after VA onset. The first generation ICD was introduced by Mirowski et al.

(1973) in 1973, and finally obtained the United States Food and Drug Administration (FDA) approval in 1985. In modern medicine, ICD can be generally divided into two types - Transvenous ICD (TV-ICD) and subcutaneous ICD (S-ICD) as shown in Fig.4.1. The left figure is an example of TV-ICD, which is comprised of two components; a pulse generator and transvenous defibrillation leads. TV-ICDs generally also have two types based on the number of transvenous leads. If the lead is attached proximally to the pulse generator and fixated distally to the endocardial surface of the right ventricle (RV), this type of TV-ICD is called VR-ICD. The one with two transvenous leads (Left of Fig.4.1) is named a dual chamber, or DR-ICD. ICD treatment strategies are primarily determined by heart rate. Shock therapies are only ever delivered if the heart rate exceeds a pre-determined threshold. In general, ICD system records the heart rate by calculating the R-R interval. For example, in S-ICD system, the heart rate is calculated using the average of four consecutive R-R intervals Wiles and Roberts (2017). Therefore, the R-wave detection is the most important element task in ICD systems.

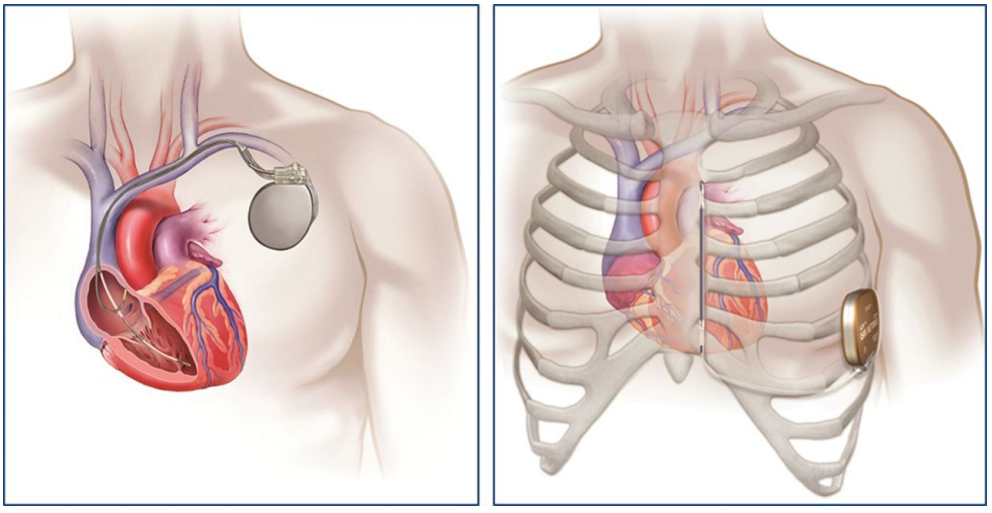

FIGURE 4.1: TImplantable cardioverter defibrillators (ICDs). (Left: TV-ICD comprising a pulse generator and two transvenous leads (right atrial and right ventricular). Right: a Boston Scientific S-ICD) Wiles and Roberts (2017)

4.2.2 Subcutaneous ICD

The S-ICD is implanted subcutaneously in individuals who are at high risk of SCD. It is comprised of a subcutaneous pulse generator and a single lead containing two sensing electrodes as shown on the right of Fig.4.1. After implantation the system continuously records ECG signal in one of three available vectors; primary, secondary and alternate (Fig.4.2). At least one vector must have a suitable ECG morphology, with large R:T ratios (large difference between R and T-waves) placing the recipient at high risk of over sensing. Non-invasive vector screening is therefore performed prior to implant, and post implantation the most favourable vector is selected for clinical use. The S-ICD continuously calculates the patient's heart rate by calculating ECG amplitude and comparing it

to a programmed and dynamically varying sensitivity level. Amplitudes above the sensitivity level are identified as R waves whilst amplitudes below this level are effectively ignored. 'Auto adjusting sensitivity' is utilised, whereby the sensitivity falls gradually after the detection of a R wave, before being rapidly increased to a percentage value of the next sensed R wave. This is designed to prevent under-sensing of low amplitude VF whilst minimising risk of T wave over-sensing.

Shock treatment is primarily determined by calculated heart rate (R-R interval), but more sophisticated algorithms are also employed once tachycardia has been detected. For example, ECG morphology is used to distinguish between rapid arrhythmia originating in the ventricle and those originating in the atria. This is important as the latter are not expected to be life threatening, so do not require shock therapy. To achieve this, a template of each vector is stored by the S-ICD system at implant (and updated at subsequent check-ups). This records that individual's ECG morphology in normal rhythm, allowing later comparison to the morphology during tachycardia. Where the morphology matches the template, an atrial origin is indicated, and shock therapy can be appropriately withheld. In a similar way, we hypothesise that a stored template could be used to prevent shock therapy from being delivered where tachycardia had been incorrectly diagnosed as a result of T wave over-sensing.

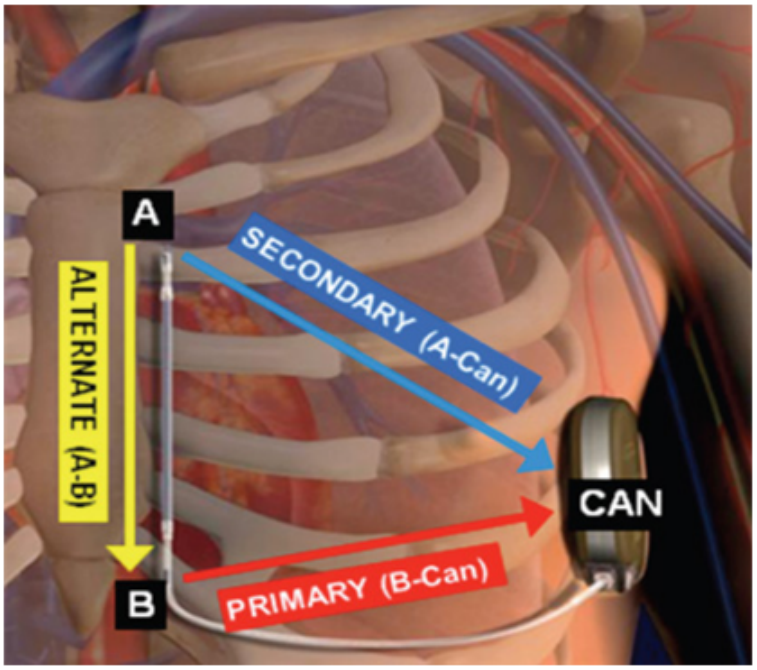

FIGURE 4.2: The three S-ICD sensing vectors Cappelli et al. (2014)

4.2.3 PSR and box-counting in ECG

PSR is common method to analyse the chaotic characteristics of non-linear signals Fan et al. (2018). Recently, it is widely applied for ECG processing, a PSR based algorithm for heartbeat classification is presented in Nejadgholi et al. (2011). PSR methods for ECG fiducial point detection can be found in Plesnik et al. (2012); Hou et al. (2018). It was also an important role in ECG noise removal Lee et al. (2002), fetal ECG monitoring Wei et al. (2012) and human identification Fang and Chan (2009). In addition, PSR technique has been used successfully for arrhythmia analysis, such as VT/VF detection Sarvestani et al. (2009). It reconstructs the trajectory by plotting the original signal and its delayed versions in a multi-dimensional phase space. Consider a signal with one-dimension $x[i]$, where $i = 1, 2, ..N$, N is the number of data samples. The delay signal is $x[i - \tau]$, where τ is the delay time. Then the two-dimensional phase space diagram can be plotted in the co-ordinate system. In general, the x-axes is original signal and the y-axes represents the delay signal. An example based on ECG signal is shown in Fig.4.3.

Box counting technique is usually used with PSR to analyse the statistical features of the trajectories in a phase-space diagram Vemishetty et al. (2019). The phase-space diagram is divided into $N \times N$ pixels, where N is an integer. An example is given in Fig.4.4. In this case, phase-space diagram of normal ECG is plotted based on 0.02 seconds time delay and it is divided into 25×25 pixels. Cappiello et al. (2014) suggested that 20 samples is an appropriate delay for the optimum PSR analysis of ECG signals with 1 KHz sampling frequency, which means 0.02 seconds time delay gives good person-centric characterization among various other embedding delays. One or more trajectories in the phase-space diagram pass through pixels are considered as black boxes (n_b) and others are white boxes (n_w). The number of (n_b) among all pixels can reflect the spread of these trajectories and thus is possible feature to distinguish R and T-wave, since different waves have the different phase space features. Following the exploration reported in Hou et al. (2018), the trajectories of QRS complex in the phase space diagram are located relatively far away from the diagonal line and the trajectories of other ECG features are concentrated near the diagonal line. Comparing to the trajectories of T-wave, the trajectories of QRS complex are more spread out in a same phase space diagram and leading to a larger n_b. This phenomenon is relative to the difference of morphology rather than the amplitude. Therefore, it may help us to distinguish the QRS complex and TWOS.

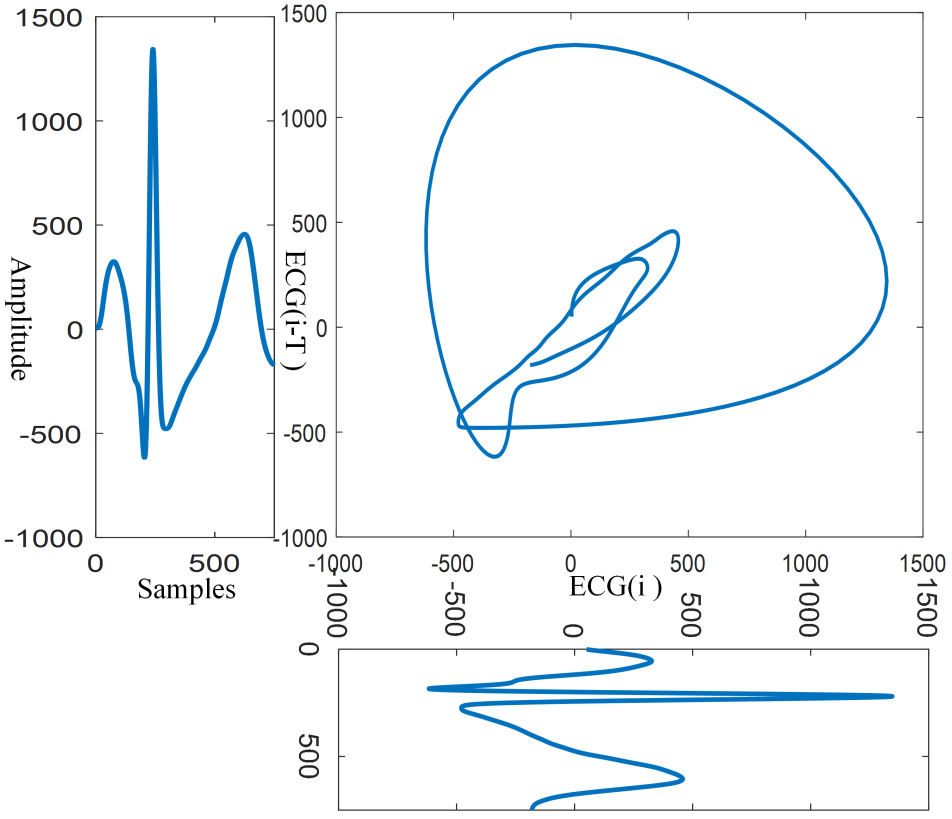

FIGURE 4.3: ECG signals and the corresponding phase-space diagram

4.3 Methodology

The flow chart of our proposed algorithm is shown in Fig.4.5. It can be divided into three main steps. First is data pre-processing and initial R-peak detection. The second step is to extract features of the template using PSR and box-counting technique. Finally identifying all detected R-peaks and discard the inappropriate detections.

4.3.1 Data pre-processing and R-peak detection

The first stage is data pre-processing and initial R-peak detection. A fourth-order Butterworth high-pass filter with 1 Hz cut-off frequency and a low-pass filter with 30 Hz cut-off frequency are appiled to remove the noise and baseline wandering of the raw signals Amann et al. (2005). Then, the filtered signals were normalized using (4.1) in order to put all values in the range of [0,1]. Finally, all R-peaks were initially detected using the hierarchical clustering technique Chen and Maharatna (2020) and recorded as $QRS[i]$, where $i = 1, 2, ..N$, N is the number of the R-peaks. The results of R-peak detection using the hierarchical clustering based on a part of the UHS record (No.3)

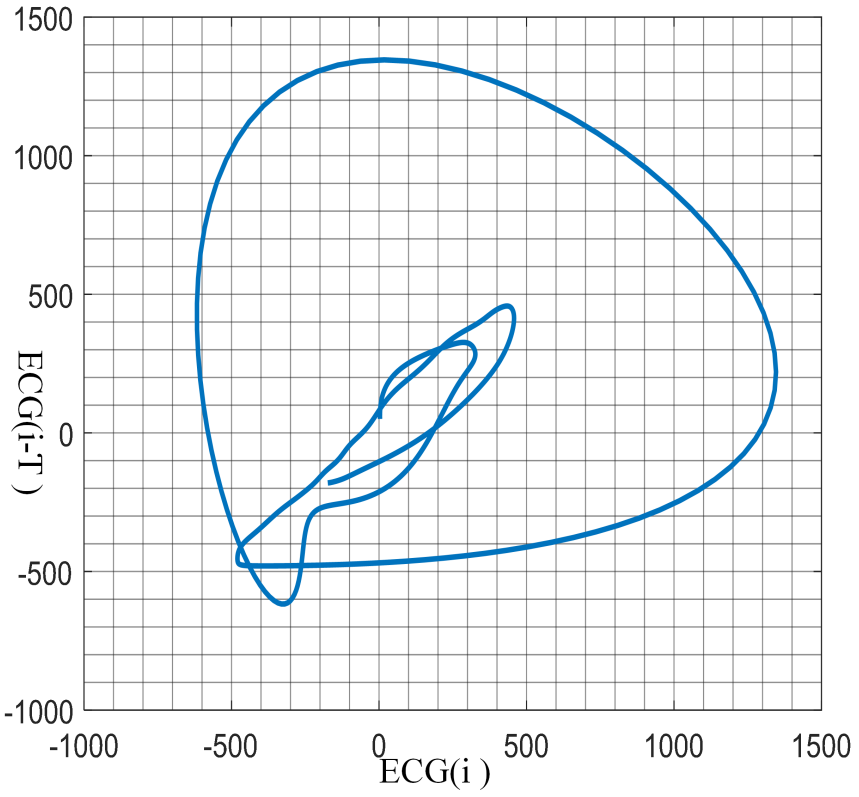

FIGURE 4.4: Box counting in phase-space diagram (N=25).

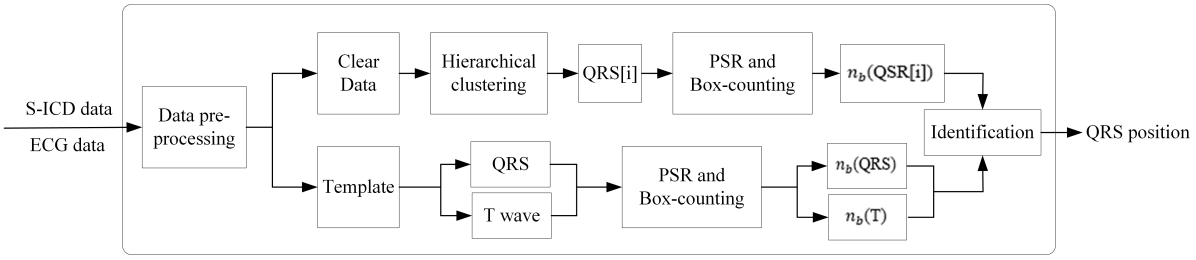

FIGURE 4.5: The system overview of the proposed algorithm

with 14 TWOS are shown in Fig.4.6. For this example, although hierarchical clustering can reduce the TWOS, there still exits 5 inappropriate detections. These large T-waves are identified as R-waves due to their sharp morphology and high amplitude.

$$\widetilde{E}(n) = (E(n) - E_{min}) / (E_{max} - E_{min}) \tag{4.1}$$

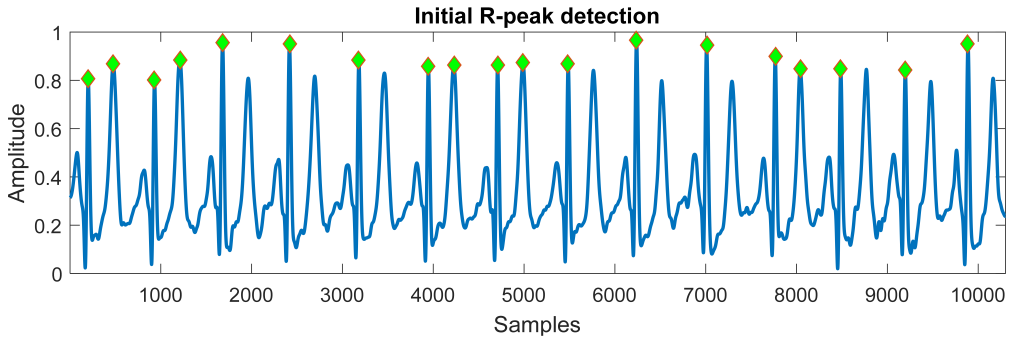

FIGURE 4.6: The initial result before removing inappropriate detections of R-peak

4.3.2 Template analysis

In the second stage, we first obtain the template in subject-specific way. For UHS records, specific template of each subject is defined by an Electrophysiologist. For MIT-BIH arrhythmia records, each template is collected by randomly selecting a normal beat with a well-behaved QRS complex in each subject that are annotated by cardiologists Goldberger et al. (2000). Fig.4.7 is an example of a template with the determined QRS complex and T-peak. The green diamond is marked as R-peak (t_0). Moreover, the QRS-onset and QRS-offset are t_1 and t_2 respectively, T-peak is t_3. Next step is to analyse phase-space features of QRS and T-wave. In order to put them into a uniform platform, the length of QRS and T-wave should be same as $t_2 - t_1$. In this case, T wave boundary is considered as $[t_3 - (t_0 - t_1),\ t_3 + (t_2 - t_0)]$. The phase-space diagrams of QRS complex and T-wave are shown in Fig.4.8 and Fig.4.9 respectively. Finally, box-counting technique is used to analyse the trajectories of QRS complex and T-wave. In our work, the phase-space diagram is divided into $2^{10} \times 2^{10}$ pixels Cappiello et al. (2014). For this example, the numbers of black box of QRS complex ($n_b(QRS)$) and T-wave ($n_b(T)$) are 3511 and 1719 respectively.

4.3.3 Identification of real R-peak

In the first stage, we initially obtained all R-peaks $QRS[i]$. A part of results with incorrect detection of R-peaks based on the previous example is shown in Fig.4.10. Two T-peaks are detected as R-peaks because of their relatively high amplitude. In order to remove such inappropriate detections (TWOS). We analysed the phase-space features of all detected "QRS complex". The range of each QRS complex is same as the template, the position of each detected R-peak is considered as t'_0, then the QRS onset and QRS offset are t'_1 and t'_2 respectively. The distances between all points (QRS onset, R-peak ,QRS offset) are same as the template. Then the box-counting technique is applied to count the number of black box and recorded as $n_b(QRS[i])$ for all corresponding QRS complexes $QRS[i]$. Finally, $n_b(QRS[i])$ is compared with $n_b(QRS)$ and $n_b(T)$. If the

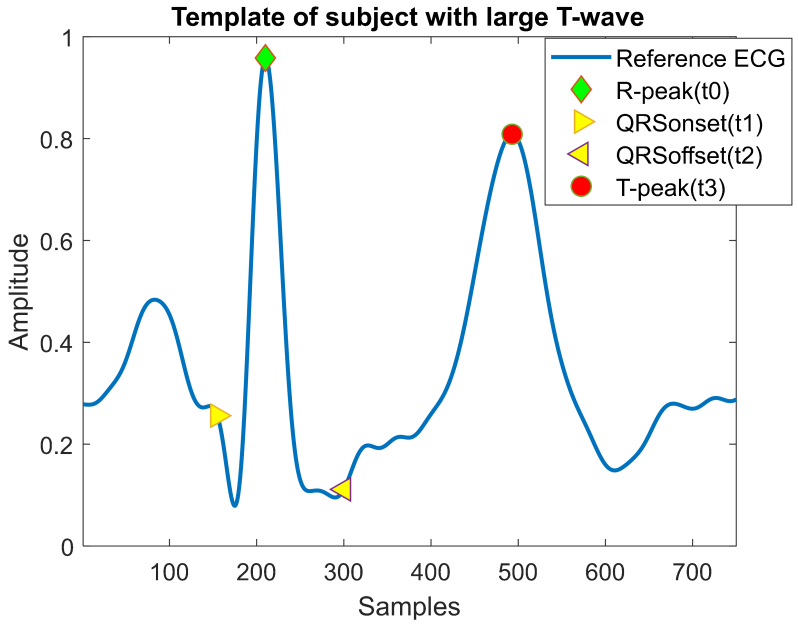

FIGURE 4.7: The template of a normal heart beat (annotation: Patient No.3 from NSH database)

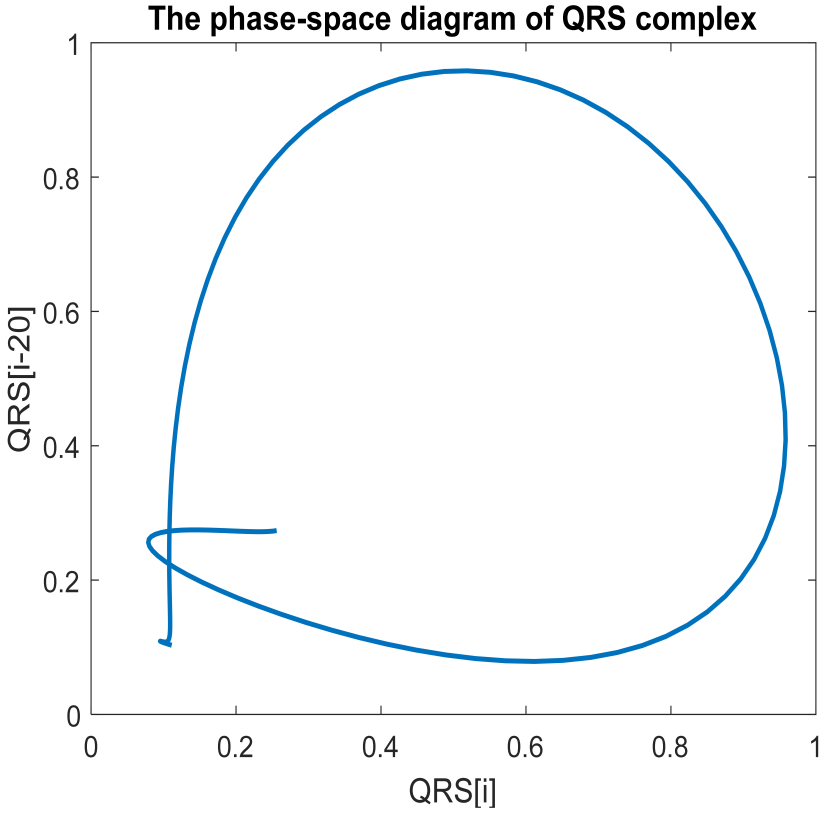

FIGURE 4.8: The phase-space diagram of QRS complex template (annotation: Patient No.3 from UHS database)

value is closer to the $n_b(T)$, this QRS[i] will be removed and considered as an inappropriate detection. After removing these inappropriate detections, the rest of the detected

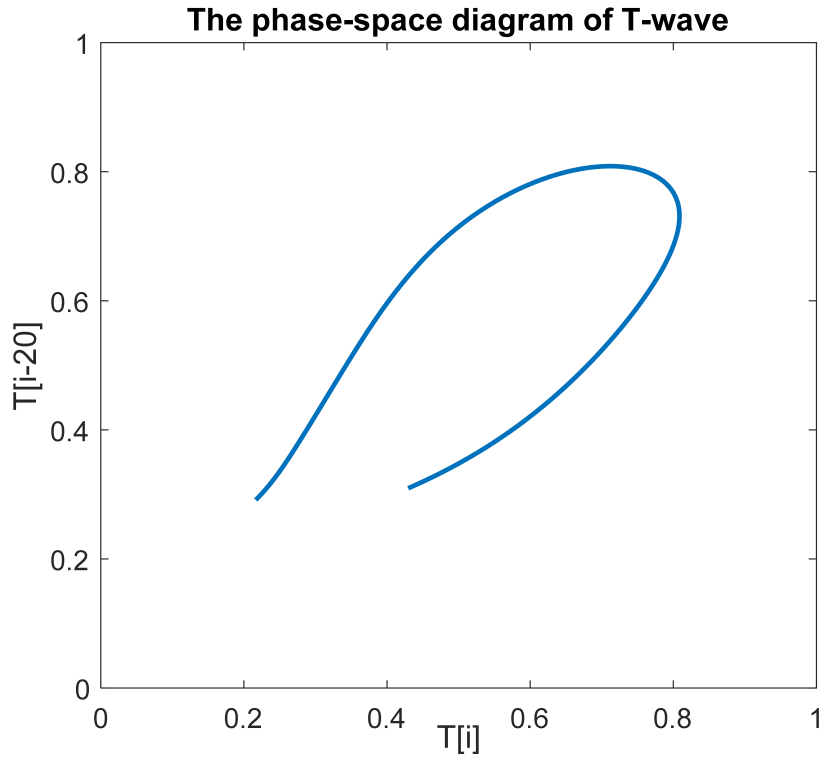

FIGURE 4.9: The phase-space diagram of T-wave template (annotation: Patient No.3 from UHS database)

R-peaks will be considered as real R-peaks. The results of the previous example (UHS record No.3) are shown in Fig.4.11.

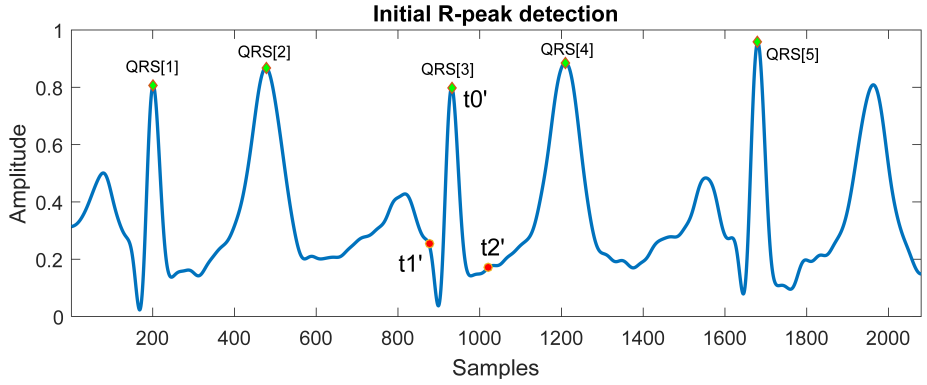

FIGURE 4.10: A part of results with incorrect detection of R-peaks based on the previous example of T wave over-sensing (Fig.4.6)

4.3.4 Additional function for VF detection

The entire principle of the S-ICD is that it has to detect the low amplitude R waves during ventricular fibrillation (VF) and it must do this whilst also managing to not

Table 4.1: Pseudocode of the proposed algorithm

Pseudocode of the proposed Algorithm
Input: A sequence of ECG signal E[i]
Template T[i] (R-peak(t0), QRS onset(t1),QRS offset(t2), T-peak(t3))
1. Pre-processing and normalization E[i], T[i]
2. Hierarchical clustering QRS[i], i=1,2...N
3. x1=T[t1,t2], y1=T[t1-20,t2-20]
4. x2=T[t3-(t0-t1),t3+(t2-t0)], y2=T[t3-(t0-t1)-20,t3+(t2-t0)-20]
5. PSR technique **Fig**(QRS)=(x1,y1),**Fig**(T)=(x2,y2)
6. Box-counting n_b(QRS) and n_b(T)
7. **for** i=1:N
8. x[i]=E[QRS[i]-(t0-t1),QRS[i]+(t2-t0)]
9. y[i]= E[QRS[i]-(t0-t1)-20,QRS[i]+(t2-t0)-20]
10.PSR technique **Fig**(QRS[i])=(x[i],y[i])
11.Box-counting n_b(QRS[i])
12.b1=**abs**(n_b(QRS[i]),n_b(QRS)), b2=**abs**(n_b(QRS[i]),n_b(T))
13. **if** b1>b2
14. QRS[i] is removed
15. **end if**
16.**end for**
Additional function for abnormal R waves detection
17. **if** n_b(QRS[i]) $> 1.2 \times n_b(QRS)$
18. QRS[i] is an abnormal R wave not **TWOS**
19. **end if**

oversense T waves during normal rhythm. Hence, the main task of S-ICD system is not only reducing TWOS during normal rhythm but also detecting abnormal R-waves during VF. However, our algorithm based on the healthy template may discard such abnormal R-waves during VF. Following the exploration report in Cappiello et al. (2014), comparing to a phase space diagram of healthy ECG signals, a phase space diagram constructed using an equivalent length of the VF signals is more chaotic. It shows large chaotic motions in all trajectories indicating towards a larger n_b. In order to reduce T-wave oversensing without impacting the detection of R-waves during VF, it is possible to set a threshold to detect such abnormal R-waves during VF. Based on our experimental results of 10 USH records with VF, the n_b of R-waves during VF is at least 20% larger than the normal R-waves. Therefore, once the n_b of the detected R-waves are larger than $1.2 \times n_b(QRS)$, these R-waves will be considered as abnormal R-waves rather than TWOS. The pseudocode of our proposed algorithm is presented in Table 1. In this case, x1 and y1 represent the x-axes and y-axes of phase-space diagram of the R-wave template respectively, x2 and y2 are the x-axes and y-axes of phase-space diagram of the T-wave template. Furthermore, x[i] and y[i] represent the x-axes and y-axes of each phase-space diagram of detected R-wave, where N is the number of R-wave.

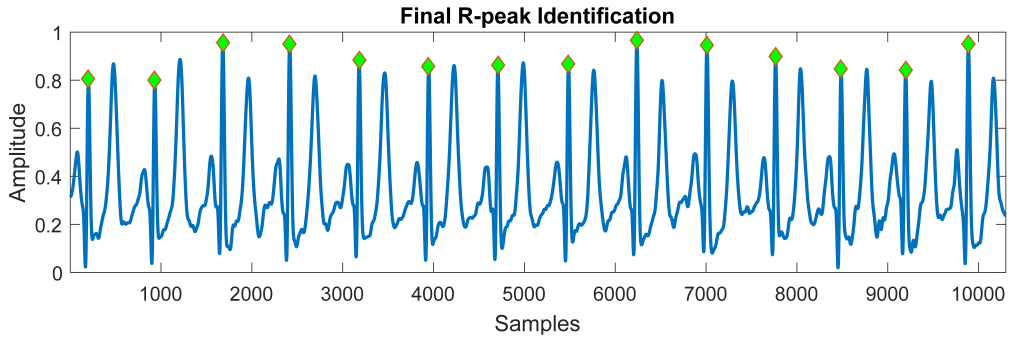

FIGURE 4.11: The final result after removing inappropriate detections of R-peak by using PSR

4.4 Results and Discussion

4.4.1 Data and Validation

All ECG signals were obtained from either the UHS or publicly available MIT-BIH arrhythmia database Goldberger et al. (2000). The UHS ECG signals were obtained from 34 adult patients undergoing ECG recordings at the UHS. Among 34 recordings, 10 recordings are 1-hour normal rhythm followed by 15 seconds VF, rest 24 1-hour records are all normal ECG signals. . Informed written consent was provided by all participants. ECG signal was obtained using a five-lead two channel digital Holter recorder (Model AFT-1000, Holter Supplies, Paris) positioned using anatomical landmarks to recreate the primary and secondary sensing vectors of an S-ICD. The Holter data was downloaded in ASCII format at a frequency of 1 KHz and a template file showing 30 seconds of stable intrinsic rhythm created by an Electrophysiologist, who also visually identified the R and T wave components in each signal. In clinical practice surface ECG is accepted as a suitable surrogate for the S-ICD vectors, and is used for all pre-implant screening assessments to determine suitability for the device. Besides, in the absence of a life-threatening dysrhythmia, only limited ECG data can be downloaded from the S-ICD system (10 seconds). As such this study could not have been performed using S-ICD data. S-ICD vectors and surface ECG data recorded in exactly this manner (using this Holter device setup) have been shown to be highly correlated Wiles et al. (2018). Therefore, these records are acceptably considered as S-ICD signals. In order to evaluate the performance of our proposed algorithm, we calculated sensitivity $Se = TP/(TP+FN)$, positive predictivity $+P = TP/(TP+FP)$ and accuracy $Acc = TP/(TP+FP+FN)$, where TP represents the true positives (R-peaks are detected correctly), FN is the false negatives (R-peaks are not detected)and FP is the false positives (R-peaks are detected improperly). Among these 34 records, there are 166 TWOS, which are defined when the amplitude of T-peak is larger than R-peak in a same heart beat. . In addition, all abnormal R-waves during VF are detected by our proposed algorithm, which are validated based on 10 recordings with VF. In order to evaluate our algorithm for reducing TWOS,

TABLE 4.2: The R-peak detection performance comparison in our UHS database.(Numerators are the number of T-peaks that are identified as R-peaks)

Authors	Method Used	TP	FP	FN	Se[%]	+P[%]	Acc[%]	TWOS
Mazomenos et al. (2013)	HFEA	183681	1094	1163	99.37	99.41	98.79	149/166
This work	HFEA + PSR	183627	12	1217	99.34	99.99	99.88	0/166
Chen and Maharatna (2020)	Hierarchical clustering	184652	108	192	99.90	99.94	99.84	74/166
This work	Hierarchical clustering + PSR	184631	12	213	99.88	99.99	99.88	0/166

we also found the source code of Hybrid feature extraction algorithm (HFEA) for R-peak detection Mazomenos et al. (2013). The main reason for choosing this algorithm is that our proposed PSR based algorithm requires a healthy template and this algorithm also need to define a healthy template for R-peak detection. They were compared with our proposed method based on UHS database. The comparison results are shown in Table 4.2.

Concerning the MIT-BIH arrhythmia database, it has 48 30-minutes records and the sampling frequency is 360Hz. In this work, all records are used to evaluate our algorithm. The sensitivity Se and positive predictivity $+P$ are calculated by considering the range of 150ms ($\pm$75ms) based on the AAMI-ECAR guidelines ECAR (1987) in order to compare with our previous method and other methods in the same condition. Table 4.3 compares the R-peak detection results of MIT-BIH arrhythmia database by different methods, including two algorithms based on our previous work Mazomenos et al. (2013) Chen and Maharatna (2020). In addition, Table 4.4 provides the effectiveness of our proposed method in terms of false positives and false negatives of R-peak detection for some specific MIT-BIH records.

4.4.2 Method Evaluation

Table 4.2 shows the performance of the proposed algorithm when combined with two different R-peak detection algorithms, viz. Chen and Maharatna (2020) and Mazomenos et al. (2013). It can be seen from Table 4.2, the highest performance overall was achieved when we combine our algorithm with hierarchical clustering Chen and Maharatna (2020) - 99.88% Se, 99.99% +P and 99.88% Acc. The proposed algorithm also shows a high performance to reduce TWOS based on UHS database. Among 166 TWOS in all records, our proposed method can find all TWOS and remove them. Comparing our work to Chen and Maharatna (2020) and Mazomenos et al. (2013), PSR algorithm significantly reduces the TWOS at the expense of slightly increase of false negatives (FNs) of R-wave detection. This limitation is due to the false detection of abnormal R-waves during normal rhythm. Some R-waves with abnormal situations give us a relatively small n_b and thus might be identified as TWOS. For example, a small QRS-complex, a wide QRS-complex with baseline or noise. Another interesting thing is that no matter what

TABLE 4.3: The R-peak detection performance comparison in the MIT-BIH Arrhythmia database.(The window used for defining a true positive is reported as w, N/R: Not Reported)

Authors	Method Used	w[ms]	TP	FP	FN	Se[%]	+P[%]	Acc[%]
This work	**Hierarchical clustering + PSR**	**150**	**109347**	**16**	**147**	**99.87**	**99.99**	**99.85**
This work	**HFEA + PSR**	**150**	**108181**	**16**	**1313**	**98.80**	**99.99**	**98.79**
Chen and Maharatna (2020)	Hierarchical clustering	150	109370	63	124	99.89	99.94	99.83
Hou et al. (2018)	Phase Portraits	N/R	109254	610	748	99.32	99.45	N/R
Mazomenos et al. (2013)	HFEA	150	108250	938	1244	98.86	99.14	98.02
Merah et al. (2015)	Stationary wavelet transform(SWT)	100	109316	126	178	99.84	99.88	99.72
Saadi et al. (2015)	Optimized adaptive thresholding	150	N/R	N/R	N/R	99.90	99.87	N/R
Thiamchoo and Phukpattaranont (2016)	Continuous wavelet transform(CWT)	N/R	109135	356	185	99.69	99.83	99.52
Smaoui et al. (2017)	Continuous wavelet transform(CWT)	N/R	N/R	168	756	99.37	99.83	N/R
Cesari et al. (2017)	Wavelet transform (WT)	150	109321	147	173	99.84	99.87	99.71
Friganovic et al. (2018)	Mathematical morphological filter	150	98659	268	214	99.78	99.72	99.52
Zalabarria et al. (2020)	Iterative state machines	N/R	106096	431	485	99.54	99.60	N/R
Kaur et al. (2019)	self-convolution window(SCW)	100	109416	53	76	99.93	99.95	99.83

TABLE 4.4: Comparison of the numbers of false-positives (FPs) and false negatives (FNs) based on R-peak detection for specific records of the MIT-BIH arrythmia database, (where **N/A** is Noise and Artefact, **BD** is Baseline Drifts, **IR** is Irregular Rhythmic, **VA** is Ventricular Arrhythmias, **SCR** is sudden changes in R-peak, **HT** and **HP** are high T-peak and P-peak respectively, **PVCs** is Premature Ventricular Contractions and **sQRS** is small QRS complexes.)

No.	Characteristics	Number of FN/FP detection						
		Chen and Maharatna (2020)	Hou et al. (2018)	Merah et al. (2015)	Thiamchoo and Phukpattaranont (2016)	Smaoui et al. (2017)	Zalabarria et al. (2020)	**This work**
104	N/A	4/0	16/21	9/12	13/15	0/32	1/3	**4/0**
105	N/A	2/0	20/41	17/11	14/22	0/25	2/9	**2/0**
108	N/A, BD, HP	1/5	11/9	14/10	19/12	18/19	2/73	**1/3**
113	HT	1/0	0/34	1/4	0/8	0/0	0/0	**0/0**
116	BD, sQRS	6/10	6/18	4/7	21/2	25/2	3/1	**13/0**
200	N/A, VA	8/0	2/2	3/0	8/16	2/7	2/0	**6/0**
203	N/A, BD, IR, VA	6/10	94/124	16/10	72/14	65/24	61/24	**7/5**
208	BD, PVCs, sQRS	1/7	32/32	9/3	25/4	143/4	76/4	**0/0**
210	N/A, BD	0/7	40/39	5/3	27/3	58/4	17/1	**0/2**
222	BD, IR, HP	3/4	18/8	8/5	2/1	0/1	11/0	**7/0**
223	SCR	6/0	38/5	3/0	1/1	2/0	22/0	**0/0**
228	N/A, BD	9/7	75/24	9/7	9/19	7/19	2/9	**9/1**
232	BD	0/4	4/6	0/10	0/4	0/2	93/12	**0/0**
233	VA	8/0	0/0	1/0	4/0	4/0	87/0	**0/0**
Total		55/54	356/363	99/82	215/121	324/139	379/136	**49/11**

algorithm was combined to our proposed PSR based algorithm, the results for reduction TWOS are the same. This phenomenon reflects that PSR algorithm has potential to combine to any other R-wave detection algorithm to reduce the TWOS with the same result. This is particularly suitable for such S-ICD sensing algorithm, since it requires the healthy template as well.

Our method based on hierarchical clustering and PSR achieved a Se of 99.87%, a +P of 99.99% and an Acc of 99.85% over MIT-BIH arrhythmia database for R-peak detection. From Table 4.3, the +P and Acc of our proposed method are higher than other methods. Also, our method achieves a higher Se than other approaches except the one in study Kaur et al. (2019). The results show our method has the same Se with Kaur et al. (2019), however, the number of FNs of R-peak detection (81) is slightly larger than it (76) in literature Kaur et al. (2019). From Table 4.3, concerning hierarchical clustering and HFEA algorithms, after applying PSR based algorithm, the FPs of R peak detection reduce to 16, leading to a high +P of 99.99%. It shows the same point as we discovered in UHS database, PSR algorithm can be applied for different algorithms with the same improvement for R-peak detection. Most of the common real-time R-wave detection algorithms are based on the wavelet transform (WT) Merah et al. (2015) Thiamchoo and Phukpattaranont (2016) Smaoui et al. (2017) and Cesari et al. (2017), since WT gives a low computational complexity, but it also shows relatively lower performance for R-wave detection. Some other novel algorithms such as hierarchical clustering Chen and Maharatna (2020) and self-convolution window (SCW) Kaur et al. (2019) show a high performance to detect R-wave but the computational complexity is relatively higher. Overall, an important characteristic of our proposed method is getting the same FPs of R-peak detection even if it combines to the different R-peak detection algorithms. Although our proposed algorithm may slightly increase the FNs of R-peak detection, the FPs of R-peak detection are significantly decreased- leading to a reduction of TWOS.

A detailed result in terms of FPs and FNs for R-peak detection for some specific MIT-BIH records are shown in Table 4.4. As mentioned before, our algorithm is based on the hierarchical clustering and PSR technique. The FPs and FNs of R-peak detection are 11 and 49 respectively. Comparing with other methods, our proposed algorithm can efficiently reduce the FPs of R-peak detection for these records. Actually, in this case the FPs are only occurring for the records that are corrupted with noise and artefacts. It also shows that our proposed method gets a relatively larger number of FNs of R-peak detection in records with abnormal QRS complexes, particularly in those records with small QRS complexes or baseline drifts. For a small QRS complex or an R-wave with baseline, the number of black boxes might be lower than normal QRS complex, and therefore are identified as inappropriate detections by our algorithm. Besides, the detailed performance of the proposed algorithm on 48 ECG records from MIT-BIH arrhythmia database is shown in Table 4.5. We only show the performance based on

hierarchical clustering with PSR in this work. Since it gives a better result than HFEA with PSR for R-peak detection.

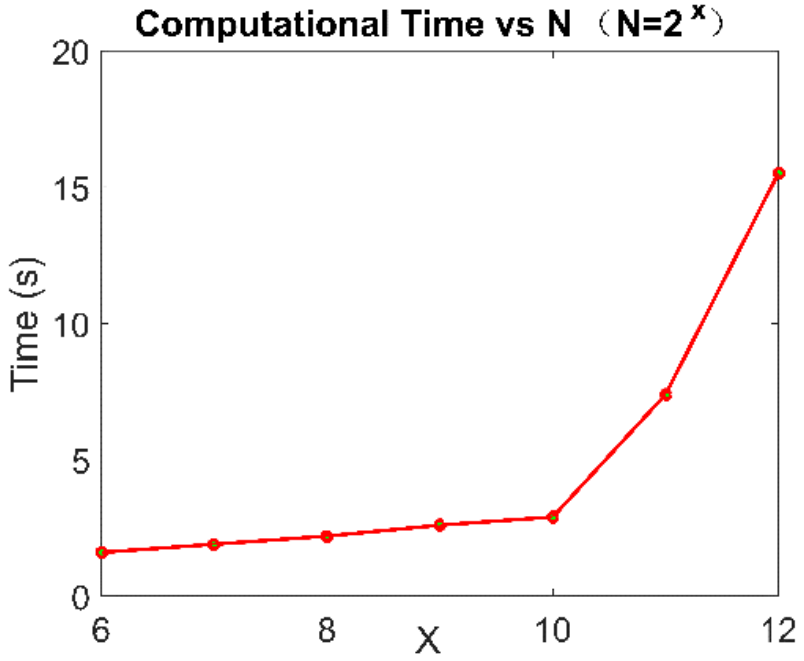

FIGURE 4.12: The run time against N for processing of one-minute ECG record

4.4.3 Complexity analysis

The implementation of our proposed algorithm for validation took place in MATLAB R2018a. The computational complexity of our algorithm is briefly given in Table 4.6. In our proposed algorithm, the main computational complexity is due to determine the number of black boxes in the PSR diagram. The PSR diagram is divided into $N \times N$ pixels, hence, the computational complexity of the proposed algorithm is $O(N^2)$. In addition, the average run-time of our proposed algorithm for 1-min ECG record against the value of N is plotted in Fig.4.12. The computational time rise steadily when the value of N increases from 2^6 to 2^{10} and the run-time is 2.9 seconds at 2^{10}. However, it increases suddenly at $N = 2^{11}$ from 2.9 seconds to 7.4 seconds and finally goes to 15.5 seconds at $N = 2^{12}$. The Fig. 4.13 shows how much the number of pixels can affect the reduction of TWOS while our proposed algorithm was combining with hierarchical clustering Chen and Maharatna (2020). As mentioned in Table 4.2, the number of TWOS before applying PSR method is 74. After using our proposed algorithm, is shows that the value of N is proportionate to the reduced number of TWOS. And the number of TWOS decreases to 0 when N is larger than2^{10}. Overall, we think the optimum performance is achieved for $N = 2^{10}$. Although our proposed algorithm needs to combine with other R-peak

TABLE 4.5: R-peak detection results of evaluating the proposed algorithm performance on MIT-BIH arrhythmia database

MIT-BIH	TP	FP	FN	SE(%)	+P(%)	Acc(%)
100	2271	0	2	99.91	100.00	99.91
101	1863	0	2	99.89	100.00	99.89
102	2185	0	2	99.91	100.00	99.91
103	2085	0	0	100.00	100.00	100.00
104	2225	0	4	99.82	100.00	99.82
105	2570	0	2	99.92	100.00	99.92
106	2024	0	3	99.85	100.00	99.85
107	2137	0	0	100.00	100.00	100.00
108	1762	3	1	99.94	99.83	99.77
109	2529	0	3	99.88	100.00	99.88
111	2118	0	6	99.72	100.00	99.72
112	2539	0	0	100.00	100.00	100.00
113	1794	0	1	99.94	100.00	99.94
114	1877	0	2	99.89	100.00	99.89
115	1953	0	0	100.00	100.00	100.00
116	2399	0	13	99.46	100.00	99.46
117	1533	0	2	99.87	100.00	99.87
118	2277	0	1	99.96	100.00	99.96
119	1981	0	2	99.90	100.00	99.90
121	1861	0	2	99.89	100.00	99.89
122	2476	0	0	100.00	100.00	100.00
123	1518	0	0	100.00	100.00	100.00
124	1616	0	4	99.75	100.00	99.75
200	2592	0	9	99.65	100.00	99.65
201	1958	2	5	99.75	99.90	99.64
202	2129	0	7	99.67	100.00	99.67
203	2973	5	7	99.77	99.83	99.60
205	2654	3	2	99.92	99.89	99.81
207	1861	0	1	99.95	100.00	99.95
208	2948	0	7	99.76	100.00	99.76
209	3005	0	0	100.00	100.00	100.00
210	2650	2	0	100.00	99.92	99.92
212	2748	0	0	100.00	100.00	100.00
213	3249	0	2	99.94	100.00	99.94
214	2260	0	2	99.91	100.00	99.91
215	3360	0	3	99.91	100.00	99.91
217	2206	0	2	99.91	100.00	99.91
219	2151	0	3	99.86	100.00	99.86
220	2047	0	1	99.95	100.00	99.95
221	2421	0	6	99.75	100.00	99.75
222	2476	0	7	99.72	100.00	99.72
223	2599	0	6	99.77	100.00	99.77
228	2044	1	9	99.56	99.95	99.51
230	2253	0	3	99.87	100.00	99.87
231	1566	0	5	99.68	100.00	99.68
232	1780	0	0	100.00	100.00	100.00
233	3071	0	8	99.74	100.00	99.74
234	2753	0	0	100.00	100.00	100.00
Overall	109347	16	147	99.87	99.99	99.85

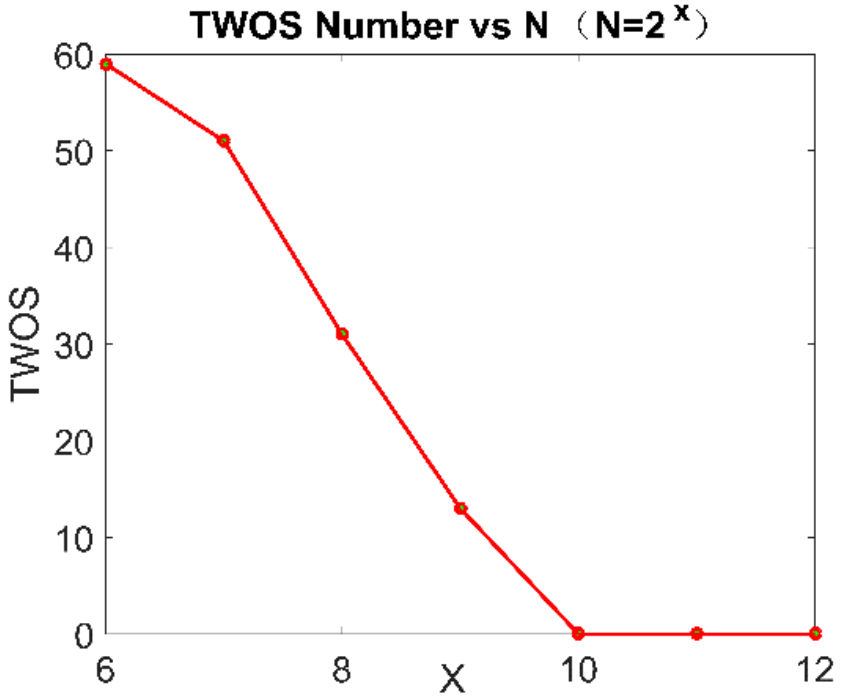

FIGURE 4.13: Number of TWOS is determined versus number of pixels in row or column for different N (Combining with hierarchical clustering)

TABLE 4.6: Computational complexity of the proposed scheme. Parameter N is the number of pixels in row or column and directly affect the order of computation

The proposed method	Order of computation
Step1: PSR and box-counting	O(N^2)

detection algorithms, the average computational time for processing of one minute ECG signals is only 2.9 seconds.

4.5 Concluding Remarks

This work in this chapter presents a novel algorithm based on PSR and box-counting techniques to reduce the TWOS in S-ICD systems. The performance of our proposed method has been evaluated with the database from UHS and MIT-BIH arrhythmia database. The results show our proposed method can identify TWOS and effectively reduce the number of TWOS from 166 to 0 based on UHS database. Our future work will be to integrate this algorithm with ICD/S-ICD and real-time performance evaluation of the integrated system. In this regard, we anticipate translating this algorithm into a computationally "light-weight" version without sacrificing its accuracy so that the system's battery life could be enhanced. However, S-ICD can only detect VA until it occurs. If the existing S-ICD system can be modified to predict and classify impending

VA, it can effectively improve patient's quality of life (QoL) and pre-empt a SCD episode. Therefore, in the next chapter, we will present a novel algorithm to predict and classify impending VA that not only could be incorporated in an S-ICD system but also in the other systems used for the similar clinical purposes.

Chapter 5

Prediction and Classification of Ventricular Arrhythmia based on Phase-Space Reconstruction and Fuzzy C-means Clustering

5.1 Introduction

The main reason behind the Sudden Cardiac Death (SCD) is fatal ventricular arrhythmias (VA) Szabó et al. (2020). The most attempt to characterise SCD risk from ECG analysis has been on a static population basis trying to predict patient cohorts where the risk of SCD is sufficiently high to warrant prophylactic treatment with implantable cardioverter defibrillator (ICD) Levy et al. (2009). Different approaches for predicting and classifing arrhythmia have been explored as shown in Section 2.4.3. However, the main emphasis of these works have been on prediction of non-fatal arrhythmia rather than prediction of fatal arrhythmia. Another point to note is that in the proposed classification methods successful classification of arrhythmia could be done only after the actual arrhythmic event takes place. There is almost no literature that has taken a holistic view of prediction and classification of arrhythmia before the actual arrhythmic event occurrence Cappiello et al. (2014). Inspired by this fact, the aim of our work is to develop a novel arrhythmia analysis methodology which can not only predict the impending fatal VA but is also capable of classifying the type of impending VA. In this paper, we firstly adapted a novel approach seeking to identify ECG features to predict the impending VA based on phase-space reconstruction (PSR) and box-counting techniques. Then a fuzzy c-means (FCM) clustering based classifier is proposed to classify four different types of impending VA (VA without ventricular premature beats (VPBs),

VT, VF and VT followed by VF).

The rest of this chapter is organized as follows: in Section 5.2, we introduce the possible problems of the previous work and the theoretical background of used techniques in this work. Then we describe our algorithm in Section 5.3. The results and the discussion of the validation on 64 records from PTB diagnostic ECG database (PTBDB) and CU ventricular tachyarrhythmia database(CUDB) are show in Section 5.4. Finally, conclusions are drawn in Section 5.5.

5.2 Theoretical Background

The formation mechanism of the arrhythmia might be considered as a cumulative effect of phase relationship between heart electrical activities which leads to a desynchronisation operation of the heart Cappiello et al. (2014). Such cumulative effect pushes the heart activity towards chaotic behaviour and finally leads to arrhythmia with the increasing of desynchronized operations of the heart. At the same time, the ECG signals change to the random fluctuations (VT/VF) rather than the normal P-QRS-T pattern. Although the variation of the phase relationship between electrical activities occurring at different part of the heart is small during the temporal drift before the arrhythmia onset, it is a cumulative process finally leading to arrhythmia. Hence, it is possible to develop a statistical index based on phase-space analysis to present such cumulative process and predict the impending arrhythmia.

For VA prediction, we developed a system that takes inspiration from the previous work of Cappiello et al. (2014) based on the PSR and box-counting techniques. In the previous work, measures of descriptive statistics like mean (μ), standard deviation (σ), coefficient of variation ($CV = \sigma/\mu$), skewness (γ) and kurtosis (β) in phase space diagrams were studied for a sliding window of 10 beats of ECG signal using the box-counting technique. Subsequently, a hybrid prediction index which was composed of a weighted sum of CV and kurtosis was proposed for predicting the impending arrhythmia before its actual occurrence. But several new ideas were implemented to overcome the potential problems of the previous work. The four possible problems of the previous work are listed as follows:

- ECG beat boundaries identification: the previous work used the automated time domain morphology and gradient (TDMG) algorithm, which is proposed by Mazomenos et al. (2012) to determine the boundaries of all ECG beats and analysed the phase space diagram based on a sliding window of 10 consecutive ECG beats. Example of 3 ECG beats can be seen in Fig.5.1. However, The TDMG algorithm

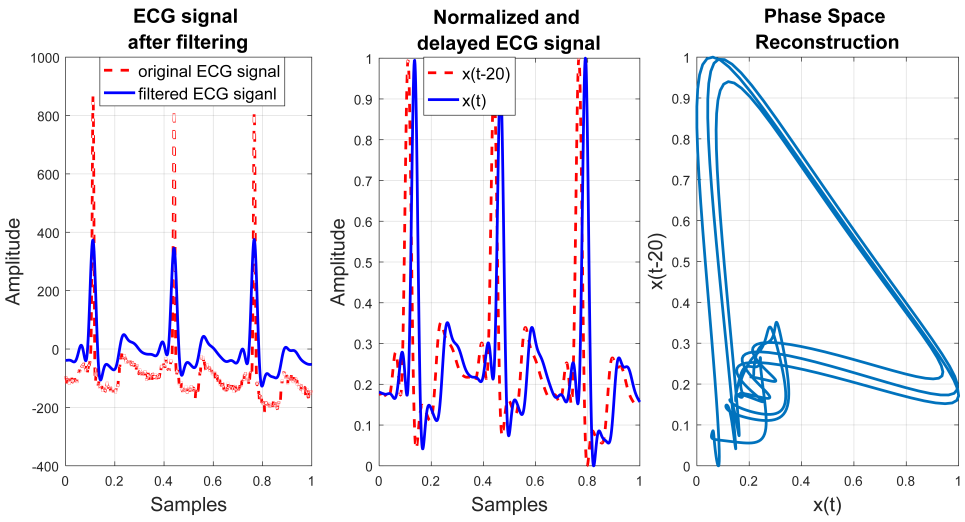

FIGURE 5.1: PSR from filtered and normalized delayed ECG signal

can only be applied for normal ECG beats (P-QRS-T), once ECG beats become abnormal such as irregular rhythmic pattern, tall sharp of T or P-waves, sudden changes in QRS morphology, small QRS complexes. It can not identify the boundaries of these abnormal ECG beats accurately. An incorrect window length of 10 successive ECG beats can lead to the unexpected trajectories in the phase-space and the wrong number of the black boxes.

- Sample Interpolation: The previous work interpolated the CUDB signals to increase the sample frequency from 250 Hz to 1000 Hz that is same as the PTBDB signals in order to put them into a uniform platform. This requires them to add more artificial data, hence the information of the original CUDB signals may be distorted. The new CUDB signals may cause the incorrect result in the PSR and box-counting.

- Prediction time calculation: The prediction time of the previous work is calculated using the average heart rate where is under an ideal condition although the heart rate changes all the time for arrhythmia.

- There is another problem from the previous work that may cause the spurious result of the PSR plot. As can be seen, on the top of Fig.5.2, there is an example of a window with 5 consecutive ECG beats of $CU15m$ record from CUDB. The red and green time window represent two successive windows of 4 consecutive ECG beats. After the normalization of these two windows, it is observed that the ECG data of the next window contain ECG peaks with relatively high or low amplitude, which can be considered as a VPB. The amplitude of the overlapped ECG beats between the first window and the next window reduces after normalization. From the normalization formula (5.1), the larger difference between x_{max} and x_{min} can lead to relatively small $\widetilde{x}(t)$. Hence a premature beat can cause the other normal

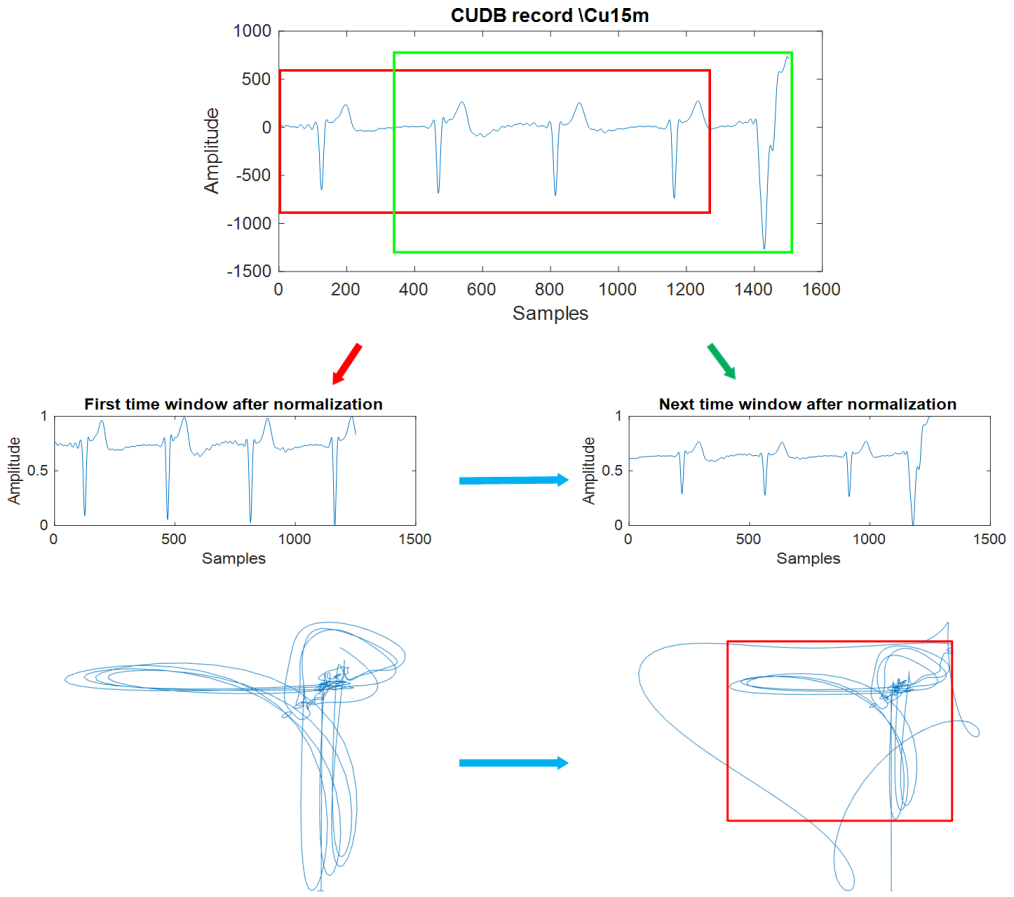

FIGURE 5.2: The PSR problem of normalization in ECG windows

beats to shrink in the same window. Furthermore, the bottom of Fig.5.2 are the corresponding PSR plots of two windows. From the second PSR graph, the main body (red frame) becomes narrow if we compare with the former, the results show the number of the black boxes of the second PSR plot is less than the first one. However, the actual situation should be opposite, since a premature beat can lead to a large trajectory in the phase-space, which should generate more black boxes than the normal trajectory.

$$\widetilde{x}(t) = (x(t) - x_{min}) / (x_{max} - x_{min}) \tag{5.1}$$

In our work, in order to overcome the first three problems, we plotted the phase-space diagram based on a sliding window of fixed length rather than 10 consecutive ECG beats. Moreover, we used Interquartile range (IQR) technique to find the outliers in order to remove the ECG signal with relatively high or low amplitude to solve the fourth problem. The following part will give the theoretical background of the key methods used in our work.

5.2.1 PSR of Arrhythmia

Normally the phase space of a system of fixed frequency oscillations within a limit cycle would be a closed contour, however, the trajectory will start to spread in a chaotic system thereby filling the phase space Cappiello et al. (2014). In the healthy heart condition, within a small time window, the consecutive ECG beats can be considered as an almost quasi-periodic waveform Chakraborty et al. (2017). Therefore, the phase-space analysis of it would produce an almost closed contour Fojt and Holcik (1998). However, during arrhythmia episode, the system is disrupted since the heart rhythm becomes chaotic, leading to an incoherent phase relationship between heart electrical activities Cappiello et al. (2014). In this case, PSR method might be a good choice for arrhythmia analysis, since it can present the phase space of ECG signals that can help us identify the phase relationship of electrical activities from different parts of the heart. The phase-space of the normal ECG signal within a small time-window can be plotted as a closed contour and such closed contour might be distributed in the presence of desynchronization of the heart Cappiello et al. (2014). This feature may help us to distinguish the normal and abnormal heart beats.

5.2.2 Data standardization and IQR application

IQR is an important measurement in statistics, which is defined by the difference between upper and lower quartiles. In general, it is used to build graphical representations of a probability distribution and equals to the difference between 25^{th} and 75^{th} percentiles (middle 50%). IQR was widely used to identify outliers Walfish (2006); Schwertman et al. (2004). They introduced the upper and lower bounds can be set based on the 1.5× IQR, any observation outside these fences is considered as a potential outlier. The most significant advantage of the IQR is that it depends on the median rather than the mean of the data, hence it also works for such ECG data that are not normally distributed.

In this work, we first apply standardization for ECG signal processing as seen in Fig.5.3**a**. Then we determine the probability distribution of an ECG record based on their amplitude after standardization and find the median value from the data. After that, we try to determine the IQR by calculating the probabilities forward and backward the median value until they reach to 25% respectively. However, it is a discrete system, the probabilities can not reach to 25% exactly. Therefore, our algorithm stops to calculate once the probabilities are larger than 25% and marks the stop points as Q_1 and Q_3 respectively. The difference between Q_1 and Q_3 is defined as IQR. Because the probability distribution of an ECG record is wider than the normal distribution, the upper and lower fences should be wider than the normal case. We used 3× IQR to replace 1.5× IQR based on our experimental results. In order to guarantee most of the ECG

data are in these fences. As can be seen in Fig.5.3**b**.

As mentioned above, The normalized ECG data can get distorted if there exist some ECG beats with relatively high or low amplitude, such as artefacts or VPBs. Since the whole phase portraits gets squeezed in a smaller region and leads to spurious result of the number of the black boxes (See Fig.5.4**a**) if we can fix relatively large upper and lower limit after applying standardization instead of the normalization by using formula (5.2), that may solve this problem Das and Maharatna (2014). The results show our method can effectively overcome the fourth problem of the previous work. The PSR diagram after standardization and IQR technique can be seen in Fig.5.4**b**. It keeps all phase portraits in the same region as shown in the red frames (the dotted red line). Although, the phase portraits can not contain the ECG samples outside the upper and lower bounds, these samples are just a very small part and can not influence the results.

$$\widetilde{x}\left(t\right) = \left(x\left(t\right) - \text{mean}(x)\right) / \text{std}(x) \tag{5.2}$$

5.2.3 FCM clustering

The FCM clustering is one type of unsupervised machine learning algorithm involves assigning all objects to different clusters, while objects belonging to the same cluster are as similar as possible. This technique has been applied recently for cardiac color ultrasound analysis Dongdong et al. (2019), arrhythmia classification and detection Haldar et al. (2017); Roopa et al. (2018) and detection of Premature Ventricular Contractions (PVCs) Gharieb et al. (2016). FCM clustering technique is normally applied in which each object may belong to more than one cluster. This is particularly important in our work, the subjects from VT followed by VF group contain the features from both VT and VF conditions and they possibly belong to more than one group. Hence it is important to use Fuzzy C-means clustering to identify such subjects.

The FCM clustering is achieved based on the minimization of the objective function in (5.3),

$$FCM_m = \sum_{i=1}^{D}\sum_{j=1}^{N} \mu_{ij}^{m} \left\| x_i - c_j \right\|^2 \tag{5.3}$$

where D is the number of objects and N is the number of clusters, m is the degree of fuzzy overlap, x_i and c_j represent the i^{th} object and the center of the j^{th} cluster respectively, μ_{ij} is the degree of membership of object x_i in the j^{th} cluster. Initially,

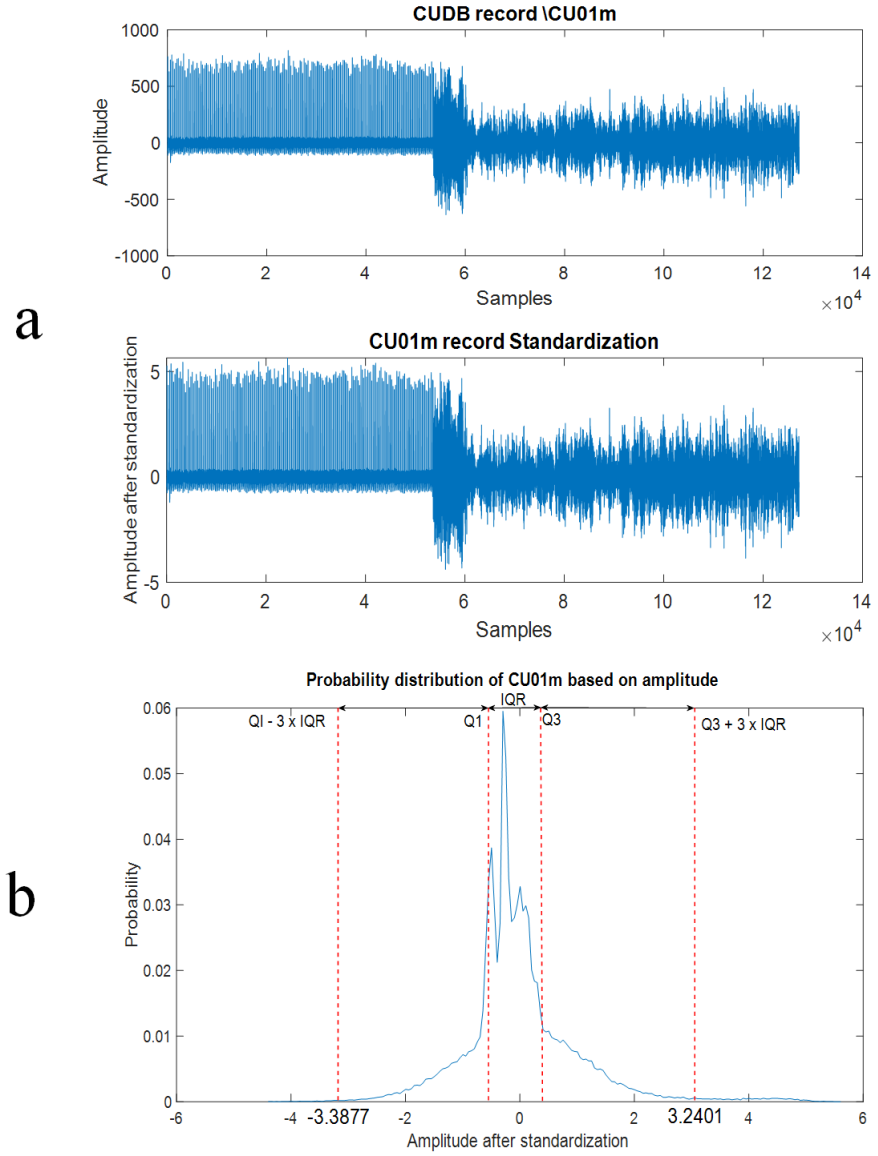

FIGURE 5.3: ECG data standardization and outlier identification ($CU01m$). **a**, ECG data standardization. **b**, Outlier identification of ECG data, the data smaller than -3.3877 or larger than 3.2401 will be removed

the degree of cluster membership μ_{ij} is set randomly, then the c_j and updated μ_{ij} are calculated by using formulas (5.4) and (5.5) respectively.

$$c_j = \frac{\sum_{i=1}^{D} \mu_{ij}^m x_i}{\sum_{i=1}^{D} \mu_{ij}^m}, \tag{5.4}$$

$$\mu_{ij}^m = \frac{1}{\sum_{k=1}^{D} (\frac{\|x_i - c_j\|}{\|x_i - c_k\|})^{\frac{2}{m-1}}} \tag{5.5}$$

In our work, the number of objects D is 32, which is the number of the VA records we used. The number of clusters is 4 because the number of types of VA is 4 (VA

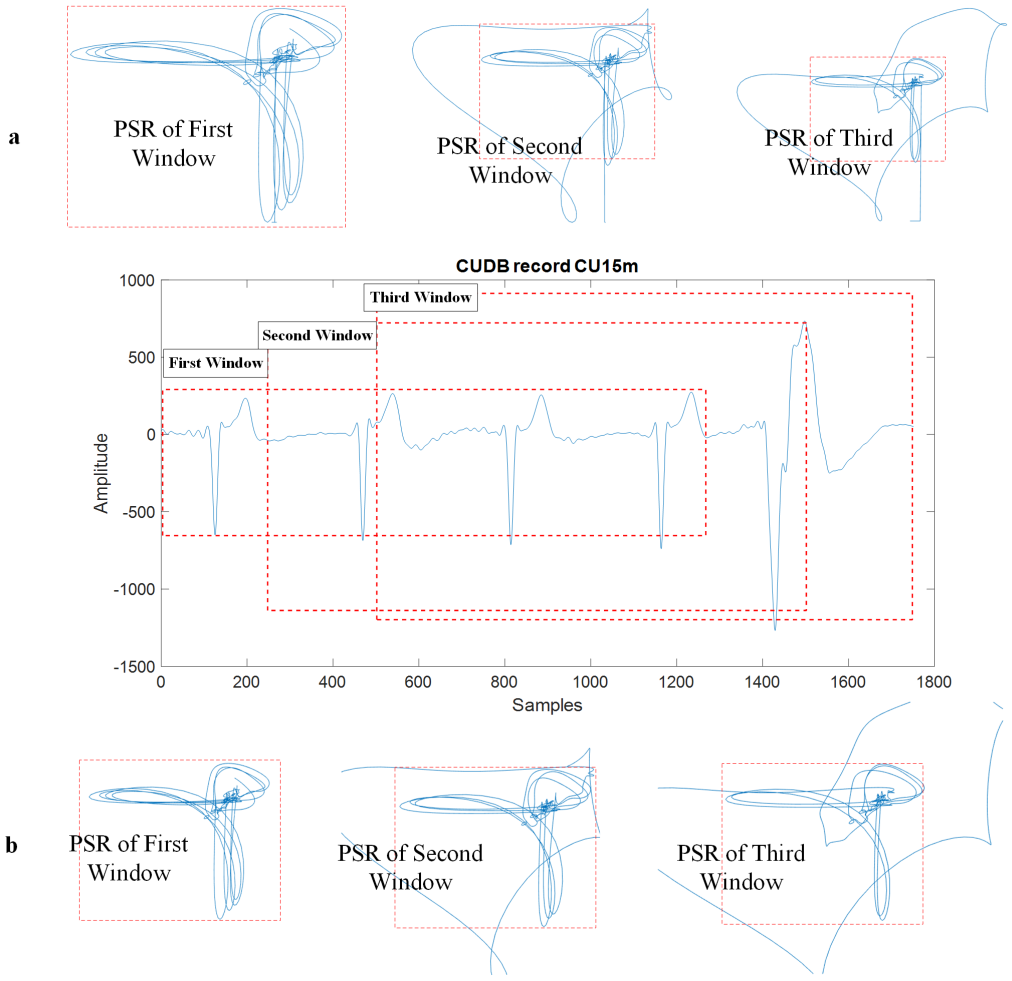

FIGURE 5.4: Problem of PSR plot based on data normalization and solution. **a**, PSR plot after data normalization. **b**, PSR plot after using data standardization and IQR. (The dotted red lines in **a** and **b** mean the main body of PSR for each window)

without VPBs, VT, VF and VT followed by VF). All objects x are firstly located in the coordinate system based on the calculated values of the x-axis and y-axis. For each object x_i $(i = 1, 2, ..32)$, the center of each cluster c_j $(j = 1, 2, ..4)$ will be calculated using (5.4) based on a random cluster membership μ_{ij}. Then, repeating to calculate the c_j with updated μ_{ij} and objective function FCM_m until the FCM_m improves by less than a minimum threshold or after a maximum number of iterations. The sum of the cluster membership values μ_{ij} should be 1, where lower value represents the object is unlikely to belong to this cluster, higher value means the object is more likely member of this cluster. The detailed description will be given in Section 5.3.2.

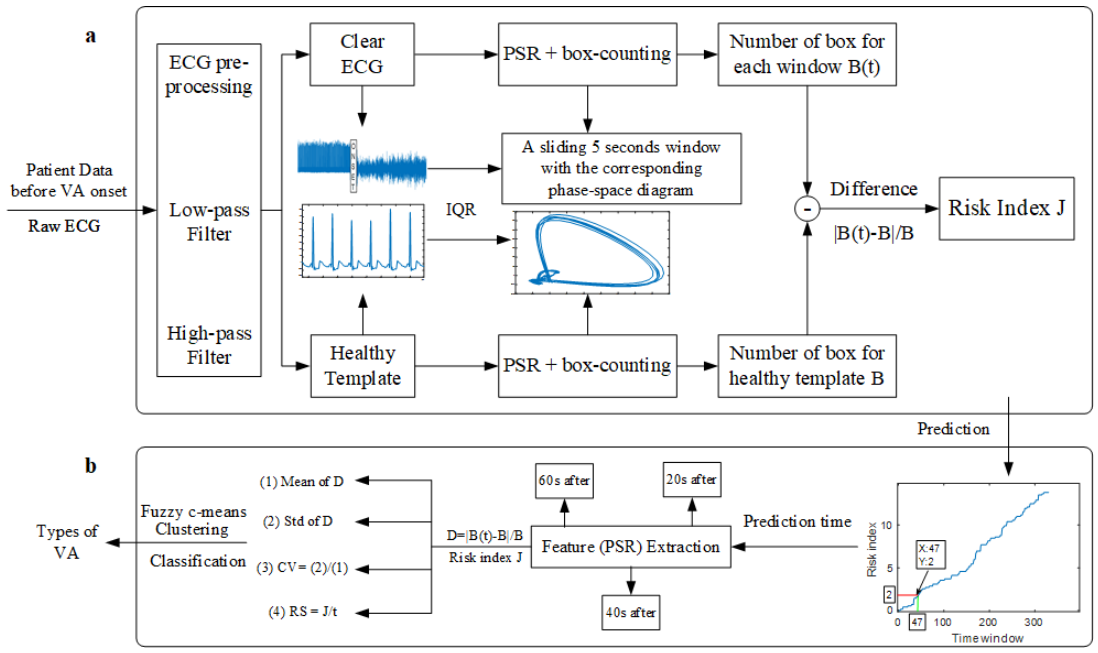

FIGURE 5.5: System overview of VA prediction and classification. **a**, Prediction of VA using PSR and box-counting. **b**, Classification of VA based on PSR features using fuzzy clustering technique.

5.3 Methodology

The block diagram of the proposed system for VA prediction and classification has been shown in Fig.5.5. The prediction system consists of four stages in Fig.5.5**a**. The first stage includes fourth order Butterworth high-pass filter and low-pass filter with cut-off frequency of 1 Hz and 30 Hz respectively to remove ECG noise and baseline wandering Amann et al. (2005). In the second stage, the phase space diagram of an ECG healthy template and its corresponding number of black boxes are determined using PSR and box-counting techniques. The number of black boxes for the healthy template was used as the healthy standard. In our work, the time delay for PSR is 20 samples and the value of N for box-counting is 2^{10}, which are the same as the previous work Cappiello et al. (2014); Koulaouzidis et al. (2015); Vemishetty et al. (2019). After that, we built a sliding window of 5 seconds of ECG signals with 4 seconds overlap for the ECG segment that precedes the onset of VA condition and applied PSR and box-counting technique to determine the number of black boxes for each time window. Finally, the risk index J is calculated based on the difference of the number of black boxes between each sliding time window and the healthy template.

For classification system in Fig.5.5**b**, it includes two main steps. Firstly, once the risk index reaches the threshold (which will be discussed in the following section), we extract features based on the number of black boxes and risk index during next few seconds. Secondly, the FCM clustering technique is used to classify four different types of VA.

5.3.1 Formulation of the prediction index for impending VA

First, the mean of the number of the black boxes from the healthy template (B_{mean}) for each individual ECG record is calculated. Then we developed J based on this value to predict VA. We obtained the number of the black boxes for all consecutive 5 seconds of time windows with 4 seconds overlap before the VA ($B(t)$). They were divided into four categories based on the difference between $B(t)$ and B_{mean}, which are normal situation and three abnormal situations. We found for most of the healthy subjects, the difference between B_{mean} and all $B(t)$ are less than 10% of B_{mean}. Therefore, we decided to use 10% as a threshold to distinguish normal and abnormal situations. Here, if the difference between $B(t)$ and B_{mean} is less than 10% of B_{mean}, the ECG signals in this time window will be considered as a normal case. For abnormal situations, there are three different levels when the difference between $B(t)$ and B_{mean} is larger than 10% of B_{mean}, which are 10% to 15%; 15% to 20% and larger than 20% respectively. And the J is generated based on these situations, which is formulated as (5.6).

$$J(t) = \begin{cases} X(t) & t = 1, \\ J(t-1) + X(t) & 1 < t < n, \end{cases} \tag{5.6}$$

where n is the number of the time window. $X(t)$ is the index value of the t^{th} time window, which can be divided into five different situations as shown in (5.7).

$$X(t) = \begin{cases} 0 & \left|\frac{B(t)-B_{mean}}{B_{mean}}\right| \leq 10\%, \\ w_1 & 10\% < \left|\frac{B(t)-B_{mean}}{B_{mean}}\right| \leq 15\%, \\ w_2 & 15\% < \left|\frac{B(t)-B_{mean}}{B_{mean}}\right| \leq 20\%, \\ w_3 & 20\% < \left|\frac{B(t)-B_{mean}}{B_{mean}}\right|, \\ -0.1 & \left|\frac{B(t)-B_{mean}}{B_{mean}}\right| \leq 5\%, Condition_1,. \end{cases} \tag{5.7}$$

Here, $B(t)$ is the number of the black boxes in the t^{th} time window and B_{mean} is the mean of the number of black boxes for the healthy template. In addition, if the difference between $B(t)$ and B_{mean} is less than 10%, that time window is considered as a normal situation and the index value $X(t)$ is 0. Among three abnormal situations, w_1, w_2 and w_3 represent the index value of the t^{th} time window when the $\left|\frac{B(t)-B_{mean}}{B_{mean}}\right|$ are between 10% and 15%, between 15% and 20% and larger than 20% respectively. In this case, w_1, w_2 and w_3 are the weighting factors and their sum should be 1 Cappiello et al. (2014). The weighting factors determine the contributions of these three abnormal situations towards the final risk index J for impending VA and the larger $\left|\frac{B(t)-B_{mean}}{B_{mean}}\right|$ should lead to a larger weighting factor. In our work, we chose three different combinations of w_1, w_2 and w_3 with (0.6,0.25,0.15); (0.5,0.3,0.2) and (0.4,0.35,0.25) and finally chose 0.5, 0.3 and 0.2 as the w_1, w_2 and w_3 respectively since this combination gave us the most

TABLE 5.1: The average values of J in each group based on three different combinations of weight

	The combination of weight to calculate J		
	(0.6,0.25,0.15)	(0.5,0.3,0.2)	(0.4,0.35,0.25)
Healthy	0.1688	0.1375	0.1425
VA without VPBs	4.525	4.875	4.675
VA with VPBs	38.57	46.18	41.82

obvious difference of J between three groups (healthy, VA without VPBs and VA with VPBs), which is shown in Table 5.1. In order to avoid the situation of progressively increasing of J, we have set a condition ($condition_1$ in 5.7) to reduce it.. This condition should be stricter than the condition of normal window. Therefore, we set 5% as a threshold to signify the completely normal ECG, leading to the reduction of J index. In this case, if the values of $\left|\frac{B(t)-B_{mean}}{B_{mean}}\right|$ in 10 successive time windows are lower than 5%, the trend of ECG is considered to become completely normal. In this case, J reduces 0.1 and the minimum value of J is 0.

5.3.2 Classification of VA

Once the risk index reaches to the threshold, it is considered as an omen of impending VA. In order to understand the regularity of continuous ECG time windows after the prediction time and classify the VA before its onset, we have extracted the ECG PSR features during the next 20, 40 and 60 seconds and compared the performance based on the corresponding accuracy. These features are extracted based on the $\left|\frac{B(t)-B_{mean}}{B_{mean}}\right|$ and risk index J by calculating the mean (μ), standard deviation (σ), coefficient variation (CV) and rising speed (RS) as in equation (5.8)

$$\begin{cases} \mu = mean(\left|\frac{B(t)-B_{mean}}{B_{mean}}\right|), CV = \sigma/\mu, \\ \sigma = \sqrt{(\left|\frac{B(t)-B_{mean}}{B_{mean}}\right| - \mu)^2}, RS = J/t. \end{cases} \tag{5.8}$$

All subjects from four different classes are assigned into four clusters by using FCM clustering. All subjects are displaced into a two-dimension co-ordinate system with their RS - (X axes) and CV - (Y axes). The degrees of membership of each subject for four clusters are calculated based on the distance between itself and the centre of each cluster. Finally, the cluster with the highest degree of membership is recognised as the

group of the corresponding subject. In this case, the number of the cluster N is 4 since we have four different types of VA and degree of fuzzy overlap m is generally chosen as 2 Kesemen et al. (2016). We also identify the subjects that their highest cluster membership value is smaller than 0.6 as the fuzzy overlaps, since these subjects possibly belong to more than two clusters. The whole operation will stop once the number of iterations reaches a maximum of 20 or the improvement of the objective function is less than 0.001 between the final two iterations.

5.4 Results and discussion

5.4.1 ECG data description

The proposed system was evaluated using the publicly available ECG databases from Physionet Goldberger et al. (2000). 32 subjects both from PTBDB Bousseljot et al. (1995) and CUDB Nolle et al. (1986) were used in order to analyse in both healthy and arrhythmic ECG databases respectively. Here, we only used 32 subjects in CUDB, since other 3 records from CUDB $CU21m$, $CU33m$ and $CU35m$ have large amount of artefacts before the VA onset, hence it is difficult to extract features for VA prediction. For these arrhythmic subjects, we analysed the ECG segment that precedes the onset of the VA condition as shown in Fig.5.6. The ECG signals after the VA onset are not used in our work.

5.4.2 Prediction of VA

Among 32 healthy subjects in PTBDB, the maximum value J attained was 1.4 with its value for most of the subjects (22 subjects) remaining at 0 and others in Fig.5.7.(**a**). The 32 arrhythmic subjects from the CUDB were divided into four groups, which are VA without VPBs, VT, VF and VT followed by VF. The values of J based on the three different combinations of weighting factor are shown in Fig.5.7.(**b**). The combination of the weighting factors w_1, w_2 and w_3 (refer to the methodology section) with 0.5, 0.3 and 0.2 respectively gave us the most obvious difference of J between three groups (healthy, VA without VPBs and VA with VPBs). Hence, we chose this combination to calculate J. In this case, the choice of the template becomes an important task in our work, since different templates may lead to a different value of risk index J. Here, the comparison of J between healthy subjects in PTBDB and arrhythmic subjects in CUDB is done based on three different templates - in essence three 5s segments are taken from the healthy part of ECG in subject-specific way - as shown in Table 5.2. It shows the risk index J for most of healthy subjects in PTBDB are 0 and the highest value of all healthy subjects is 1.4 while, the lowest value of J for all arrhythmic subjects (except $CU30m$) in CUDB are greater than 2. Here, the information of subject $CU30m$

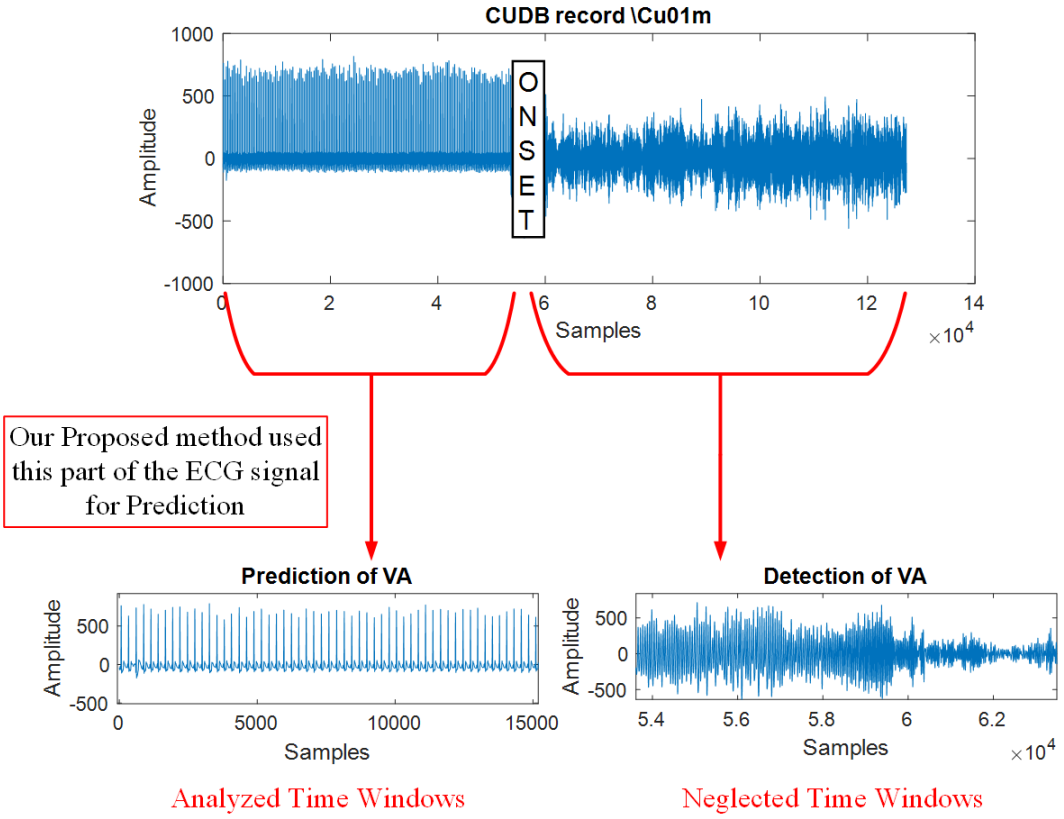

FIGURE 5.6: Prediction VA based on the ECG analysis before the VA onset

is not available, since there are insufficient ECG data before VA onset to calculate the risk index. Therefore according to our analysis the condition $J > 2$, might signify an impending VA. Another interesting point to note is that for the VA without VPBs group ($CU01m$, $CU06m$, $CU07m$, $CU28m$), J is relatively lower than the other three groups. This is due to the fact that immediately after the occurrence of a VPB, the value of J increases significantly.

5.4.3 Classification of VA

The classification of VA is achieved based on the PSR features using FCM clustering technique. We extracted the ECG PSR features during the 20, 40 and 60 seconds after the prediction time point for each subject in order to evaluate the accuracy of the classifier employed accuracy and classification time before the VA onset. The Average values of CV and RS of J for four types of VA was calculated using (5.8) with 95% confidence interval as shown in Table 5.3. It is apparent that there are significant variation in terms of CV and RS for the four different types of VA and therefore these parameters were used for the classification purpose. The performance of VA classification using FCM clustering are shown in Fig.5.8**a**, and their average classification time before VA onset and the corresponding accuracy are shown in Fig.5.8**b(1)**. The result based

TABLE 5.2: The highest risk index J for both healthy and arrhythmic subjects in PTBDB and CUDB based on different templates (N/A: not available)

Class of Database	Patient ID in PTBDB	Highest risk index value based on the different templates				Class of Database	Patient ID in CUDB	Highest risk index value based on the different templates			
		Tmpl 1	Tmpl2	Tmpl 3	Average			Tmpl 1	Tmpl 2	Tmpl 3	Average
Healthy Subjects	PTB105	0	0.2	0	0.07	VA without VPBs	CU01m	6.8	5.1	6.5	6.13
	PTB116	0.2	0.4	0	0.2		CU06m	3.3	2.9	3.7	3.30
	PTB117	0	0.4	0	0.13		CU07m	4.4	4.7	6.6	5.23
	PTB122	0	0	0	0		CU28m	5	3.1	4.6	4.23
	PTB155	0	0	0	0		CU30m	N/A	N/A	N/A	N/A
	PTB156	0	0	0	0	VF	CU08m	102.7	112.8	184.4	133.3
	PTB166	0	0	0	0		CU11m	154.3	145.9	138.7	146.30
	PTB170	0	0	0	0		CU22m	113.1	117.9	112.7	114.57
	PTB180	0	0	0	0		CU23m	124.2	131.9	109.7	121.93
	PTB182	0	0	0	0	VT	CU02m	33	52.4	53.4	46.27
	PTB185	0.2	0.2	0	0.13		CU04m	10.9	14.2	11.4	12.17
	PTB198	0.2	0.6	0.2	0.33		CU05m	20.2	33.7	20.1	24.67
	PTB214	0.8	0.8	0.2	0.6		CU13m	16.2	27	15.4	19.53
	PTB229	0	0	0	0.07		CU16m	23.1	14.6	13.6	17.10
	PTB233	1.4	0.7	0.7	0.93		CU17m	11	12.3	13.9	12.40
	PTB235	0	0	0	0		CU20m	59.2	40.3	42.8	47.43
	PTB236	0	0.2	0	0.07		CU25m	15.9	28.9	13.8	19.53
	PTB237	0	0	0	0		CU26m	17.3	16.4	15.4	16.37
	PTB238	0	0.2	0	0.07		CU27m	34.1	39.6	33.3	35.67
	PTB240	0	0	0	0		CU31m	36.1	39.5	44.4	40.00
	PTB242	0.2	0.2	0.8	0.4		CU32m	14	13.8	9.3	12.37
	PTB244	0	0	0	0		CU34m	48.2	47.1	38.6	44.63
	PTB246	0	0.8	0.2	0.33	VT followed by VF	CU03m	34.4	30.8	53.4	39.53
	PTB247	0	0	0	0		CU09m	21.8	25.2	22.5	23.17
	PTB248	0.2	0.6	0.2	0.33		CU10m	95.5	72.6	85.9	84.67
	PTB251	0	0	0	0		CU12m	18.6	22.6	34	25.07
	PTB252	0.6	0.6	0.4	0.53		CU14m	61.8	67.6	60.5	63.30
	PTB155	0	0	0	0		CU15m	16.4	15.7	14.6	15.57
	PTB260	0	0.4	0.2	0.2		CU18m	16.4	18.4	37.7	24.17
	PTB263	0.2	0.4	1	0.53		CU19m	39.9	36.3	37.7	37.97
	PTB264	0.2	0.2	0.9	0.43		CU24m	28.1	28.4	30.5	29.00
	PTB266	0	0.2	1	0.4		CU29m	80.4	72.6	85.9	79.63

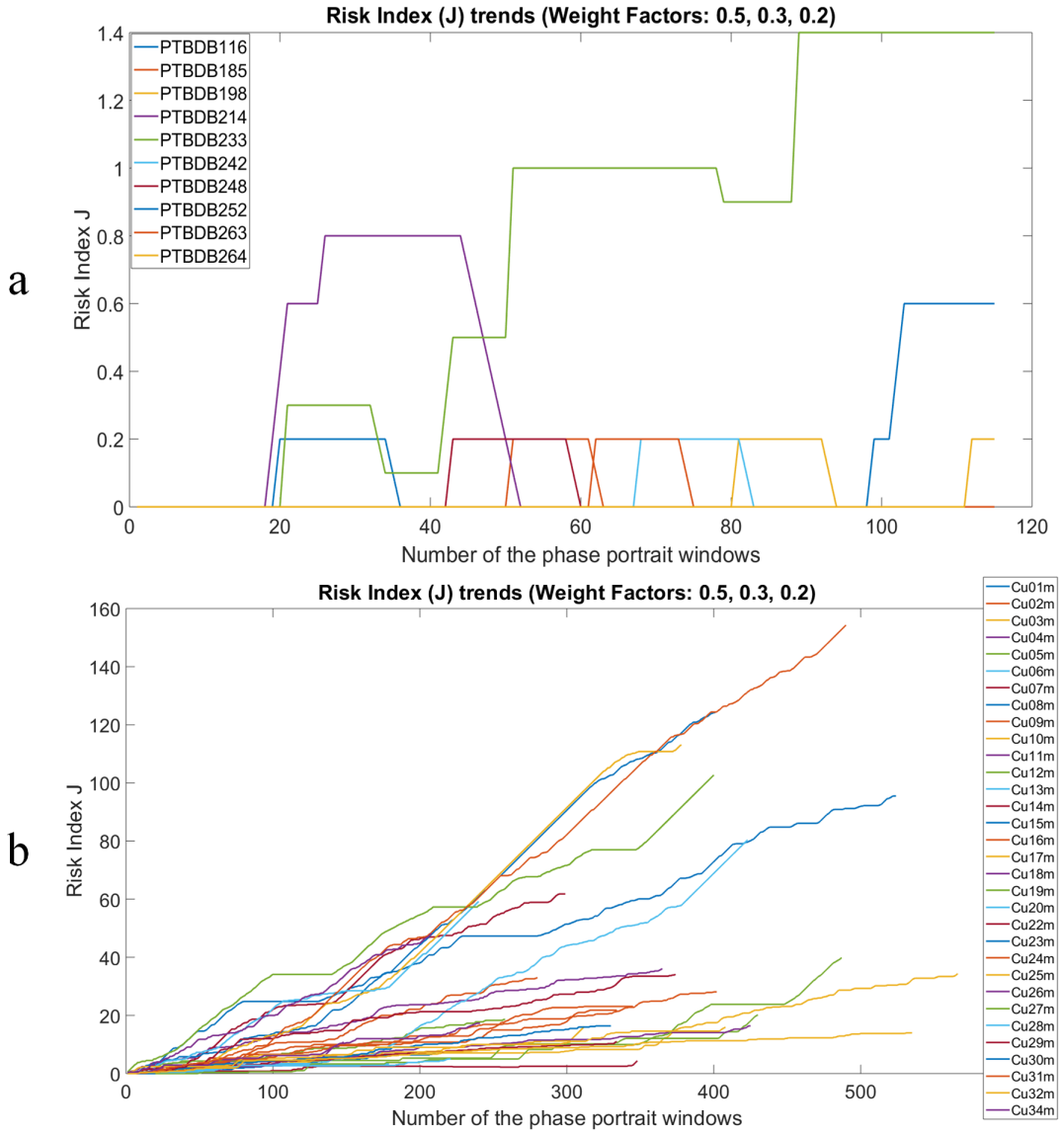

FIGURE 5.7: The risk index J trends. **a**, Results of 10 healthy subjects in PTBDB. **b** Results of 32 arrhythmic subjects in CUDB.

on 20s and 40s PSR features after prediction time point shows the same accuracy of 93.5% with two and one fuzzy overlap respectively. The best result was obtained using 60s PSR features after prediction time point with 96.8% accuracy and no fuzzy overlap. Hence we have selected to use the features during 60s after the prediction time for each subject. Moreover, we applied confusion matrix and Receiver Operator Characteristic (ROC) curve to evaluate our classification results. Fig.5.8**b(2)** and Fig.5.8**b(3)** show the confusion matrix and ROC of VA classification.

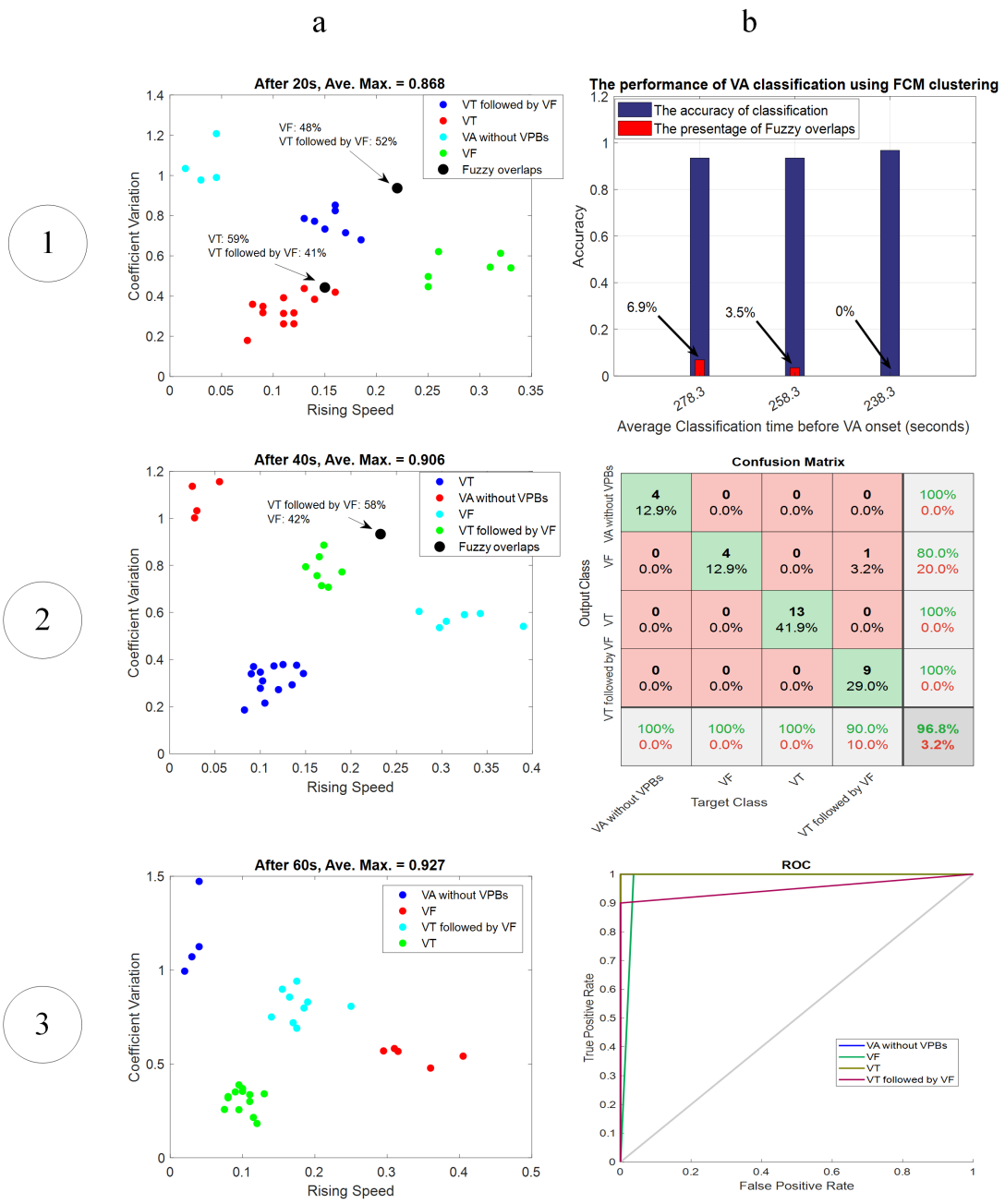

FIGURE 5.8: The classification results. **a**, Results of FCM clustering based on **(1)**20s, **(2)**40s and **(3)**60s. PSR featurwes after the prediction time. **b(1)**,The performance of VA classification with average classification time before VA onset. **b(2)**,The confusion matrix of VA classification. **b(3)**,The ROC of VA classification

TABLE 5.3: The feature extraction of all subjects based on CV and RS

Parameters	VA without VPBs	VF	VT	VT followed by VF
Average CV	1.100	0.549	0.321	0.761
Average RS	0.034	0.329	0.109	0.191
CV interval (95% CI)	(0.99, 1.21)	(0.48, 0.59)	(0.19 ,0.44)	(0.54, 0.94)
RS interval (95% CI)	(0.02, 0.04)	(0.29, 0.39)	(0.08, 0.15)	(0.14, 0.29)

5.4.4 Method evaluation

For prediction of VA, we evaluate our method by computing the prediction time - defined as the time point where $J > 2$ - for each arrhythmic subject in CUDB and compare the results to the previous works Cappiello et al. (2014) which is shown in Table 5.4. The average prediction time for all subjects is 4.97 mins, which is 50 seconds earlier than the previous work Cappiello et al. (2014), with the best and the worst case prediction time being 8.68 mins ($CU03m$) and 1.78 mins ($CU06m$) respectively. Our results show that the prediction time for different subject is different since it is relative to the length of the analysed ECG data before the VA onset. Here, we provided the correlation between the length of the healthy ECG data before the VA onset (analysis time) and the corresponding prediction time for each of the subjects in Fig.5.9. It shows that all the data points can be fitted around a straight line with the correlation coefficient $R = 0.952$. This result clearly shows that there is a strong positive linear relationship between the prediction times and the length of the data that was available for analysis before the VA onset. Hence it implies that if we can have longer length of analysis data before VA onset, the performance of our prediction method will be even better; a scenario that can be satisfied for long-term ECG monitoring either by conventional ECG systems at the hospitals or through wearable ECG sensors in a nomadic environment.

In addition, in order to evaluate the performance of VA prediction, we used a leave one out cross-validation (LOOCV) method to calculate the true positive (TP), true negative (TN), false positive (FP) and false negative (FN) with positive P (VA subjects) and negative N (Healthy subjects). Here, we derived the prediction performance based on sensitivity (SE), specificity (SP), accuracy (ACC), positive predictive value (PPV), negative predictive value (NPV), false positive rate (FPR), false discovery rate (FDR), false negative rate (FNR) and F_1 score using the following formulas in (5.9). The Table 5.5 depicts the comparison of prediction measures between the previous work Cappiello et al. (2014) and our work using LOOCV approach which shows that with the proposed risk index J, we obtained 100% SE, ACC, NPV and F_1 score, which are better than the previous work Cappiello et al. (2014).

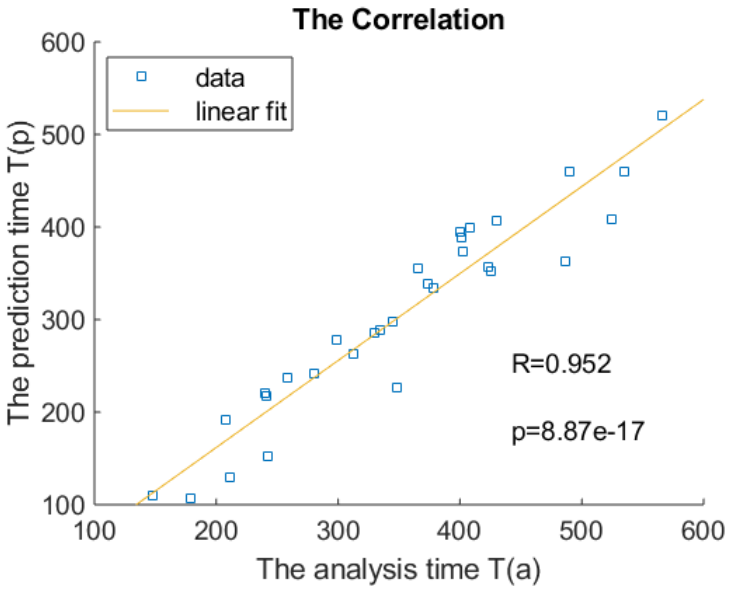

FIGURE 5.9: The correlation between the length of the analysed ECG data before VA onset T(a) and prediction time before VA onset T(p)

$$\begin{cases} \text{SE} = \text{TP/P} = \text{TP}/(\text{TP} + \text{FN}), \text{SP} = \text{TN/P} = \text{TN}/(\text{FP} + \text{FN}), \\ \text{ACC} = (\text{TP} + \text{TN})/(\text{P} + \text{N}), \text{PPV} = \text{TP}/(\text{TP} + \text{FP}), \\ \text{NPV} = \text{TN}/(\text{TN} + \text{FN}), \text{FPR} = \text{FP/N} = \text{FP}/(\text{FP} + \text{TN}), \\ \text{FDR} = \text{FP}/(\text{FP} + \text{TP}) = 1 - \text{PPV}, \text{FNR} = \text{FN}/(\text{FN} + \text{TP}), \\ \text{F}_1\text{score} = 2\text{TP}/(2\text{TP} + \text{FP} + \text{FN}). \end{cases} \tag{5.9}$$

In addition, the classification measures of each type of VA are calculated using (5.9) and the results are shown in Table 5.6. Our methodology achieved an average sensitivity, specificity and accuracy of 97.5%, 99.1% and 98.4% respectively for VA classification. Among 31 subjects (except $CU30m$), only one of VT followed by VF group was recognised as VF group. However, since subject from VT followed by VF group finally goes to the VF condition, it is logical to be considered as VF group in which case the classification performance goes to 100%. We also compared our technique to other previously established algorithms that were mentioned in the literature. The comparison results are given in Table 5.7. It is evident that our proposed method has comparable or better performance than the previous methods for VA classification with the added advantage that here the classification is possible even before the event actually occurs.

5.5 Concluding Remarks

This Chapter proposed an algorithm for prediction and classification of fatal VA using PSR and fuzzy c-means clustering techniques. The number of black boxes based on

TABLE 5.4: The comparison of prediction time between the previous work and our work (N/A: not available)(Prediction time: The time length between prediction time point and VA onset)

Class of Database	Patient ID in CUDB	Time before VA onset (s)	Prediction time of Cappiello et al. (2014) (s)	Prediction time of our work (s)
VA without VPBs	CU01m	211	34.3	130
	CU06m	179	21.9	107
	CU07m	348	195.1	227
	CU28m	221	97.2	152
	CU30m	N/A	14.6	N/A
VF	CU08m	524	135.7	408
	CU11m	490	359.3	460
	CU22m	378	336.7	334
	CU23m	401	323.3	389
VT	CU02m	280	172	242
	CU04m	148	107.5	110
	CU05m	430	358.7	407
	CU13m	312	343.4	263
	CU16m	345	222.2	297
	CU17m	334	520.5	289
	CU20m	240	197.5	220
	CU25m	408	360.8	399
	CU26m	241	70.1	217
	CU27m	400	213	395
	CU31m	365	250.8	355
	CU32m	535	381.6	460
	CU34m	208	122.3	192
VT followed by VF	CU03m	566	413.5	521
	CU09m	334	214.4	288
	CU10m	423	294.4	357
	CU12m	258	200	237
	CU14m	299	242	278
	CU15m	401	323.2	389
	CU18m	425	329.3	352
	CU19m	487	422.1	363
	CU24m	402	337.5	374
	CU29m	374	321.9	339
	Average	351.4	245.2	298.3

TABLE 5.5: The comparison of prediction performance between the previous work and our work under a LOOCV scheme

Prediction measures (%)	Cappiello et al. (2014)	Our work
Sensitivity (SE)	96.88	100
Specificity (SP)	100	100
Accuracy (ACC)	98.44	100
Positive predictive value (PPV)	100	100
Negative predictive value (NPV)	96.97	100
False positive rate (FPR)	0	0
False discovery rate (FDR)	0	0
False negative rate (FNR)	3.13	0
F_1 score	98.41	100

TABLE 5.6: The classification performance of our system for VA classification

Classification Measures (%)	VA without VPBs	VF	VT	VT followed by VF	Average
SE	100	100	100	90	97.5
SP	100	96.3	100	100	99.1
ACC	100	96.8	100	96.8	98.4
PPV	100	80	100	100	95
NPV	100	100	100	95.5	98.9
FPR	0	3.7	0	0	0.93
FDR	0	20	0	0	5
FNR	0	0	0	10	2.5
$F_{.1.}$ score	100	88.9	100	94.7	95.9

the trajectory of the ECG phase-space diagrams was calculated using the box-counting technique and the difference of the number of boxes between subject-specific normal ECG template and a sliding window of 5 seconds of the ECG signal is used to formulate a prediction risk index J. This index when tested on CUDB predicts an impending VA with an average prediction time of 298.3 seconds before the VA onset. Then we used fuzzy c-means clustering to classify four different types of VAs based on phase-space features. When tested on CUDB the proposed algorithm reached to an accuracy of 98.4%. However, we only used 64 ECG records to evaluate our proposed method as a proof-of-concept study. However, there are still many problems and limitations in our proposed algorithm. First, some parameters that were chosen in our work is based on our experimental results and hence are somewhat arbitrarily. For example, the parameters that were used in formulating the predicting index in section 5.3.1. Using 10% to distinguish normal and abnormal situations is relatively arbitrary. This probably can be solved by plotting the distribution of $\left|\frac{B(t)-B_{mean}}{B_{mean}}\right|$, and then determining some percentile (or else cross-validation) to set the parameter in the future. Second is the

TABLE 5.7: The comparison of classification performance of VA classification in other literature

Authors	Method Used	Classifier	Arrhythmia classes	Performance (%)
Li et al. (2013)	14 different features	SVM classifier	VF and VT	Acc: 96.3 SE: 98.4 SP: 98
Alonso-Atienza et al. (2013)	Time-frequency parameters	SVM classifier	Shockable (VF, VT) and non-shockable arrhythmias	Acc: 96 SE: 92 SP: 97
Balasundaram et al. (2013)	Wavelet anlysis features	Binary classifier	VT, OVF and DVF	Acc: 93.7
Roopaei et al. (2010)	Chaotic features	Thresholding	VF and VT	Acc: 88.6
Tripathy et al. (2016)	Entropy features	Random forest classifier	Shockable (VF, VT) and non-shockable arrhythmias	Acc: 97.23 SE: 96.54 SP: 97.97
Acharya et al. (2018)	Time segments	Convolution neural networks	Shockable (VF, VT) and non-shockable arrhythmias	Acc: 93.18 SE: 95.32 SP: 91.04
Mohanty et al. (2018)	Time-frequency features	C4.5 classifier	VF, VT and NSR	Acc: 97.02 SE: 90.97 SP: 97.86
Proposed method	Phase-space features	Fuzzy c-means clustering	VA without VPBs, VF, VT, and VT followed by VF	Acc: 98.4 SE: 97.5 SP: 99.1

feature scaling for Fuzzy C-means clustering method. In my work, it is lucky that the chosen features (CV and RS) were in a similar dynamic range. However, if the chosen features are in a dissimilar dynamic range, the cluster results will be completely different. In this case, the dimensions of the chosen features in a such distance-based scheme is important. Therefore, in order to avoid this situation, normalisation should be applied to keep all features in a same range. Third is the prediction is not an impending VA, but the database from which the record comes. As shown in Fig.5.9. It shows that there is a strong positive linear relationship between the prediction times and the length of the data that was available for analysis before the VA onset. However, what is more likely to be the case is that these arrhythmia patients are on the cusp of the J threshold because they are unwell. Then the prediction is always performed at the beginning of the record. In the future, I should apply our prediction and classification algorithms to the whole duration of each record in the MIT-BIH Arrhythmia and the MIT-BIH Normal Sinus Rhythm databases. Then, it is possible to characterise the temporal evolution of the J index and quantify the number of the false positive VA predictions and the classification performance. In addition, 3-dimension of phase space diagram can be further applied to extract more useful features of ECG to improve the prediction of VA Nandi et al. (2018). As a conclusion, the main feature of the proposed method is that for the first time it has been shown that it is not only possible to predict an impending VA sufficiently before its actual occurrence in time but also is possible to classify the type of VAs before it actually occurs (1 min after the prediction time point). We believe this is a novel result over existing approaches that can be used in clinical practice after rigorous clinical trial to advance technologies such as ICD or its sub-cutaneous version (S-ICD) that can help to preempt the occurrence of fatal VA - a main cause of Sudden Cardiac Death. However, apart from VA, there are other types of arrhythmias that could be precursors of other cardiac problems and therefore it is necessary to classify those as well. In the next chapter, we will develop a simple arrhythmia classifier based on PSR and box-counting techniques to classify more types of arrhythmias.

Chapter 6

An effective PSR-based Arrhythmia Classifier using Self-Similarity Analysis

6.1 Introduction

The most common types of arrhythmias leading to SCD are ventricular tachycardia (VT) and ventricular fibrillation (VF) Baldzizhar et al. (2016). These life-threatening arrhythmias normally require immediate treatment. However, there are several non-fatal arrhythmias like atrial fibrillation (AF), which may not require immediate treatment. Hence, the classification of arrhythmias is a vital task in cardiac arrhythmias diagnosis, which could be achieved by automatic classification method in the ECG analysis. Recently, various methods have been proposed for successful classification of ventricular arrhythmia (VA) or other non-fatal arrhythmias as discussed in Section 2.4.3.1. However, in clinical practice, early detecting of fatal arrhythmia requires a quick and accurate analysis of ECG signals. Hence, it is necessary to develop an arrhythmia classifier with low computational complexity and high accuracy. Besides, there is almost no literature that has taken a holistic view of the detection of transition process from VT to VF.

In this chapter, the main focus was to classify AF, VT, VF and VT followed by VF arrhythmias using phase space reconstruction (PSR) features that obtained from processed windows of ECG signals by taking inspiration from the previous work Roopaei et al. (2010). Two PSR diagrams were first plotted based on the same window length of 5 s filtered and normalized ECG signals with two different time delays. Then the PSR diagram was divided into several pixels and the features of PSR trajectories were extracted from two PSR diagrams using box-counting technique. Finally the classification model was trained by 50% of ECG windows from each ECG record based on these

features, remaining 50% ECG windows were used to evaluate our proposed algorithm.

The rest of this chapter is structured as follows. In next Section 6.2, we present the PSR diagrams with different time delays and different heart conditions. Then description of our algorithm is given in Section 6.3. Section 6.4 provides the results and discussion of the validation on four different databases. Finally, the conclusions are drawn in Section 6.5.

6.2 Theoretical Background

6.2.1 PSR diagram of different ECG windows

As mentioned in Section 4.2.3. One or more trajectories in the phase-space diagram pass through pixels are considered as black boxes (n_b) and others are white boxes (n_w). The number of (n_b) among all pixels can reflect the spread of these trajectories. The degree of complexity or chaotic dimension of a PSR diagram is defined as follows $d = n_b/((n_b+n_w))$ Amann et al. (2006). It suggested that if value of d is larger than a certain threshold d_0, the corresponding ECG is identified as VF. Following the exploration reported in Roopaei et al. (2010), the self-similarity of a PSR diagram of ECG signals can be determined by calculating the difference between the two achieved values of d based on two different time delay values. The following section will show the PSR diagrams of different types of ECGs with different time delay.

Many studies have shown the PSR of normal ECG is a regular pattern even if the time delay is different, such pattern could be different for different embedded delays Roopaei et al. (2010); Cappiello et al. (2014); Vemishetty et al. (2019). Roopaei et al. (2010) proposed a method based on self-similarity analysis of PSR diagram of ECG to classify VA. The results also showed that self similarity analysis of PSR diagrams with different time delay of 0.02 s and 0.08 s gave the highest performance to classify VT and VF. Thus, in our work, the self-similarity analysis of PSR is also based on the time delay of 0.02 s and 0.08 s. Following the exploration of our experiment, we summarized three different types of PSR diagrams of normal ECG as shown in Fig.6.1. The top three figures are the PSR diagrams of normal ECG when the time delay is 0.02 s. These PSR diagrams are closed contours and we called them type O. The bottom three figures are the PSR diagrams of the same normal ECG with 0.08 s time delay. The PSR diagram looks like a cross and we named them type X. After the analysis of all 122 records from 4 different databases (MIT-BIH AFDB, PTBDB, CUDB and UHSF). We found if the time delay of PSR is larger than 0.05 s, the PSR diagram of normal ECGs tends to type X, otherwise, it goes to type O.

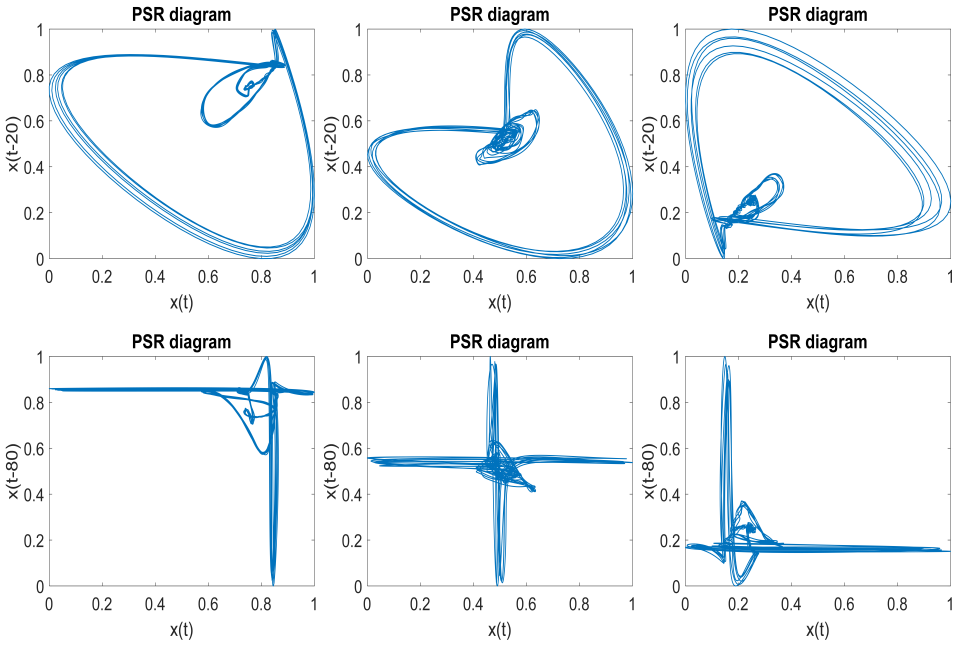

FIGURE 6.1: Three different types of the PSR diagrams of normal ECG. (Top: 0.02s time delay; Bottom: 0.08s time delay)

In PSR diagram of normal ECG, the small closed contours are P and T waves, and the spread trajectories represent R waves Hou et al. (2018). For the PSR diagram of AF, the shape is generally similar with the PSR diagram of normal ECG. Because AF and normal ECG both have QRS waves, which can be seen by naked eyes. The main difference of PSR diagram between AF and normal ECG is the part that represents P and T waves. As shown in Fig.6.2, this part (red window) is more chaotic in AF (right) than it is in a normal ECG (left).

Concerning the PSR diagram of VA, there are three types of VA (VT, VF and VT followed by VF), which are shown in Fig.6.3. The PSR diagrams of VT with 0.02 seconds and 0.08 seconds are shown in top left and bottom left respectively. It can be seen the trajectories are consisted of different sizes of circles. Since VT is a type of regular heart activity. Comparing with VT, the PSR diagrams of VF are more chaotic because it is an irregular heart activity. As shown in the middle two PSR diagrams of VF, the most of the trajectories are in the center part of the PSR diagram. The PSR diagrams of VT followed by VF are not as chaotic as the VF, but more disordered than VT. These different features of PSR diagram can be used to classify different types of ECGs. Hence, it is possible to develop an arrhythmia classifier based on PSR and box-counting techniques. The proposed method based on PSR features for arrhythmia classification will be given in the next section.

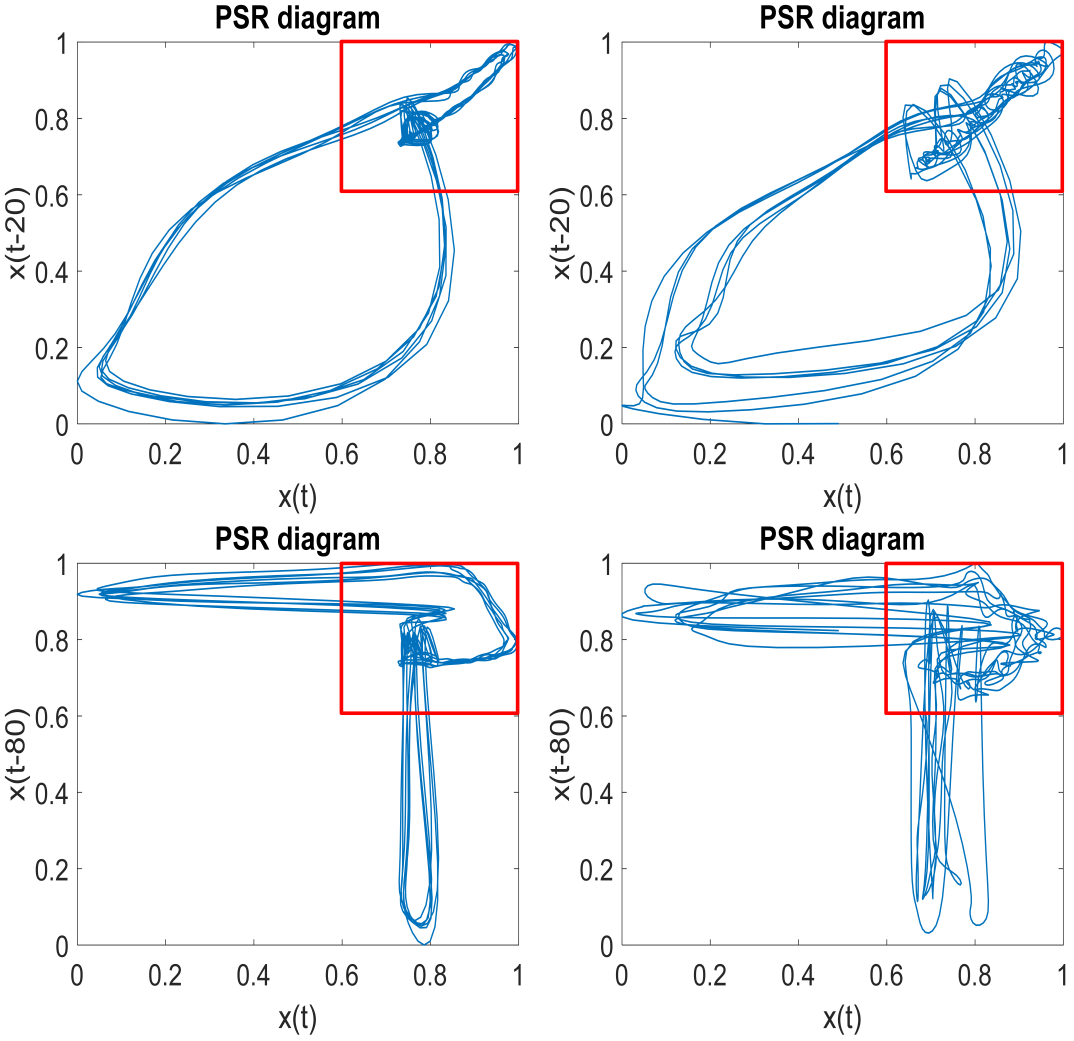

FIGURE 6.2: The PSR diagrams of normal ECG (left) and AF (right). (Top: 0.02s time delay; Bottom: 0.08s time delay))

6.3 Methodology

In this section, we will present the proposed method based on PSR and box-counting. Our proposed algorithm aims to classify 4 types of arrhythmias (AF, VT, VF and VT followed by VF), it is structured as a three-stage process as shown in Fig.6.4. First step is ECG pre-processing, which includes noise removal and data normalization. The next step is feature extraction. PSR features are extracted from each clear ECG window based on two different values of time delay. Finally, the classification model is developed by taking 50% of the ECG data. Remaining 50% data is used for validation of the proposed classification algorithm.

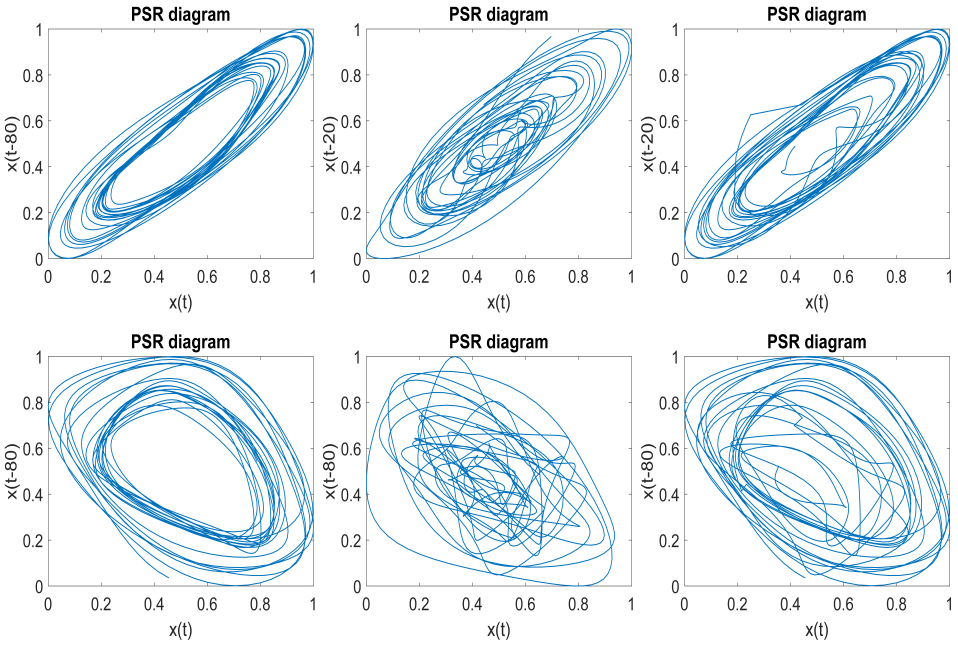

FIGURE 6.3: The PSR diagrams of VT (left), VF (middle) and VT followed by VF (right). (Top: 0.02s time delay; Bottom: 0.08s time delay)

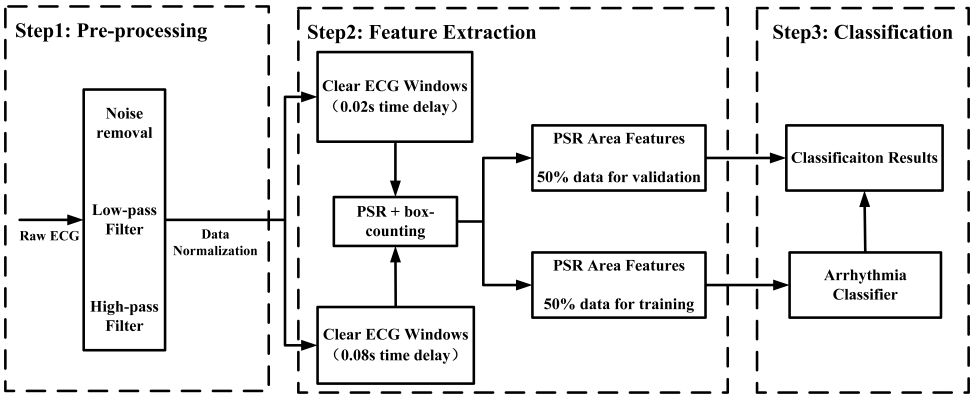

FIGURE 6.4: The system overview of the proposed algorithm.

6.3.1 Data and Pre-processing

Three publicly available ECG databases (PTBDB, MIT-BIH AFDB, CUDB) from PhysionetGoldberger et al. (2000) and UHS database has been used to develop and validate our proposed algorithm. 32 healthy records from PTBDB are used in our work and each record includes 15 simultaneously measured signals (12 conventional leads and 3 Frank leads), therefore it has 480 healthy signals (but some of these leads will be very correlated) Bousseljot et al. (1995). MIT-BIH AFDB has 23 AF records, CUDB contains 32 VA records (13 VT, 9 VF and 10 VT followed by VF) Moody (1983); Nolle et al. (1986). Among these three public databases, the sampling frequency of PTBDB is 1000 Hz while that of the other two are both 250 Hz. Our UHS database has 35 4 hours long-term records, with 24 healthy, 10 VF and 1 VT. ECG signal was obtained using a five-lead two channel digital Holter recorder (Model AFT-1000, Holter Supplies, Paris)

and was downloaded in ASCII format at a frequency of 250Hz. In order to have a uniform platform for all four databases, sample frequency of the PTBDB was decreased to 250 Hz. To make sure each ECG window has sufficient features, an appropriate length of 5 seconds ECG time window has been chosen in our work, and the sample number of each window is 1250. In PTBDB, the total number of the window for one record (15 signals) was found 90 and hence 2880 windows of normal ECG were found in this database. Also, a total window of 2802 for AF was obtained in the entire MIT-BIH AFDB. Concerning CUDB (including 2 leads), we have obtained 1272 windows of VT, 1144 windows of VF and 816 windows of VT followed by VF. And a total number of 6912 for normal ECG, 1341 for VF and 740 for VT were found in entire UHSDB. In our work, a large number of normal ECG windows of UHSDB were not considered in order to maintain a balance between the numbers of these 5 classes. Overall, 2880 windows of normal ECG, 2802 windows of AF, 2012 windows of VT, 2485 windows of VF and 816 windows of VT followed by VF were used in our work.

In our work, ECG noise removal is necessary, since the PSR yields best results if the ECG signals are noise-free Cappiello et al. (2014). Here, a common filtered method is applied to remove ECG noise and baseline wandering Amann et al. (2005). It is consisted of a fourth order Butterworth high-pass filter followed by a low-pass filter with the corresponding cut-off frequency of 1 Hz and 30 Hz respectively. ECG data normalization is also necessary in order to ensure that value of all ECG samples in a same window are within a range of (0,1) Vemishetty et al. (2019). The expression of data normalization equation is shown in (6.1), where x_{min} and x_{max} are the minimum and the maximum value of the filtered ECG signals $x(t)$ in one window, $\widetilde{x}(t)$ is the final normalized ECG signals.

$$\widetilde{x}(t) = (x(t) - x_{min})/(x_{max} - x_{min}) \tag{6.1}$$

6.3.2 Feature extraction

Following the detailed analysis of the PSR diagram of normal ECG with 0.08 s time delay, there are three different situations which can be seen in Fig.6.5. The trajectories only go through top right, middle or left bottom of the PSR diagram. Therefore, if we can divide the PSR diagram into 9 areas, we will find most of PSR trajectories only lie in 5 areas, depending on the area with the highest degree. Here, the degree of complexity or fractal dimension of a specific area of a PSR diagram is defined as follows $d_a = n_a/((n_b + n_w))a = 1, 2 \cdots 9$, where a is the number of the specific area. When the area with the highest degree is area 3 (left of Fig.6.5), then the most of the PSR trajectories are in area 1, 2, 3, 6 and 9. If the area with the highest degree is area 5 (middle of Fig.6.5), the most of the PSR trajectories are in area 2, 4, 5, 6 and 8. When area 7 has the highest degree (right of Fig.6.5), the most of the PSR trajectories lie in

area 1, 4, 7, 8 and 9. However, the PSR trajectories of VA are completely different to the PSR trajectories of normal ECG and AF. As shown in Fig.6.3, although the overall outlines of the PSR diagrams of three different types of VA are similar, they still have difference in area 5. From the analysis of VA records, for VT, the area 5 is relatively empty. The PSR trajectories of VF are more concentrated, thus the degree in area 5 is higher than VT. Concerning VT followed by VF, the degree in area 5 is lower than VF but higher than VT. In our work, degree ($d_a a = 1, 2 \cdots 9$)of nine specific areas of every PSR diagram was calculated. All these features of 50% ECG data were used to train the classification model and the remaining 50% ECG windows were used for validation. The detailed description of our classification step will be given in the next section.

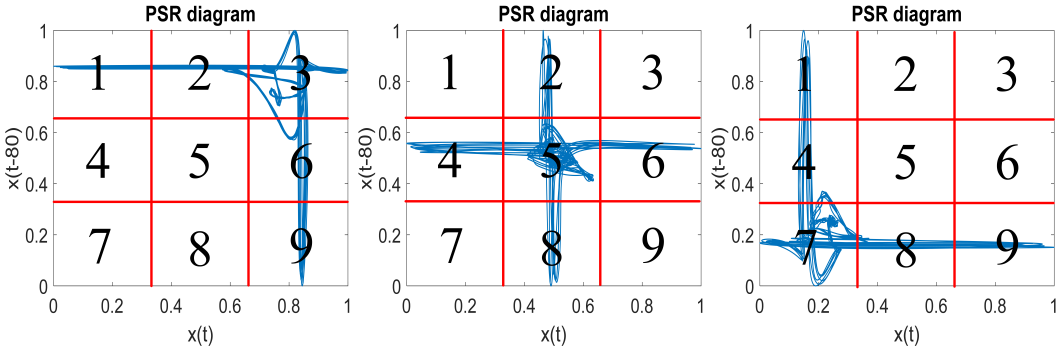

FIGURE 6.5: 9 areas of PSR diagrams of normal ECG (0.08 s time delay).

6.3.3 Classification

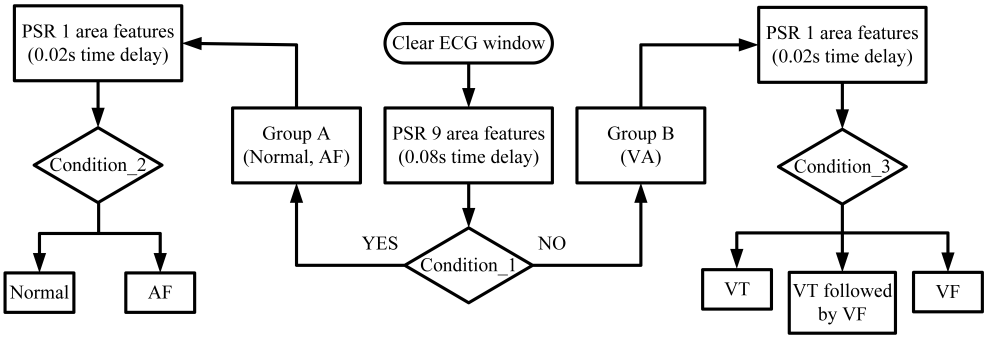

FIGURE 6.6: The structure of arrhythmia classifier.

The classification method can be divided into two main steps as shown in Fig.6.6. First is to classify two main groups by $Condition_1$ Group A is normal ECG and AF windows and group B contains three types of VA (VT, VT followed by VF and VF). As mentioned in the previous section, when time delay of PSR is 0.08 seconds, most of the PSR trajectories of normal ECG and AF only lie in 5 areas. For normal ECG and AF, when area with the highest degree is area 3 the most of the PSR trajectories are in area 1, 2, 3, 6 and 9. If area with the highest degree is area 5, the most of the PSR trajectories are in area 2, 4, 5, 6 and 8. And if area 7 has the highest degree, the

most of the PSR trajectories lie in area 1, 4, 7, 8 and 9. Here, the degrees of PSR 9 areas ($d_{a(0.08)}, a = 1, 2 \cdots 9$) based on 0.08 seconds time delay are calculated using $d_{a(0.08)} = n_{a(0.08)}/n_{b(0.08)}$, where $n_{a(0.08)}$ is the number of black boxes in area a and $n_{b(0.08)}$ is the number of whole black boxes when time delay is 0.08 seconds, also the highest $d_{a(0.08)}$ among 9 areas is defined as $d_{h(0.08)}$. It is important to calculate the sum of the degrees in these five areas and find a threshold between two groups. In this case, we used half of ECG data to find the threshold to classify two groups. For group A, the minimum value is 0.962 and for group B the maximum value of 0.822. Then, it is possible to define a condition to classify group A and group B as shown in (6.2). The threshold is defined as the average value between the minimum value of group A and maximum value of group B. If the PSR features of one ECG window satisfy one situation of $condition_1$, this window is considered as group A. Otherwise, it belongs to group B.

$$Condition_1 = \begin{cases} d_{h(0.08)} = d_3, d_1 + d_2 + d_3 + d_6 + d_9 \geq 0.9; or \\ d_{h(0.08)} = d_5, d_2 + d_4 + d_5 + d_6 + d_8 \geq 0.9; or \\ d_{h(0.08)} = d_7, d_1 + d_4 + d_7 + d_8 + d_9 \geq 0.9. \end{cases} \tag{6.2}$$

Second step is to classify normal ECG and AF in group A using $Condition_2$. Also to classify VT, VT followed by VF and VF in group B using $Condition_3$. In order to reduce the computational complexity of our proposed method, we only analyzed the features in a specific area with highest degree $d_{h(0.02)}$ based on 0.02 seconds time delay and $d_{h(0.08)}$ based on 0.08 seconds time delay. In our work, the difference (d-value) between $d_{h(0.02)}$ and $d_{h(0.08)}$ was calculated for each ECG window to analyse the self-similarity of PSR features in this specific area. The d-value distributions of group A and group B are shown in the left and right of Fig.6.7 respectively.Upon observation, it is noticed that the d-value of normal ECG have two different situations in group A (see red bars). A deeper analysis showed that for these normal ECG windows with large d-value, the some T-waves are relatively larger leading to some extra large closed circles in PSR diagram when time delay is 0.02 seconds. The detailed parameters based on the d-value for training data are shown in Table.6.1. For group A, PSR features were extracted from 1440 normal ECG windows and 1401 AF windows. For group B, the number of windows we used for VT, VT followed by VF and VF are 1006, 408 and 1283 respectively. Parameter d for each window was calculated and the mean and standard deviation (SD) of each group were calculated as well. For the statistical analysis, we usually select confidence levels of 95% Moyé (2016). However, we chose the confidence levels of 99% in order to clearly see the difference between each group. The values of Upper Confidence Level (UCL) and Lower Confidence Level (LCL) of all groups are shown in the Table.6.1. The UCL of (Normal 1) cases in all windows is lower than the LCL of AF cases, and the LCL of (Normal 2) cases is higher than the UCL of AF cases as shown on the top of Fig.6.8. Therefore, for group A, the average value between UCL of (Normal 1) cases and LCL of AF cases is used to classify test ECG windows of Normal

TABLE 6.1: The detailed parameters for arrhythmia classification

Parameters	Group A			Group B		
	Normal 1	AF	Normal 2	VT	VT followed by VF	VF
Mean	0.0527	0.1159	0.2358	0.1983	0.1614	0.0784
SD	0.0159	0.0220	0.0185	0.0132	0.0184	0.0289
99% LCL	0.0151	0.0735	0.2066	0.1840	0.1180	0.0299
99% UCL	0.0676	0.1445	0.2634	0.2209	0.1896	0.1253

1 and AF. Also, the average value LCL of (Normal 2) cases and UCL of AF cases is used to classify test ECG windows of Normal 2 and AF. The $Condition_2$ is shown in (6.3).

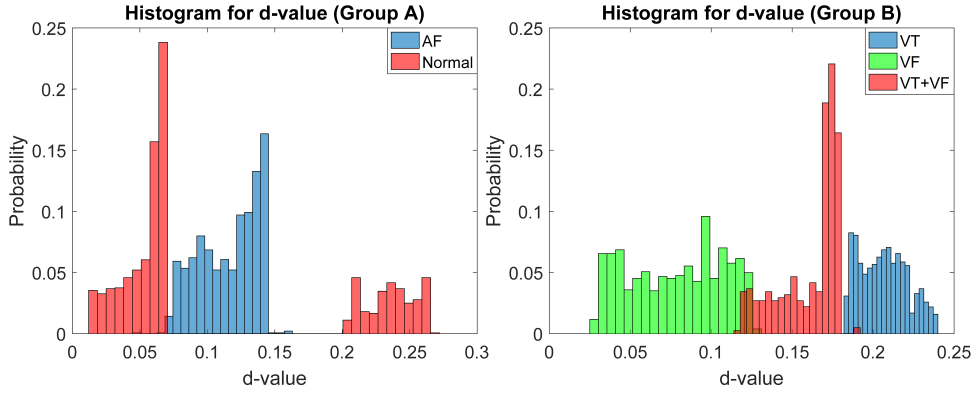

FIGURE 6.7: The histogram of d-value distribution. (left: group A; right: group B)

$$Condition_2 = \begin{cases} \text{if } d < 0.0706 & \text{Normal} \\ \text{if } 0.0706 \leq d \leq 0.1760 & \text{AF} \\ \text{if } 0.1760 < d & \text{Normal} \end{cases} \tag{6.3}$$

Concerning three types of VA in group B, it is noticed that the LCL of VT followed by VF cases in all windows is slightly lower than the UCL of VF cases, and the UCL of VT followed by VF cases is slightly higher than the LCL of VT cases as shown on the bottom of Fig.6.8. There exist overlaps because the ECG windows of VT followed by VF may contain both similar features of VT and VF. However, the overlaps are small and hence it can only make little influence for classification. In our work, since the VT followed by VF cases finally go to the VF condition, they can also be considered as VF. We decided to use the UCL of VF cases to classify VF and VT followed by VF. Also, the average value of UCL of VT followed by VF cases and LCL of VT cases is used to classify VT and VT followed by VF. The decision $Condition_3$ is given in (6.4).

$$Condition_3 = \begin{cases} \text{if } d < 0.1253 & \text{VF} \\ \text{if } 0.1253 \leq d \leq 0.1868 & \text{VT+VF} \\ \text{if } 0.1868 < d & \text{VT} \end{cases} \tag{6.4}$$

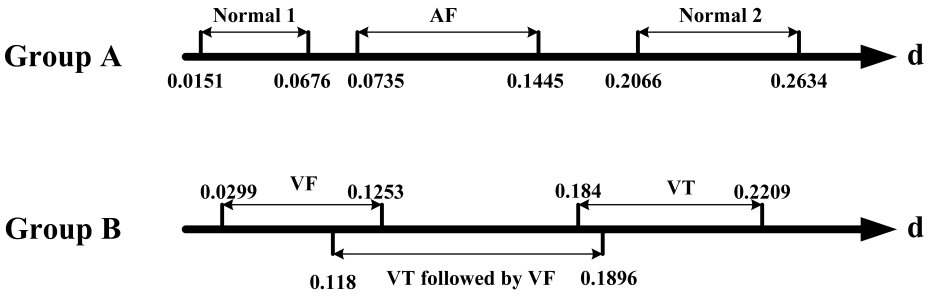

FIGURE 6.8: 99% confidence levels of d for all types ECG in two groups.

6.4 Results and Discussion

6.4.1 Classification performance

In our work, we applied confusion matrix and Receiver Operator Characteristic (ROC) curve to evaluate our classification results. The confusion matrix and ROC are shown on the left and right of Fig.6.9 respectively. As shown in the confusion matrix, among 1440 normal ECG windows, 20 windows are classified as AF windows. For 1401 AF windows, 24 windows are considered as normal ECG window. Besides, 8 VT windows are classified as VT followed by VF. 2 windows of VT followed by VF is recognized as VT and 8 VT followed by VF windows are considered as VF. The overall accuracy of our proposed classifier is 98.9%. Another interesting observation comes from the analysis of the first classification of group A and B. All normal ECG and AF windows are classified as group A and all VA windows are recognized to group B, also all VA windows belong to group B. It reflects the accuracy of the first step of classification is 100%. Thus it is possible to say our proposed algorithm first has potential to distinguish between VA and other heart conditions. Concerning ROC figure, the middle gray line means random guess (50% accuracy), and the classification performance is better when ROC is more close to 1. From our results, the ROC of five types of ECG conditions are all close to 1 and it means our algorithm has high performance for arrhythmia classification.

For deeper evaluation of our proposed method, the leave one out cross validation (LOOCV) approach is applied for the five types of ECG windows. Each specific type of ECG is considered as Positive P and other four types represent Negative N. The true positive (TP), false positive (FP), true negative (TN) and false negative (FN) are used to calculate the

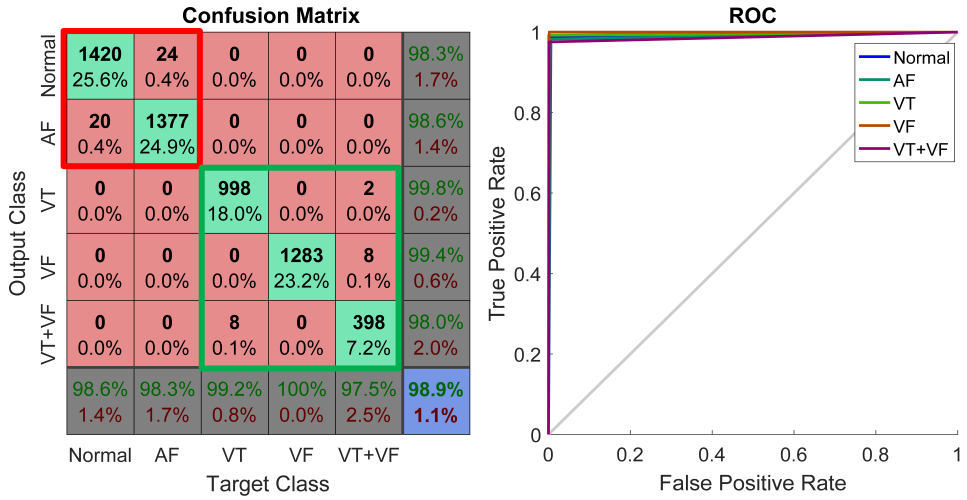

FIGURE 6.9: The confusion matrix of classification (left), the corresponding ROC (right).

TABLE 6.2: The classification performance under a LOOCV scheme

Classification Measures(%)	Group A		Group B			Average	Standard Deviation
	Normal	AF	VT	VT+VF	VF		
SE	98.61	98.29	99.20	97.55	100	98.73	0.83
SP	99.41	99.52	99.96	99.84	99.81	99.71	0.21
ACC	99.20	99.21	99.82	99.68	99.86	99.56	0.29
PPV	98.34	98.57	99.80	98.03	99.38	98.82	0.66
NPV	99.51	99.42	99.82	99.81	100	99.71	0.21
FPR	0.59	0.48	0.04	0.16	0.18	0.29	0.21
FDR	1.66	1.43	0.20	1.97	0.62	1.18	0.66
FNR	1.39	1.71	0.80	2.45	0	1.27	0.83
F_1 score	98.47	98.43	99.5	97.79	99.69	98.78	0.71

serval classification measures. In our work, sensitivity (SE), specificity (SP), accuracy (ACC), positive predictive value (PPV), negative predictive value (NPV), false positive rate (FPR), false discovery rate (FDR), false negative rate (FNR) and F_1 score using the following formulas in(6.5).These classification performance measures are shown in Table.6.2.

$$\begin{cases} \mathrm{SE} = \mathrm{TP/P} = \mathrm{TP}/(\mathrm{TP}+\mathrm{FN}), \mathrm{SP} = \mathrm{TN/P} = \mathrm{TN}/(\mathrm{FP}+\mathrm{FN}), \\ \mathrm{ACC} = (\mathrm{TP}+\mathrm{TN})/(\mathrm{P}+\mathrm{N}), \mathrm{PPV} = \mathrm{TP}/(\mathrm{TP}+\mathrm{FP}), \\ \mathrm{NPV} = \mathrm{TN}/(\mathrm{TN}+\mathrm{FN}), \mathrm{FPR} = \mathrm{FP/N} = \mathrm{FP}/(\mathrm{FP}+\mathrm{TN}), \\ \mathrm{FDR} = \mathrm{FP}/(\mathrm{FP}+\mathrm{TP}) = 1-\mathrm{PPV}, \mathrm{FNR} = \mathrm{FN}/(\mathrm{FN}+\mathrm{TP}), \\ \mathrm{F_1score} = 2\mathrm{TP}/(2\mathrm{TP}+\mathrm{FP}+\mathrm{FN}) \end{cases} \tag{6.5}$$

We only have 408 ECG windows for VT followed by VF, 7.4% of whole data. This proportion is much less than others. Thus, it is necessary to calculate the classification performance measures for each data class. The average value of SE, SP and ACC are 98.73%, 99.71% and 99.56% respectively for five types of ECG windows. The results show a relatively lower average value of SE, since the SE value of VT followed by VF is lower than other four groups. Among these five groups, the results in VT followed by VF show relatively lower SE, ACC and PPV. Since the features from VT followed by VF windows contain both features from VT and VF windows, thus these windows of VT followed by VF may be recognized as VT or VF windows. The FN of this group is higher than others, leading to a lower SE. In group A, the SE, PPV of normal ECG and AF are also lower than other parameters. This phenomenon reflects that the classification of AF and normal ECG is not good as the classification of VT and VF. The reason might be the difference of PSR diagram between AF and normal ECG is more relatively similar.

The performance results of our proposed method for arrhythmia classification were compared to the literature and are presented in Table.6.3. Our proposed method presents a higher or comparable sensitivity of 99.2%, specificity of 99.88% and accuracy of 99.81% than other methods in literature. Most of the studies were focus on VT and VF classification. Tripathy et al. (2018) suggested to use magnitude and phase difference features for each 8 s time windows with the least square SVM to classify VT and VF with 93.97% accuracy. However, the sensitivity and specificity are lower than 90%, which are lower than the other cited methods. The similar SVM classifier was used in Sharma et al. (2020) based on the combined features that is consisted of Fuzzy entropy and Renyi entropy parameters to classify shockable and nonshockable arrhythmias with accuracy of 97.8%, sensitivity of 93.42% and specificity of 98.35%. A novel Boosted-CART method was introduced to combine with 6 features from the band-limited intrinsic modes (BLIMs) to classify VT and VF with a high accuracy of 98.29% Xu et al. (2018). Gawde et al. (2017) integrated that Markov model can be used to classify VT and VF by matching probabilistic transition graph of ECG and the performance showed an average sensitivity of 96.15% and a specificity of 93.5%. Mohanty et al. (2018) represented a new C4.5 algorithm to classify normal ECG, VT and VF based on time-frequency domain and finally got an accuracy of 97.02% Roopaei et al. (2010) developed a new algorithm based on PSR matrix with AND operation to classify normal ECG, VT and VF with an accuracy of 94%. Also, a real-time ECG signal monitor was developed based on complex phase space difference (CPSD) algorithm Liu et al. (2010). The appropriate threshold values were set to 2.0 and 6.0 to classify normal ECG, AF and VF with a sensitivity of 100% and specificity of 98.8%. Although this method achieved a higher sensitivity than our proposed method, it used different thresholds for different types of ECG signals. It differentiated VF and normal ECG based on threshold of 2, but for VF and AF classification, the threshold was set to 6. It is noticed that in reality, we don not know the specific type of one ECG window before classification. Hence it is

impossible to set specific threshold for classification of some specific types of arrhythmia in a real-time biomedical signal processing application.

In Table.6.3, the overall performance of multi-features-combining classification methods Tripathy et al. (2018); Sharma et al. (2020); Xu et al. (2018); Tripathy et al. (2016); Weixin (2016); Acharya et al. (2018); Mohanty et al. (2018) are better than other single-feature-based classification methods Gawde et al. (2017); Roopaei et al. (2010); Liu et al. (2010). Xu et al. (2018) also suggested that compared with the single-feature-based methods, the performances of the multi-features-combining methods are better. However, although we proposed a single-feature-based method in this work, we still show that the performance of our method is even better than other multi-features-combining methods. Comparing with these cited methods that used the similar features with our work Roopaei et al. (2010); Liu et al. (2010), the improvement of our method is the thorough exploration of single-phase space feature by extracting features from a specific area of the phase-space diagram. Although it seems that our method is based on the single phase space feature, in essence, each single feature is divided into 9 parts and all of these features are used to classify VA. Therefore, our work also can be considered as a multi-features-combining method. The main advantage of our method is that it not only has the low computational complexity as the single-feature-based method, but also has the comparable or higher performance than such multi-featurescombining methods. The detailed information in terms of computational complexity of our method is described in the next section.

6.4.2 Complexity analysis

The implementation of our proposed algorithm for validation took place in MATLAB R2018a. The computational complexity of our algorithm is briefly given in Table.6.4. In our proposed algorithm, the main computational complexity is due to determine the number of black boxes in the PSR diagram. The PSR diagram is divided into $N \times N$ pixels, hence, the main computational complexity of the processing of one PSR diagram is $O(N^2)$. For each ECG window, our proposed method need to generate two PSR diagrams with different time delay. Therefore the total computational complexity of our proposed method is $O(2N^2)$. In addition, the average run-time of our proposed algorithm for one 5 seconds time window ECG against the value of N is plotted on the left of Fig.6.10. The computational time rise steadily when the value of N increases from 2^6 to 2^{10} and the run-time is 1.9 seconds at 2^{10}. However, it increases suddenly at $N = 2^{11}$ from 1.9 seconds to 4.7 seconds and finally goes to 8.3 seconds at $N = 2^{12}$.If computational time of one 5 seconds window is larger than 5 seconds, it does not have potential to achieve real-time processing. Thus, N larger than 2^{11} is not considered in our work. The right of Fig.6.10 shows how much the number of pixels can affect the overall accuracy of the proposed method. It shows that the value of N is proportionate to

TABLE 6.3: Comparison of the performance of arrhythmia classification with other literature.(The window length is reported as w)

Author	Classifier (Features)	w(s)	arrhythmia classes	Performance (%)
Tripathy et al. (2018)	SVM classifier (Magnitude-phase)	8	VT,VF	SE:89.81, SP:86.38 ACC:93.97
Sharma et al. (2020)	SVM classifier (Multi-entropy features)	2	VT,VF (Shock or non-shock)	SE:93.42, SP:98.35 ACC:97.8
Xu et al. (2018)	boosted-CART (6 different features)	5	VT,VF	SE:97.32, SP:98.95 ACC:98.29
Gawde et al. (2017)	Markov model (Probabilistic transition graph)	10	VT, VF	SE:96.15, SP: 93.5
Tripathy et al. (2016)	Random forest (7 different features)	5	VT,VF (Shock or non-shock)	SE:96.54, SP:97.97 ACC:97.23
Weixin (2016)	FLCL (time,frequency,complex)	8	VT, OVF, DVF	SE:90.2, SP:95.1 ACC:92.6
Acharya et al. (2018)	CNN (27 different features)	2	VT,VF (Shock or non-shock)	SE:93.18, SP:95.32 ACC:91.04
Mohanty et al. (2018)	C4.5 classifier (time-frequency)	5	Nor,VT,VF	SE:90.97, SP:97.86 ACC:97.02
Roopaei et al. (2010)	Threshold (phase space)	8	Nor,VT,VF	Acc: 94
Amann et al. (2006)	Threshold (phase space)	8	Nor,VF	SE:79, SP:97.8 ACC:96.2
Liu et al. (2010)	Threshold (phase space)	1	Nor,AF,VF	SE:100, SP:98.8
Proposed Method	Threshold (phase space)	5	Nor,AF,VT VF,VT+VF	SE:98.73, SP:99.71 ACC: 99.56

TABLE 6.4: Computational complexity of the proposed method. (Parameter N is the number of pixels in row or column and directly affect the order of computation).

The proposed method	Order of cumputation
Step1: PSR and box-counting ($\tau = 0.02s$)	O(N^2)
Step2: PSR and box-counting ($\tau = 0.08s$)	O(N^2)
Total	O($2N^2$)

the overall accuracy before $N = 2^{11}$. The overall accuracy starts at 86.3% when $N = 2^6$ and increase to 98.9% when $N = 2^{10}$. The overall accuracy finally goes to 99.0% when $N = 2^{11}$ and 2^{12}. Overall, we think the optimum performance is achieved for $N = 2^{10}$. It shows lower computational time consumption and relatively higher accuracy when $N = 2^{10}$. The average computational time for one 5 seconds window is 1.9 seconds, it is noticed that our proposed algorithm has sufficient time to classify one ECG window before the next time window coming. Thus, our proposed method has potential for developing a real-time system.

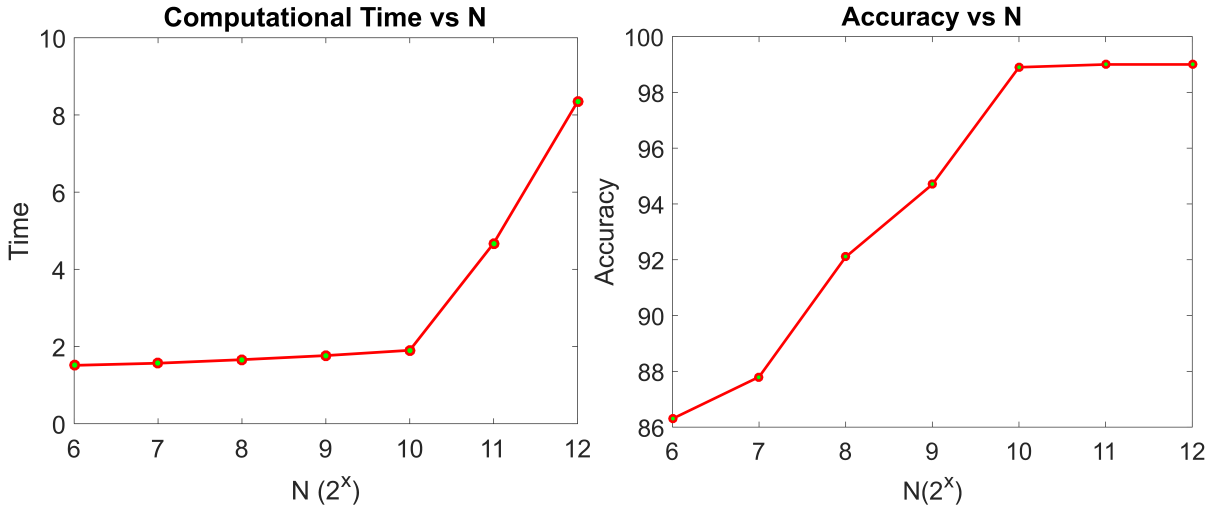

FIGURE 6.10: The run time versus N (left), the overall accuracy versus N (right).

6.5 Concluding Remarks

A novel and efficient arrhythmia classification method has been proposed in this chapter. The specific area features of PSR diagram for each ECG window were used to classify normal ECG, AF, VT, VF and VT followed by VF. When tested on four databases, the results showed our proposed method can classify normal ECG, AF, VT, VF, and VT followed by VF with a sensitivity of 98.73% and a specificity of 99.71%. The computational complexity is $O(2N^2)$ and average time for processing of one 5s ECG window is 1.9s when $N = 2^{10}$ with an average accuracy of 99.56%. However, as mentioned before, 50%

of the ECG windows from each record were used to train the classification model. There will be a problem of 'data leakage', where information about the training set has leaked into the test set and would lead to over-optimistic results. Therefore, our future work will first randomly select 50% of ECG records and train a new classification model based on all ECG windows from each selected record. Then test our classification algorithm on the remaining ECG windows to show a more objective result. Besides, the further work can be done by testing our algorithm on more databases to classify more types of arrhythmias. Exploration of ECG leads that can give the best classification results is also included in our future work. Moreover, since the computational complexity of our proposed algorithm is low, it would be useful to integrate it with ICD systems for improving a patient's quality of life. However, the real-time performance evaluation of the integrated system should be done in a proper clinical trial. In the next chapter, we will provide the conclusions of our whole work presented in this dissertation and will discuss the future work in detail.

Chapter 7

Conclusions and Future Work

7.1 Conclusions

In this thesis, we propose an algorithm for predicting VA through step-by-step analysis of ECG signal coupled with innovative signal processing and machine learning methods.

We have first introduced an automated ECG delineation algorithm with high precision. The experimental results in terms of positive detection (+P) and sensitivity (SE) that tested on MIT-BIH database and QT database are used to evaluate the proposed algorithm. The results also compared with other formally published methods and show a high performance for ECG feature extraction. Our algorithm achieved 99.89% of Se and 99.94% of +P , 100% of Se and 99.83% of +P for R peak detection in MIT-BIH and QT database respectively. It also shows 99.91% of Se and 99.38% of +P for T peak detection in QT database.

We have also presented a PSR-based algorithm to reduce TWOS in S-ICD system. The algorithm has been evaluated against 34 records from University Hospital Southampton (UHS) and all records from the MIT-BIH arrhythmia database. In the UHS analysis we demonstrate a sensitivity of 99.88% and a positive predictive value of 99.99% with reductions in TWOS episodes (from 166 to 0). Whilst in the MIT-BIH analysis we demonstrate a sensitivity of 99.87% and a positive predictive value of 99.99%, with effective reduction in the number of false positives in R wave detection.

We have proposed a novel algorithm based on the combination of PSR and Fuzzy C-means (FCM) clustering technique of the ECG for prediction and classification of VA. 32 healthy subjects and 32 arrhythmic subjects from PTBDB and CUDB respectively were used to evaluate our proposed technique. The proposed system showed 298.3 seconds of an average prediction time for impending ventricular arrhythmia based on 32 VA subjects. Also, our system can classify four types of VA (VA without VPBs, VF, VT, and VT followed by VF) with an average 238.3 seconds before the VA onset. It achieved

an average accuracy of 98.4%, a sensitivity of 97.5% and specificity of 99.1%, which was comparable and better than the previous works. This study has demonstrated that this algorithm can be used to predict and classify the impending VA.

Finally, a simple PSR-based arrhythmia classifier has been developed to classify normal ECG, atrial fibrillation (AF), VT, VF and VT followed by VF. This process was verified with 122 records with more than 5500 windows of ECG signals. The results show an average sensitivity of 98.73%, specificity of 99.71% and accuracy of 99.56%.

Overall, this thesis first has contributed to develop an automatic algorithm with high performance for ECG feature extraction. In addition, this thesis argued that PSR is a simple and effective tool for ECG processing, which has been prove to reduce TWOS in S-ICD system and to analyse arrhythmias. The main contribution of this thesis is to develop a method for fatal arrhythmia prediction and classification. These results could be implemented in hardware which could be integrated with an S-ICD to prevent Sudden Cardiac Death (SCD). It is hoped that the findings of our research will contribute towards ECG applications for arrhythmia prevention.

7.2 Future Work

In this thesis, we have worked on the four objects, which are developments of an automated ECG delineation algorithm, reduction of TWOS in S-ICD and arrhythmia prediction and classification. It is seen that there are three main objectives for the next research, which will discuss in the next sections. We have published three journal articles based on the previous work and aim to publish another journal article in this year. Furthermore, it is possible to write two more articles. First is based on the correlation between body fluid and ECG features during dialysis. Another paper might be considered as the FPGA implementation of the system based on our previous work. The following have been identified as our potential future research challenges during the research study undertaken in this thesis.

7.2.1 Arrhythmia Prediction and Classification

In addition to the VA prediction in Chapter 5, the prediction of nonfatal arrhythmias is also important. Because nonfatal arrhythmias could be precursors for cerebrovascular acute events. For example AF is associated with increased morbidity and mortality that primarily occur as a result of stroke Vlachos et al. (2016). Besides, it is important to classify all types of arrhythmias as well as the prediction so that the clinician can prevent and treat the life-threating arrhythmias. Therefore, in our future work more databases - such as MIT-BIH Atrial Fibrillation DB and Supraventricular Arrhythmia DB will be used to validate our arrhythmia prediction and classification algorithm (In Chapter

5). The results will be used to evaluate the performance for other nonfatal arrhythmia prediction and the classification of these all types of arrhythmia.

7.2.2 Correlation between body fluid and ECG features

Another interesting aspect of ECG analysis is to understand the correlation between ECG features and the change of fluid in the body during dehydration. The ECG acquired during dialysis (data available from UHS) will be used for understanding the correlation between body fluid and ECG features. We will consider several possibilities of the relationship between the body fluid and ECG features in the different domain. For example, assuming that the relation between fluid loss and time is linear, it means the fluid losses in the same space of time are equal during dialysis. Next step is to detect the ECG features for each same time window and try to associate any features with fluid loss. The results above will be incorporated within the predictive algorithm developed earlier and we will expect if this give the better predictability of arrhythmia.

7.2.3 Hardware implementation

Current stage of our work still stays at the software algorithms level. The final aim of our work is to design a hardware platform that can be integrated with S-ICD to prevent SCD caused by fatal arrhythmia. In this case, it is possible to translate the proposed algorithms (artefact separation, ECG delineation, arrhythmia prediction and classification) into a single hardware framework creating a wearable system. Besides, considering such real-time system need to be low power consumption, the computational complexity of our algorithms need to be further reduced. For example, the PSR diagram of ECG in our previous work was divided into $2^{10} \times 2^{10}$ pixels, in order to reduce the computational complexity, the number of pixel can be reduced but in that case one needs to examine the trade-offs between pixel reductions and accuracy. Therefore, the balance between performance and computational complexity need to be evaluated in the future work.

Appendix A

ECG Feature Extraction

The following lists the pseudocode of our ECG feature extraction algorithm

1: Initialize

2: Select the window length to process ECG data x[n]

(Normal based on the sampling frequency of the ECG database)

3: Hierarchical Clustering (Clusters number from 2 to 4)

4: R cluster detection $(C_1, C_2 \cdots C_n)$

5: R-peak initial estimation $(R_1, R_2 \cdots R_n)$

6: Set a threshold to determine R-peak $(250ms)$

7: if abs$(R_{k+1} - R_k) < 250ms$

8: then $R_{k+1} = max(R_{k+1}, R_k)$

9: end if

10: PQRST, QRS Initial Estimation

11: Using template x_m to determine the initial PQRST, QRS onsets (offsets)

12: $(T_{on}^{PQRST1}, T_{off}^{PQRST1}, T_{on}^{QRS1}, T_{off}^{QRS1}) \cdots (T_{on}^{PQRSTn}, T_{off}^{PQRSTn}, T_{on}^{QRSn}, T_{off}^{QRSn})$

13: PQRST, QRS Final Detection

14: Calculate Mean Square Error (MSE) between template and x[n]

15: $n \in [T_{on}^{PQRSTk} \pm 20, T_{off}^{PQRSTk} \pm 20]$, where $k = 1, 2 \cdots n$

16: Find the interval with minimum MSE

17: $mse_{k+h} = immse(x_m, x[n])$, $n \in [T_{on}^{PQRSTk} + h, T_{off}^{PQRSTk} + h]$, where $h \in [-20, 20]$

18: Find $mse = min(mse_{k+h})$, the corresponding interval is final PQRST boundary

19: Repeat PQRST block based on QRS template to determine QRS boundary

20: Determine the T wave boundary $[T_{off}^{QRSk}, T_{off}^{PQRSTk}]$, where $k = 1, 2 \cdots n$

21: HAAR DWT

22: Calculate the 2^4 and 2^5 resolution scale detailed coefficients Dc_4 and Dc_5 for each T wave

23: Scale 2^4 MMA

24: Find $t_{k1} = min(Dc_4[n])$, where $n \in [T_{off}^{QRSk}, T_{off}^{PQRSTk}]$

25: Find $t_{k2} = max(Dc_4[n])$, where $n \in [T_{off}^{QRSk}, T_{off}^{PQRSTk}]$

26: if $t_{k1} < t_{k2}$
27: Calculate $T_{k1} = t_{k1} \times 2^4$
28: Calculate $T_{k2} = t_{k2} \times 2^4$
29: $T_{peak[4]} = max(x[n])$,where $n \in [T_{k1}, T_{k2}]$
29: else
30: Calculate $T_{k1} = t_{k2} \times 2^4$
31: Calculate $T_{k2} = t_{k1} \times 2^4$
32: $T_{peak[4]} = min(x[n])$,where $n \in [T_{k1}, T_{k2}]$
33: end if
34: Repeat for scale 2^5 MMA to obtain $T_{peak[5]}$
35: $T_{peak} = max(abs(T_{peak[4]}, T_{peak[5]}))$

Detail MATLAB code can be found in (2020) ECG R and T-peak detection. Code Ocean ($doi : 10.24433/co.5608972.v1$) [Dataset]

Bibliography

Syed Muhammad Abubakar, Wala Saadeh, and Muhammad Awais Bin Altaf. A wearable long-term single-lead ecg processor for early detection of cardiac arrhythmia. In *2018 Design, Automation & Test in Europe Conference & Exhibition (DATE)*, pages 961–966. IEEE, 2018.

U Rajendra Acharya, Hamido Fujita, Shu Lih Oh, U Raghavendra, Jen Hong Tan, Muhammad Adam, Arkadiusz Gertych, and Yuki Hagiwara. Automated identification of shockable and non-shockable life-threatening ventricular arrhythmias using convolutional neural network. *Future Generation Computer Systems*, 79:952–959, 2018.

E Roland Adams and Anthony Choi. Using neural networks to predict cardiac arrhythmias. In *2012 IEEE International Conference on Systems, Man, and Cybernetics (SMC)*, pages 402–407. IEEE, 2012.

Arrhythmia Alliance. Types of arrhythmia, 2019.

Felipe Alonso-Atienza, Eduardo Morgado, Lorena Fernandez-Martinez, Arcadi García-Alberola, and Jose Luis Rojo-Alvarez. Detection of life-threatening arrhythmias using feature selection and support vector machines. *IEEE Transactions on Biomedical Engineering*, 61(3):832–840, 2013.

Anton Amann, Robert Tratnig, and Karl Unterkofler. Reliability of old and new ventricular fibrillation detection algorithms for automated external defibrillators. *Biomedical engineering online*, 4(1):60, 2005.

Anton Amann, Robert Tratnig, and Karl Unterkofler. Detecting ventricular fibrillation by time-delay methods. *IEEE Transactions on Biomedical Engineering*, 54(1):174–177, 2006.

Moussa Amrani, Mohamed Hammad, Feng Jiang, Kuanquan Wang, and Amel Amrani. Very deep feature extraction and fusion for arrhythmias detection. *Neural Computing and Applications*, 30(7):2047–2057, 2018.

Krishnanand Balasundaram, Stephane Masse, Krishnakumar Nair, and Karthikeyan Umapathy. A classification scheme for ventricular arrhythmias using wavelets analysis. *Medical & biological engineering & computing*, 51(1-2):153–164, 2013.

Aksana Baldzizhar, Ekaterina Manuylova, Roman Marchenko, Yury Kryvalap, and Mary G Carey. Ventricular tachycardias: characteristics and management. *Critical Care Nursing Clinics*, 28(3):317–329, 2016.

Seema Bandyopadhyay and Edward J Coyle. An energy efficient hierarchical clustering algorithm for wireless sensor networks. In *IEEE INFOCOM 2003. Twenty-second Annual Joint Conference of the IEEE Computer and Communications Societies (IEEE Cat. No. 03CH37428)*, volume 3, pages 1713–1723. IEEE, 2003.

Nourhan Bayasi, Temesghen Tekeste, Hani Saleh, Baker Mohammad, Ahsan Khandoker, and Mohammed Ismail. Low-power ecg-based processor for predicting ventricular arrhythmia. *IEEE Transactions on Very Large Scale Integration (VLSI) Systems*, 24 (5):1962–1974, 2015.

Joachim A Behar, Laurent Bonnemains, Vyacheslav Shulgin, Julien Oster, Oleksii Ostras, and Igor Lakhno. Noninvasive fetal electrocardiography for the detection of fetal arrhythmias. *Prenatal diagnosis*, 39(3):178–187, 2019.

Sergey T Belyakin and A SS. Model fibrillation as an analogue of the hyperbolic the smale-williams attractor. *American Journal of Biomedical Science & Research*, 2(5): 197–201, 2019.

Lucas Boersma, Craig Barr, Reinoud Knops, Dominic Theuns, Lars Eckardt, Petr Neuzil, Marcoen Scholten, Margaret Hood, Juergen Kuschyk, Paul Jones, et al. Implant and midterm outcomes of the subcutaneous implantable cardioverter-defibrillator registry: the effortless study. *Journal of the American College of Cardiology*, 70(7):830–841, 2017.

R Bousseljot, D Kreiseler, and A Schnabel. Nutzung der ekg-signaldatenbank cardiodat der ptb über das internet. *Biomedizinische Technik/Biomedical Engineering*, 40(s1): 317–318, 1995.

Paul C Boutros and Allan B Okey. Unsupervised pattern recognition: an introduction to the whys and wherefores of clustering microarray data. *Briefings in bioinformatics*, 6(4):331–343, 2005.

Serge Boveda, Marijke C Laarakker, Christèle Cardin, and Jean-Paul Albenque. Impact of a novel algorithm designed to reduce t-wave oversensing with the subcutaneous defibrillator in a patient with type i brugada electrocardiogram. *HeartRhythm case reports*, 4(1):31, 2018.

Amy J Brisben, Martin C Burke, Bradley P Knight, Stephen J Hahn, Keith L Hermann, Venugopal Allavatam, Deepa Mahajan, Rick Sanghera, and Michael R Gold. A new algorithm to reduce inappropriate therapy in the s-icd system. *Journal of cardiovascular electrophysiology*, 26(4):417–423, 2015.

Martin C Burke, Michael R Gold, Bradley P Knight, Craig S Barr, Dominic AMJ Theuns, Lucas VA Boersma, Reinoud E Knops, Raul Weiss, Angel R Leon, John M Herre, et al. Safety and efficacy of the totally subcutaneous implantable defibrillator: 2-year results from a pooled analysis of the ide study and effortless registry. *Journal of the American College of Cardiology*, 65(16):1605–1615, 2015.

E. Burns. Ecg library, 2019.

Jian Cao, Jeffrey M Gillberg, and Charles D Swerdlow. A fully automatic, implantable cardioverter-defibrillator algorithm to prevent inappropriate detection of ventricular tachycardia or fibrillation due to t-wave oversensing in spontaneous rhythm. *Heart Rhythm*, 9(4):522–530, 2012.

Stefano Cappelli, Alina Olaru, and Elia De Maria. The subcutaneous defibrillator: who stands to benefit. *ESC Counc Cardiol Prac*, 12(17), 2014.

Grazia Cappiello, Saptarshi Das, Evangelos B Mazomenos, Koushik Maharatna, George Koulaouzidis, John Morgan, and Paolo Emilio Puddu. A statistical index for early diagnosis of ventricular arrhythmia from the trend analysis of ecg phase-portraits. *Physiological measurement*, 36(1):107, 2014.

CARDIOLOGYreview. Atrial fibrillation topic review, 2021a.

CARDIOLOGYreview. Premature ventricular contractions (pvcs) topic review, 2021b.

CARDIOLOGYreview. Ventricular fibrillation ecg review, 2021c.

CARDIOLOGYreview. Ventricular tachycardia (vt) ecg review, 2021d.

Matteo Cesari, Jesper Mehlsen, Anne-Birgitte Mehlsen, and Helge Bjarup Dissing Sorensen. A new wavelet-based ecg delineator for the evaluation of the ventricular innervation. *IEEE journal of translational engineering in health and medicine*, 5: 1–15, 2017.

Goutam Chakraborty, Takuya Kamiyama, Hideyuki Takahashi, and Tetsuo Kinoshita. An efficient anomaly detection in quasi-periodic time series data—a case study with ecg. In *International Work-Conference on Time Series Analysis*, pages 147–157. Springer, 2017.

Shubhojeet Chatterjee, Rini Smita Thakur, Ram Narayan Yadav, Lalita Gupta, and Deepak Kumar Raghuvanshi. Review of noise removal techniques in ecg signals. *IET Signal Processing*, 14(9):569–590, 2020.

Hanjie Chen, Saptarshi Das, John Morgan, and Koushik Maharatna. An effective psr-based arrhythmia classifier using self-similarity analysis. *Biomedical Signal Processing and Control*, 69:102851, 2021a.

Hanjie Chen, Saptarshi Das, John M Morgan, and Koushik Maharatna. Prediction and classification of ventricular arrhythmia based on phase-space reconstruction and fuzzy c-means clustering. *Computers in biology and medicine*, page 105180, 2021b.

Hanjie Chen and Koushik Maharatna. An automatic r-peak detection method based on hierarchical clustering. In *2019 IEEE Biomedical Circuits and Systems Conference (BioCAS)*, pages 1–4. IEEE, 2019.

Hanjie Chen and Koushik Maharatna. An automatic r and t peak detection method based on the combination of hierarchical clustering and discrete wavelet transform. *IEEE Journal of Biomedical and Health Informatics*, 2020.

Hanjie Chen, Benedict M Wiles, Paul R Roberts, John M Morgan, and Koushik Maharatna. A new algorithm to reduce t-wave over-sensing based on phase space reconstruction in s-icd system. *Computers in Biology and Medicine*, page 104804, 2021c.

Liu Chun-Lin. A tutorial of the wavelet transform. *NTUEE, Taiwan*, 2010.

Min Dai and Shi-Liu Lian. Removal of baseline wander from dynamic electrocardiogram signals. In *2009 2nd International Congress on Image and Signal Processing*, pages 1–4. IEEE, 2009.

Saptarshi Das and Koushik Maharatna. Machine learning techniques for remote healthcare. In *Systems Design for Remote Healthcare*, pages 129–172. Springer, 2014.

James P Daubert, Wojciech Zareba, David S Cannom, Scott McNitt, Spencer Z Rosero, Paul Wang, Claudio Schuger, Jonathan S Steinberg, Steven L Higgins, David J Wilber, et al. Inappropriate implantable cardioverter-defibrillator shocks in madit ii: frequency, mechanisms, predictors, and survival impact. *Journal of the American College of Cardiology*, 51(14):1357–1365, 2008.

Gaël de Lannoy, Benoît Frénay, Michel Verleysen, and Jean Delbeke. Supervised ecg delineation using the wavelet transform and hidden markov models. In *4th European Conference of the International Federation for Medical and Biological Engineering*, pages 22–25. Springer, 2009.

Jiao Dongdong, N Arunkumar, Zhang Wenyu, Li Beibei, Zhang Xinlei, and Zhu Guangjian. Semantic clustering fuzzy c means spectral model based comparative analysis of cardiac color ultrasound and electrocardiogram in patients with left ventricular heart failure and cardiomyopathy. *Future Generation Computer Systems*, 92: 324–328, 2019.

David L Donoho. De-noising by soft-thresholding. *IEEE transactions on information theory*, 41(3):613–627, 1995.

Rajkumar Doshi, Devina Adalja, Ashish Kumar, Mihir Dave, Mariam Shariff, Jay Shah, Nageshwara Gullapalli, Rupak Desai, Chintan Rupareliya, Yasar Sattar, et al. Frequency, trends, and outcomes of cerebrovascular events associated with atrial fibrillation hospitalizations. *The American Journal of Cardiology*, 138:53–60, 2021.

W Thomas Dungan, Arthur Garson Jr, and Paul C Gillette. Arrhythmogenic right ventricular dysplasia: a cause of ventricular tachycardia in children with apparently normal hearts. *American heart journal*, 102(4):745–750, 1981.

AAMI ECAR. Recommended practice for testing and reporting performance results of ventricular arrhythmia detection algorithms. *Association for the Advancement of Medical Instrumentation*, page 69, 1987.

Shaun Eisner, Flavio H Fenton, and Ilija Uzelac. Baseline wandering removal in optical mapping measurements with pid control in phase space. In *2019 Computing in Cardiology (CinC)*, pages 1–4. IEEE, 2019.

Mohamed Elgendi. Fast qrs detection with an optimized knowledge-based method: Evaluation on 11 standard ecg databases. *PloS one*, 8(9):e73557, 2013.

Mohamed Elgendi, Bjoern Eskofier, and Derek Abbott. Fast t wave detection calibrated by clinical knowledge with annotation of p and t waves. *Sensors*, 15(7):17693–17714, 2015.

Mohamed Elgendi, Marianna Meo, and Derek Abbott. A proof-of-concept study: Simple and effective detection of p and t waves in arrhythmic ecg signals. *Bioengineering*, 3 (4):26, 2016.

Andrew E Epstein, John P DiMarco, Kenneth A Ellenbogen, NA Mark Estes, Roger A Freedman, Leonard S Gettes, A Marc Gillinov, Gabriel Gregoratos, Stephen C Hammill, David L Hayes, et al. Acc/aha/hrs 2008 guidelines for device-based therapy of cardiac rhythm abnormalities: a report of the american college of cardiology/american heart association task force on practice guidelines (writing committee to revise the acc/aha/naspe 2002 guideline update for implantation of cardiac pacemakers and antiarrhythmia devices) developed in collaboration with the american association for thoracic surgery and society of thoracic surgeons. *Journal of the American College of Cardiology*, 51(21):e1–e62, 2008.

Guo-Feng Fan, Li-Ling Peng, and Wei-Chiang Hong. Short term load forecasting based on phase space reconstruction algorithm and bi-square kernel regression model. *Applied Energy*, 224:13–33, 2018.

Shih-Chin Fang and Hsiao-Lung Chan. Human identification by quantifying similarity and dissimilarity in electrocardiogram phase space. *Pattern Recognition*, 42(9):1824–1831, 2009.

Otakar Fojt and Jiri Holcik. Applying nonlinear dynamics to ecg signal processing. *IEEE engineering in medicine and biology magazine*, 17(2):96–101, 1998.

Kresimir Friganovic, Davor Kukolja, Alan Jovic, Mario Cifrek, and Goran Krstacic. Optimizing the detection of characteristic waves in ecg based on processing methods combinations. *IEEE access*, 6:50609–50626, 2018.

Dennis Gabor. Theory of communication. part 1: The analysis of information. *Journal of the Institution of Electrical Engineers-Part III: Radio and Communication Engineering*, 93(26):429–441, 1946.

Purva R Gawde, Arvind K Bansal, and Jeffrey A Nielson. Integrating markov model and morphology analysis for finer classification of ventricular arrhythmia in real time. In *2017 IEEE EMBS International Conference on Biomedical & Health Informatics (BHI)*, pages 409–412. IEEE, 2017.

A Ghaffari, MR Homaeinezhad, M Akraminia, M Atarod, and M Daevaeiha. A robust wavelet-based multi-lead electrocardiogram delineation algorithm. *Medical engineering & physics*, 31(10):1219–1227, 2009.

Fuad A Ghaleb, Maznah Bte Kamat, Mazleena Salleh, Mohd Foad Rohani, and Shukor Abd Razak. Two-stage motion artefact reduction algorithm for electrocardiogram using weighted adaptive noise cancelling and recursive hampel filter. *PloS one*, 13 (11):e0207176, 2018.

RR Gharieb, M Massoud, S Nady, and M Moness. Fuzzy c-means in features space of teager-kaiser energy of continuous wavelet coefficients for detection of pvc beats in ecg. In *2016 8th Cairo International Biomedical Engineering Conference (CIBEC)*, pages 72–75. IEEE, 2016.

Dalia Giedrimiene and Rachel King. Burden of cardiovascular disease (cvd) on economic cost. comparison of outcomes in us and europe. *Circulation: Cardiovascular Quality and Outcomes*, 10(suppl_3):A207–A207, 2017.

Ary L Goldberger, Luis AN Amaral, Leon Glass, Jeffrey M Hausdorff, Plamen Ch Ivanov, Roger G Mark, Joseph E Mietus, George B Moody, Chung-Kang Peng, and H Eugene Stanley. Physiobank, physiotoolkit, and physionet: components of a new research resource for complex physiologic signals. *Circulation*, 101(23):e215–e220, 2000.

Himanshu Gothwal, Silky Kedawat, and Rajesh Kumar. Cardiac arrhythmias detection in an ecg beat signal using fast fourier transform and artificial neural network. *Journal of Biomedical Science and Engineering*, 4(04):289, 2011.

WC Grinstead, FW Smart, CM Pratt, DG Weilbaecher, ME Sekela, GP Noon, and JB Young. Sudden death caused by bradycardia and asystole in a heart transplant

patient with coronary arteriopathy. *The Journal of heart and lung transplantation: the official publication of the International Society for Heart Transplantation*, 10(6): 931–936, 1991.

Habib Hajimolahoseini, Javad Hashemi, and Damian Redfearn. Ecg delineation for qt interval analysis using an unsupervised learning method. In *2018 IEEE International Conference on Acoustics, Speech and Signal Processing (ICASSP)*, pages 2541–2545. IEEE, 2018.

Nur Al Hasan Haldar, Farrukh Aslam Khan, Aftab Ali, and Haider Abbas. Arrhythmia classification using mahalanobis distance based improved fuzzy c-means clustering for mobile health monitoring systems. *Neurocomputing*, 220:221–235, 2017.

Haris M Haqqani, Kim H Chan, Saurabh Kumar, A Robert Denniss, and Ann T Gregory. The contemporary era of sudden cardiac death and ventricular arrhythmias: basic concepts, recent developments and future directions. *Heart, Lung and Circulation*, 28 (1):1–5, 2019.

Paul Harris and Dimitrios Lysitsas. Ventricular arrhythmias and sudden cardiac death. *BJA Education*, 16(7):221–229, 2015.

Healthcentral. Ventricular fibrillation/ventricular tachycardia, 2005.

Nicholas A Heard, Christopher C Holmes, and David A Stephens. A quantitative study of gene regulation involved in the immune response of anopheline mosquitoes: An application of bayesian hierarchical clustering of curves. *Journal of the American Statistical Association*, 101(473):18–29, 2006.

Mohammad R Homaeinezhad, M ErfanianMoshiri-Nejad, and H Naseri. A correlation analysis-based detection and delineation of ecg characteristic events using template waveforms extracted by ensemble averaging of clustered heart cycles. *Computers in biology and medicine*, 44:66–75, 2014.

Zhongjie Hou, Yonggui Dong, Jinxi Xiang, Xuewu Li, and Bin Yang. A real-time qrs detection method based on phase portraits and box-scoring calculation. *IEEE Sensors Journal*, 18(9):3694–3702, 2018.

Enbiao Jing, Haiyang Zhang, ZhiGang Li, Yazhi Liu, Zhanlin Ji, and Ivan Ganchev. Ecg heartbeat classification based on an improved resnet-18 model. *Computational and Mathematical Methods in Medicine*, 2021, 2021.

Anubha Kalra and Andrew Lowe. Development and validation of motion artefact rejection system (mars) for electrocardiography using novel skin-stretch estimation approach. *Sensors and Actuators A: Physical*, 301:111726, 2020.

Amandeep Kaur, Alpana Agarwal, Ravinder Agarwal, and Sanjay Kumar. A novel approach to ecg r-peak detection. *Arabian Journal for Science and Engineering*, 44 (8):6679–6691, 2019.

JP Kelwade and SS Salankar. Radial basis function neural network for prediction of cardiac arrhythmias based on heart rate time series. In *2016 IEEE First International Conference on Control, Measurement and Instrumentation (CMI)*, pages 454–458. IEEE, 2016.

Orhan Kesemen, Özge Tezel, and Eda Özkul. Fuzzy c-means clustering algorithm for directional data (fcm4dd). *Expert systems with applications*, 58:76–82, 2016.

George Koulaouzidis, Saptarshi Das, Grazia Cappiello, Evangelos B Mazomenos, Koushik Maharatna, Paolo E Puddu, and John M Morgan. Prompt and accurate diagnosis of ventricular arrhythmias with a novel index based on phase space reconstruction of ecg. *International journal of cardiology*, 182:38–43, 2015.

Andrew D Krahn, Jure Manfreda, Robert B Tate, Francis AL Mathewson, and T Edward Cuddy. The natural history of atrial fibrillation: incidence, risk factors, and prognosis in the manitoba follow-up study. *The American journal of medicine*, 98(5):476–484, 1995.

Pablo Laguna, Roger G Mark, A Goldberg, and George B Moody. A database for evaluation of algorithms for measurement of qt and other waveform intervals in the ecg. In *Computers in Cardiology 1997*, pages 673–676. IEEE, 1997.

Pier D Lambiase, Craig Barr, Dominic AMJ Theuns, Reinoud Knops, Petr Neuzil, Jens Brock Johansen, Margaret Hood, Susanne Pedersen, Stefan Kääb, Francis Murgatroyd, et al. Worldwide experience with a totally subcutaneous implantable defibrillator: early results from the effortless s-icd registry. *European heart journal*, 35(25): 1657–1665, 2014.

Jeong-Whan Lee, Kyeong-Seop Kim, Bongsoo Lee, Byungchae Lee, and Myoung-Ho Lee. A real time qrs detection using delay-coordinate mapping for the microcontroller implementation. *Annals of biomedical Engineering*, 30(9):1140–1151, 2002.

Jacek M Leski. Robust nonlinear aggregation operator for ecg powerline interference reduction. *Biomedical Signal Processing and Control*, 69:102675, 2021.

Wayne C Levy, Kerry L Lee, Anne S Hellkamp, Jeanne E Poole, Dariush Mozaffarian, David T Linker, Aldo P Maggioni, Inder Anand, Philip A Poole-Wilson, Daniel P Fishbein, et al. Maximizing survival benefit with primary prevention icd therapy in a heart failure population. *Circulation*, 120(10):835, 2009.

Qiao Li, Cadathur Rajagopalan, and Gari D Clifford. Ventricular fibrillation and tachycardia classification using a machine learning approach. *IEEE Transactions on Biomedical Engineering*, 61(6):1607–1613, 2013.

Chia-Hung Lin. Frequency-domain features for ecg beat discrimination using grey relational analysis-based classifier. *Computers & Mathematics with Applications*, 55(4): 680–690, 2008.

Chin-Teng Lin, Kuan-Cheng Chang, Chun-Ling Lin, Chia-Cheng Chiang, Shao-Wei Lu, Shih-Sheng Chang, Bor-Shyh Lin, Hsin-Yueh Liang, Ray-Jade Chen, Yuan-Teh Lee, et al. An intelligent telecardiology system using a wearable and wireless ecg to detect atrial fibrillation. *IEEE Transactions on Information Technology in Biomedicine*, 14 (3):726–733, 2010.

Chien-Sheng Liu, Wei-Kung Tseng, Jen-Kuang Lee, Tze-Chien Hsiao, and Chii-Wann Lin. The differential method of phase space matrix for af/vf discrimination application. *Medical engineering & physics*, 32(5):444–453, 2010.

Ramon Luengo-Fernandez, Jose Leal, Alastair Gray, Sophie Petersen, and Mike Rayner. Cost of cardiovascular diseases in the united kingdom. *Heart*, 92(10):1384–1389, 2006.

Stefano Magni, Andrea Sansonetti, Chiara Salvi, Tiziana Tabiadon, and Guadalupe García-Isla. Combining resnet model with handcrafted temporal features for ecg classification with varying number of leads. In *2021 Computing in Cardiology (CinC)*, volume 48, pages 1–4. IEEE, 2021.

Sidharth Maheshwari, Amit Acharyya, Paolo Emilio Puddu, Evangelos B Mazomenos, Gourav Leekha, Koushik Maharatna, and Michele Schiariti. An automated algorithm for online detection of fragmented qrs and identification of its various morphologies. *Journal of The Royal Society Interface*, 10(89):20130761, 2013.

Akul Malhotra and Ananthakrishna Chintanpalli. A real time wavelet filtering for ecg baseline wandering removal. In *2020 International Conference on Artificial Intelligence and Signal Processing (AISP)*, pages 1–5. IEEE, 2020.

M Sabarimalai Manikandan and KP Soman. A novel method for detecting r-peaks in electrocardiogram (ecg) signal. *Biomedical Signal Processing and Control*, 7(2): 118–128, 2012.

Arturo Martínez, Raúl Alcaraz, and José J Rieta. A new method for automatic delineation of ecg fiducial points based on the phasor transform. In *2010 Annual International Conference of the IEEE Engineering in Medicine and Biology*, pages 4586–4589. IEEE, 2010.

Juan Pablo Martínez, Rute Almeida, Salvador Olmos, Ana Paula Rocha, and Pablo Laguna. A wavelet-based ecg delineator: evaluation on standard databases. *IEEE Transactions on biomedical engineering*, 51(4):570–581, 2004.

Roshan Joy Martis, U Rajendra Acharya, and Hojjat Adeli. Current methods in electrocardiogram characterization. *Computers in biology and medicine*, 48:133–149, 2014.

MayoClinic. Ventricular fibrillation symptoms and causes, 2018.

EB Mazomenos, Taihai Chen, Amit Acharyya, Arnab Bhattacharya, James Rosengarten, and Koushik Maharatna. A time-domain morphology and gradient based

algorithm for ecg feature extraction. In *2012 IEEE International Conference on Industrial Technology*, pages 117–122. IEEE, 2012.

Evangelos B Mazomenos, Dwaipayan Biswas, Amit Acharyya, Taihai Chen, Koushik Maharatna, James Rosengarten, John Morgan, and Nick Curzen. A low-complexity ecg feature extraction algorithm for mobile healthcare applications. *IEEE journal of biomedical and health informatics*, 17(2):459–469, 2013.

MedicineNet. What is arrhythmia., 2018.

Rahul Mehra. Global public health problem of sudden cardiac death. *Journal of electrocardiology*, 40(6):S118–S122, 2007.

Patricia Melin, Jonathan Amezcua, Fevrier Valdez, and Oscar Castillo. A new neural network model based on the lvq algorithm for multi-class classification of arrhythmias. *Information sciences*, 279:483–497, 2014.

M Merah, TA Abdelmalik, and BH Larbi. R-peaks detection based on stationary wavelet transform. *Computer methods and programs in biomedicine*, 121(3):149–160, 2015.

M Mirowski, MORTON M MOWER, VINCENT L GOTT, and ROBERT K BRAWLEY. Feasibility and effectiveness of low-energy catheter defibrillation in man. *Circulation*, 47(1):79–85, 1973.

Majid Moavenian and Hamid Khorrami. A qualitative comparison of artificial neural networks and support vector machines in ecg arrhythmias classification. *Expert Systems with Applications*, 37(4):3088–3093, 2010.

Hadi Mohammadi and Guy Fradet. Prosthetic aortic heart valves. *Cardiovascular System*, 5(1):2, 2017.

Monalisa Mohanty, Santanu Sahoo, Pradyut Biswal, and Sukanta Sabut. Efficient classification of ventricular arrhythmias using feature selection and c4. 5 classifier. *Biomedical Signal Processing and Control*, 44:200–208, 2018.

George Moody. A new method for detecting atrial fibrillation using rr intervals. *Computers in Cardiology*, pages 227–230, 1983.

Lem Moyé. Statistical methods for cardiovascular researchers. *Circulation research*, 118 (3):439–453, 2016.

Shuto Nagai, Daisuke Anzai, and Jianqing Wang. Motion artefact removals for wearable ecg using stationary wavelet transform. *Healthcare technology letters*, 4(4):138–141, 2017.

Manasi Nandi, Jenny Venton, and Philip J Aston. A novel method to quantify arterial pulse waveform morphology: attractor reconstruction for physiologists and clinicians. *Physiological measurement*, 39(10):104008, 2018.

TN Narasimhan. Fourier's heat conduction equation: History, influence, and connections. *Reviews of Geophysics*, 37(1):151–172, 1999.

Annamalai Natarajan, Gregory Boverman, Yale Chang, Corneliu Antonescu, and Jonathan Rubin. Convolution-free waveform transformers for multi-lead ecg classification. In *2021 Computing in Cardiology (CinC)*, volume 48, pages 1–4. IEEE, 2021.

Isar Nejadgholi, Mohammad Hasan Moradi, and Fatemeh Abdolali. Using phase space reconstruction for patient independent heartbeat classification in comparison with some benchmark methods. *Computers in biology and medicine*, 41(6):411–419, 2011.

Petr Nejedly, Adam Ivora, Radovan Smisek, Ivo Viscor, Zuzana Koscova, Pavel Jurak, and Filip Plesinger. Classification of ecg using ensemble of residual cnns with attention mechanism. In *2021 Computing in Cardiology (CinC)*, volume 48, pages 1–4. IEEE, 2021.

NHS. Arrhythmia, 2018.

NIH. Arrhythmia, 2015a.

NIH. How the heart works, 2015b.

FM Nolle, FK Badura, JM Catlett, RW Bowser, and MH Sketch. Crei-gard, a new concept in computerized arrhythmia monitoring systems. *Computers in Cardiology*, 13:515–518, 1986.

Louise RA Olde Nordkamp, Tom F Brouwer, Craig Barr, Dominic AMJ Theuns, Lucas VA Boersma, Jens B Johansen, Petr Neuzil, Arthur AM Wilde, Nathan Carter, Michael Husby, et al. Inappropriate shocks in the subcutaneous icd: incidence, predictors and management. *International journal of cardiology*, 195:126–133, 2015.

Jiapu Pan and Willis J Tompkins. A real-time qrs detection algorithm. *IEEE Trans. Biomed. Eng*, 32(3):230–236, 1985.

M Papouchado, PR Walker, MA James, and LM Clarke. Fundamental differences between the standard 12–lead electrocardiograph and the modified (mason—likar) exercise lead system. *European heart journal*, 8(7):725–733, 1987.

Somsanuk Pathoumvanh, Kazuhiko Hamamoto, and Phoumy Indahak. Arrhythmias detection and classification base on single beat ecg analysis. In *The 4th Joint International Conference on Information and Communication Technology, Electronic and Electrical Engineering (JICTEE)*, pages 1–4. IEEE, 2014.

Emil Plesnik, O Malgina, Jurij F Tasič, and Matej Zajc. Detection of the electrocardiogram fiducial points in the phase space using the euclidian distance measure. *Medical engineering & physics*, 34(4):524–529, 2012.

Jeanne E Poole, George W Johnson, Anne S Hellkamp, Jill Anderson, David J Callans, Merritt H Raitt, Ramakota K Reddy, Francis E Marchlinski, Raymond Yee, Thomas Guarnieri, et al. Prognostic importance of defibrillator shocks in patients with heart failure. *New England Journal of Medicine*, 359(10):1009–1017, 2008.

Riccardo Proietti, Christopher Labos, Mark Davis, George Thanassoulis, Pasquale Santangeli, Vincenzo Russo, Luigi Di Biase, Jean-Francois Roux, Atul Verma, Andrea Natale, et al. A systematic review and meta-analysis of the association between implantable cardioverter-defibrillator shocks and long-term mortality. *Canadian Journal of Cardiology*, 31(3):270–277, 2015.

Klaus F Rabe, John R Hurst, and Samy Suissa. Cardiovascular disease and copd: dangerous liaisons? *European Respiratory Review*, 27(149), 2018.

Md Asadur Rahman, Md Mahmudul Haque Milu, Anika Anjum, Farzana Khanam, and Mohiuddin Ahmad. Baseline wandering removal from ecg signal by wandering path finding algorithm. In *2017 3rd International Conference on Electrical Information and Communication Technology (EICT)*, pages 1–5. IEEE, 2017.

R Mohan Raj, Vemula Rajesh, S Saravanan, M Balaji, and V Elamaran. Baseline wandering noise removal using high-speed iir filters with an fpga implementation. In *International Conference on Microelectronic Devices, Circuits and Systems*, pages 55–65. Springer, 2021.

Atiye Riasi and Maryam Mohebbi. Predicting imminent episodes of ventricular tachyarrhythmia using an entropy-based feature in the emd domain. In *2015 23rd Iranian Conference on Electrical Engineering*, pages 88–92. IEEE, 2015.

CK Roopa, BS Harish, and SV Aruna Kumar. A novel method of clustering ecg arrhythmia data using robust spatial kernel fuzzy c-means. *Procedia computer science*, 143:133–140, 2018.

Mehdi Roopaei, Reza Boostani, R Rohani Sarvestani, Mohammad Ali Taghavi, and Zohreh Azimifar. Chaotic based reconstructed phase space features for detecting ventricular fibrillation. *Biomedical Signal Processing and Control*, 5(4):318–327, 2010.

Dorthe B Saadi, George Tanev, Morten Flintrup, Armin Osmanagic, Kenneth Egstrup, Karsten Hoppe, Poul Jennum, Jørgen L Jeppesen, Helle K Iversen, and Helge BD Sorensen. Automatic real-time embedded qrs complex detection for a novel patch-type electrocardiogram recorder. *IEEE journal of translational engineering in health and medicine*, 3:1–12, 2015.

Indu Saini, Dilbag Singh, and Arun Khosla. Delineation of ecg wave components using k-nearest neighbor (knn) algorithm: Ecg wave delineation using knn. In *2013 10th International Conference on Information Technology: New Generations*, pages 712–717. IEEE, 2013.

Marko Sarstedt, Erik Mooi, et al. A concise guide to market research. *The Process, Data, and*, 2014.

R Rohani Sarvestani, R Boostani, and M Roopaei. Vt and vf classification using trajectory analysis. *Nonlinear Analysis: Theory, Methods & Applications*, 71(12):e55–e61, 2009.

Neil C Schwertman, Margaret Ann Owens, and Robiah Adnan. A simple more general boxplot method for identifying outliers. *Computational statistics & data analysis*, 47 (1):165–174, 2004.

Manish Sharma, Ru-San Tan, and U Rajendra Acharya. Detection of shockable ventricular arrhythmia using optimal orthogonal wavelet filters. *Neural Computing and Applications*, 32(20):15869–15884, 2020.

Ghassen Smaoui, Alex Young, and Mohamed Abid. Single scale cwt algorithm for ecg beat detection for a portable monitoring system. *Journal of Medical and Biological Engineering*, 37(1):132–139, 2017.

Jangwon Suh, Jimyeong Kim, Eunjung Lee, Jaeill Kim, Duhun Hwang, Jungwon Park, Junghoon Lee, Jaeseung Park, Seo-Yoon Moon, Yeonsu Kim, et al. Learning ecg representations for multi-label classification of cardiac abnormalities. In *2021 Computing in Cardiology (CinC)*, volume 48, pages 1–4. IEEE, 2021.

Zoltán Szabó, Dóra Ujvárosy, Tamás Ötvös, Veronika Sebestyén, and Péter P Nánási. Handling of ventricular fibrillation in the emergency setting. *Frontiers in pharmacology*, 10:1640, 2020.

Mazhar B Tayel, Ahmed S Eltrass, and Abeer I Ammar. A new multi-stage combined kernel filtering approach for ecg noise removal. *Journal of electrocardiology*, 51(2): 265–275, 2018.

Snehal Thalkar and Dhananjay Upasani. Various techniques for removal of power line interference from ecg signal. *Int. J. Sci. Eng. Res*, 4(12):12–23, 2013.

Nantarika Thiamchoo and Pornchai Phukpattaranont. R peak detection algorithm based on continuous wavelet transform and shannon energy. *ECTI Transactions on Computer and Information Technology (ECTI-CIT)*, 10(2):167–175, 2016.

Anurak Thungtong. A robust algorithm for r peak detection based on optimal discrete wavelet transform. In *2017 14th International Joint Conference on Computer Science and Software Engineering (JCSSE)*, pages 1–6. IEEE, 2017.

Rajesh K Tripathy, Alejandro Zamora-Mendez, José A De la O Serna, Mario R Arrieta Paternina, Juan G Arrieta, and Ganesh R Naik. Detection of life threatening ventricular arrhythmia using digital taylor fourier transform. *Frontiers in physiology*, 9:722, 2018.

RK Tripathy, LN Sharma, and Samarendra Dandapat. Detection of shockable ventricular arrhythmia using variational mode decomposition. *Journal of medical systems*, 40(4): 79, 2016.

Elif Derya Übeyli. Combining recurrent neural networks with eigenvector methods for classification of ecg beats. *Digital Signal Processing*, 19(2):320–329, 2009.

Johannes B van Rees, C Jan Willem Borleffs, Mihály K de Bie, Theo Stijnen, Lieselot van Erven, Jeroen J Bax, and Martin J Schalij. Inappropriate implantable cardioverter-defibrillator shocks: incidence, predictors, and impact on mortality. *Journal of the American College of Cardiology*, 57(5):556–562, 2011.

Naresh Vemishetty, Ramya Lakshmi Gunukula, Amit Acharyya, Paolo Emilio Puddu, Saptarshi Das, and Koushik Maharatna. Phase space reconstruction based cvd classifier using localized features. *Scientific reports*, 9(1):1–18, 2019.

José Antonio Vila, Yi Gang, Jesús María Rodríguez Presedo, Manuel Fernández-Delgado, Senén Barro, and Marek Malik. A new approach for tu complex characterization. *IEEE Transactions on Biomedical Engineering*, 47(6):764–772, 2000.

Konstantinos Vlachos, Konstantinos P Letsas, Panagiotis Korantzopoulos, Tong Liu, Stamatis Georgopoulos, Athanasios Bakalakos, Nikolaos Karamichalakis, Sotirios Xydonas, Michael Efremidis, and Antonios Sideris. Prediction of atrial fibrillation development and progression: current perspectives. *World journal of cardiology*, 8(3):267, 2016.

Steven Walfish. A review of statistical outlier methods. *Pharmaceutical technology*, 30 (11):82, 2006.

Z Wei, L Hongxing, and C Jianchun. Adaptive filtering in phase space for foetal electrocardiogram estimation from an abdominal electrocardiogram signal and a thoracic electrocardiogram signal. *IET signal processing*, 6(3):171–177, 2012.

Nong Weixin. A novel algorithm for ventricular arrhythmia classification using a fuzzy logic approach. *Australasian physical & engineering sciences in medicine*, 39(4):903–912, 2016.

W.H.O. Cardiovascular diseases (cvds), 2019.

B Wiles, PR Roberts, V Allavatam, K Maharatna, A Acharyya, H Chen, N Vemishetty, DG Wilson, and JM Morgan. The future of s-icd sensing:'improve'significantly increases r: T ratio and generates universal device eligibility without impairing vf detection. *Europace*, 20(Supplement 4), 2018.

Benedict M Wiles and Paul R Roberts. Lead or be led: an update on leadless cardiac devices for general physicians. *Clinical Medicine*, 17(1):33, 2017.

Benedict M Wiles, Paul R Roberts, Venugopal Allavatam, Amit Acharyya, Naresh Vemishetty, Mohamed ElRefai, David G Wilson, Koushik Maharatna, Hanjie Chen, John M Morgan, et al. Personalized subcutaneous implantable cardioverter-defibrillator sensing vectors generated by mathematical rotation increase device eligibility whilst preserving device performance. *EP Europace*, 2022.

Yang Xu, Dong Wang, Weigong Zhang, Peng Ping, and Lihang Feng. Detection of ventricular tachycardia and fibrillation using adaptive variational mode decomposition and boosted-cart classifier. *Biomedical Signal Processing and Control*, 39:219–229, 2018.

Özal Yıldırım, Paweł Pławiak, Ru-San Tan, and U Rajendra Acharya. Arrhythmia detection using deep convolutional neural network with long duration ecg signals. *Computers in biology and medicine*, 102:411–420, 2018.

Maxime Yochum, Charlotte Renaud, and Sabir Jacquir. Automatic detection of p, qrs and t patterns in 12 leads ecg signal based on cwt. *Biomedical Signal Processing and Control*, 25:46–52, 2016.

Sung-Nien Yu and Ming-Yuan Lee. Bispectral analysis and genetic algorithm for congestive heart failure recognition based on heart rate variability. *Computers in Biology and Medicine*, 42(8):816–825, 2012.

Unai Zalabarria, Eloy Irigoyen, Raquel Martinez, and Andrew Lowe. Online robust r-peaks detection in noisy electrocardiograms using a novel iterative smart processing algorithm. *Applied Mathematics and Computation*, 369:124839, 2020.